The Dissertation Committee for Venkateswaran Narayanaswamy
certifies that this is the approved version of the following dissertation:

Investigation of a pulsed-plasma jet for separation shock / boundary layer interaction control

Committee:

Noel T. Clemens, Supervisor

Laxminarayan L. Raja, Supervisor

Philip L. Varghese

Venkatramanan Raman

Roger D. Bengtson

Investigation of a pulsed-plasma jet for separation shock / boundary layer interaction control

by

Venkateswaran Narayanaswamy, B.Tech.

DISSERTATION

Presented to the Faculty of the Graduate School of

The University of Texas at Austin

in Partial Fulfillment

of the Requirements

for the Degree of

DOCTOR OF PHILOSOPHY

THE UNIVERSITY OF TEXAS AT AUSTIN

August 2010

To my grandfather, late Shri N. Venkateswara Iyer

Acknowledgments

I would first like to acknowledge the kindness and support extended to me by my family, without which I wouldn't have come anywhere close to completing my doctorate. I'm greatly indebted to my supervisor, Prof. Noel T. Clemens for supporting, encouraging and challenging me all these years. It has been a great learning experience to work with him. I have really enjoyed his thorough discussions and analysis on many topics. I would also like to thank Prof. Philip L. Varghese, Prof. Laxminarayan L. Raja, Prof. Roger Bengtson and Prof. Venkatramanan Raman for serving on my committee and reviewing the current work. I want to thank all my fellow graduate students and postdoctoral fellows (present and past) Dr. Ganapathisubramani, Kevin Marr, Dr. Zachary Murphree, Dr. Mirko Gamba, Dr. Bulent Yuceil, Justin Wagner, Agustin Valdivia, Dr. Michael Ryan, Dr. Pablo Bueno, Ross Burns, Brian Lochman, Sumeet Trehan and Dr. Lakshminarasimhan Krishna for all the useful discussions and suggestions. I want to specially thank Ms. Donna Soward, who has been an irreplaceble source of kindness and help throughout these years while at the Center for Aeromechanics Research. Thanks also go to the technicians in the Department of Aerospace Engineering and Engineering Mechanics: Mr. Eddie Zihlman and Mr. Timothy Valdez at the PRC wind tunnel labs, Mr. Rick Maldonado in the WRW machine shop, Mr. Travis Crooks, Mr. David Gray and Mr. Ricardo Palacios in the ENS machine shop, Mr. Frank Wise, Mr. Pablo Cortez and his assistants in the electronics shop. They all helped in many ways during my work and my stay in the program. Last but definitely one of the most valuable, I would like to thank Dr. Balaji Sampath and Ms. Uthra Vijayaragavan for all the free food that they provided me over the last two years.

Investigation of a pulsed-plasma jet for separation shock / boundary layer interaction control

Publication No. _____

Venkateswaran Narayanaswamy, Ph.D.
The University of Texas at Austin, 2010

Supervisors: Noel T. Clemens
Laxminarayan L. Raja

A pulsed-plasma jet (called a "spark-jet" by other researchers), is a high-speed synthetic jet that is generated by striking an electrical discharge in a small cavity. The gas in the cavity pressurizes owing to the heating and is allowed to escape through a small orifice. A series of experiments were conducted to determine the characteristics of the pulsed-plasma jet issuing into stagnant air at a pressure of 45 Torr. These results show that typical jet exit velocities of about 250 m/s can be induced with discharge energies of about 30 mJ per jet. Furthermore, the maximum pulsing frequency was found to be about 5 kHz, because above this frequency the jet begins to misfire. The misfiring appears to be due to the finite time it takes for the cavity to be recharged with ambient air between discharge pulses. The velocity at the exit of the jet is found to be primarily dependent on the discharge current and independent of other discharge parameters such as cavity volume and orifice diameter. Temperature measurements are made using optical emission spectroscopy and reveal the presence of considerable non-equilibrium between rotational and vibrational modes. The gas

heating efficiency was found to be 10% and this parameter is shown to have a direct effect on the plasma jet velocity. These results indicate that the pulsed-plasma jet creates a sufficiently strong flow perturbation that is holds great promise as a supersonic flow actuator.

An experimental study is conducted to characterize the performance of a pulsed-plasma jet for potential use in supersonic flow control applications. To obtain an estimate of the relative strength of the pulsed-plasma jet, the jet is injected normally into a Mach 3 cross-flow and the penetration distance is measured by using schlieren imaging. These measurements show that the jet penetrates $1.5\,\delta$, where δ is the boundary layer thickness, into the cross-flow and the jet-to-crossflow momentum flux ratio is estimated to be 0.6. An array of pulsed-plasma jets was issued from different locations upstream of a 30-degree compression ramp in a Mach 3 flow. Furthermore, two different jet configurations were used: normal injection and pitched and skewed injection. The pitched and skewed configuration was used to see if the jets could act as high-bandwidth pulsed vortex generators. The interaction between the jets and the separation shock was studied using phase-locked schlieren imaging. Results show that the plasma jets cause a significant disturbance to the separation shock and clearly influence its unsteadiness. While all plasma jet configurations tested caused an upstream motion of the separation shock, pitched and skewed plasma jets caused an initial downstream shock motion before the upstream motion, demonstrating the potential use of these plasma jets as vortex generator jets.

The effect of the plasma jet array on the separation shock unsteadiness is studied in a time-resolved manner by using 10 kHz schlieren imaging and fast-response wall pressure measurements. An array of three pulsed-plasma jets, in a pitched and skewed configuration, is used to force the unsteady motion of the interaction formed

by a 24° compression ramp in a Mach 3 flow. The Reynolds number of the incoming boundary layer is $Re_\theta = 3300$. Results show that when the pulsed jet array is placed upstream of the interaction, the jets cause the separation shock to move in a quasi-periodic manner, i.e., nearly in sync with the pulsing cycle. As the jet fluid convects across the separation shock, the shock responds by moving upstream, which is primarily due to the presence of hot gas and hence the lower effective Mach number of the incoming flow. Once the hot gases pass through the interaction, the separation shock recovers by moving downstream, and this recovery velocity is approximately 1% to 3% of the free stream velocity. With forcing, the low-frequency energy content of the pressure fluctuations at a given location under the intermittent region decreases significantly. This is believed to be a result of an increase in the mean scale of the interaction under forced conditions. Pulsed-jet injection are also employed within the separation bubble, but negligible changes to the separation shock motion were observed. These results indicate that influencing the dynamics of this compression ramp interaction is much more effective by placing the actuator in the upstream boundary layer.

Table of Contents

List of Tables

List of Figures

Chapter 1

Introduction

1.1 Motivation

Hypersonic flight has gained renewed interest in recent years owing to the need for safe and reliable space access as well as rapid long-range strike capability for military applications. Successful flight strongly depends on the optimal design of the aerodynamic structures and efficient functioning of the control surfaces and other aerodynamic components. Shock wave / boundary layer interaction (SWBLI) has a direct impact on both of the aforementioned aspects in hypersonic/ supersonic air vehicles. Figure 1.1 shows the different parts of a hypothetical hypersonic air vehicle where SWBLI would occur. It can be seen that different SWBLI occurs at several parts of the vehicle. For instance, a compression ramp interaction occurs in the engine inlet, a blunt fin interaction occurs near the tail, etc. Despite the ubiquitous occurrence of SWBLI in hypersonic/ supersonic air vehicles, there are several important aspects of SWBLI that remain not well understood.

When a supersonic flow is incident on an inclined surface such as wing flaps, inlet leading edges, etc., a shock wave is generated. If the shock is sufficiently strong, the pressure gradient associated with the shock causes the flow downstream of the shock to separate and subsequently reattach at a downstream location, resulting in a separation bubble. The shock that forms upstream of the separation bubble is termed the separation shock. The separation bubble undergoes large-scale pulsations, which

in turn cause the separation shock to oscillate. The unsteadiness of the separated flow causes large fluctuating mechanical and thermal loading. Another detrimental effect of the separation bubble pulsations is that the frequency range of the unsteadiness is broadband with peak unsteadiness occurring at frequencies of a few kHz and below. This frequency range can coincide with structural resonance frequencies of aerodynamic panels; thus, the mechanical and thermal oscillations can lead to rapid fatigue of aero-structures.

There have been various works that aim at understanding the driving mechanisms of separation bubble dynamics (see Dolling (1993, 2001)). Based on the insights gained from these works, several strategies were developed that significantly reduced the scales of the separation bubble. The ideal strategy would be the one that would completely collapse the bubble at all times, though it is not achieved yet. A critical review of some of the flow control work has been made by Viswanath (1988); Braun et al. (2008). Even with the reduced scale of separation bubble, the broadband unsteadiness of the separation bubble persists.

The present work is to develop a control strategy that aims at reducing the broadband unsteadiness of the separation bubble by forcing the separation bubble at a predetermined frequency using plasma discharges. When the unsteadiness of the separation bubble is locked to a particular frequency, it becomes a simple task to set the unsteadiness frequency away from the panel resonance, in order to mitigate the structural fatigue. In addition, if the frequency and the amplitude of the separation bubble pulsations are known, it also becomes easier for developing more accurate models for predicting the loading. In this chapter, a brief overview of the previous work on plasma based flow control is presented first. This is followed by a survey of the previous works that aims at understanding the driving mechanism of the separation

bubble unsteadiness of the SWBLI. Finally, a survey of the various control strategies employed for SWBLI control is presented. It should be mentioned that this chapter summarizes only the most relevant works and is by no means an extensive survey.

1.2 Plasma-based flow control

Plasma-based flow control has several inherent desirable features like high bandwidth, no-moving-part actuation and immunity against corrosion and other mechanical degradation found in conventional actuators. One of the first papers which envisioned the use of electric and magnetic fields to control flow appeared about fifty years ago (Resler and Sears (1958)). In this paper, the authors proposed that the electromagnetic field could be coupled with the ionized flow in order to control boundary layer separation , for example, reduction of skin friction, heat transfer, etc. They also discussed several advancements critical to electromagnetic flow control. Among them was the need for developing very powerful magnets for achieving considerable magneto-hydrodynamic (MHD) forces. Though there were several facilities that could create very powerful electric and magnetic fields when the article was published, the research efforts have been directed towards increasing the efficiency of the plasma actuators.

A critical review of the various plasma-based flow control strategies is presented in several previous works [Corke et al. (2009); Knight (2004); Braun et al. (2008)]. For achieving electro-hydrodynamic (EHD) forcing dielectric barrier discharges (DBDs) are being widely used. Flow actuation through electrothermal heating is usually achieved through glow discharges and filamentary arc discharges. MHD forcing is still in an incipient state, as it requires considerable ionization in order to observe the effect of the Lorentz force on the flow. The following section gives

a brief survey of the different electric discharges (not restricted to surface mounted actuators) used for aerodynamic flow control and their corresponding achievements towards flow actuation.

1.2.1 EHD forcing

A typical DBD actuator consists of an asymmetric arrangement consisting of two metal strips separated by a thin dielectric, often a piece of Kapton tape. Figure 1.2, reproduced from Corke and Post (2005), shows the construction of a typical DBD discharge actuator that was mounted on an airfoil. Upon striking a discharge using an a.c. power source, a self-limiting plasma is formed whose current is a few mAs. The time varying electric field causes an associated electrostatic force in the bulk flow, whose induced velocity is a few m/s per actuator. Several previous workers have studied the mechanism of actuation for DBD actuators. They found that maximum force is obtained during the positive stroke of the discharge cycle (e.g., Enloe et al. (2009)). There have also been several parametric studies that have investigated the optimum configuration to produce the maximum induced force (e.g. Corke and Post (2005)). DBDs have found extensive application in low-speed flow control and a few applications in supersonic flow control. For instance, DBD plasma actuators have been successfully used for separation control on airfoils (e.g., Post and Corke (2004) and Post and Corke (2003)). They have also been successfully employed to reduce drag on bluff bodies (e.g., Kozlov et al. (2006)). Enhancement of lift on airfoils has been another area where DBDs have found an application. For example, Post and Corke (2003) obtained an overall increase in lift of about 12% in a NACA $66_3 - 018$ airfoil using DBD actuators. They also reported an increase in stalling angle by 8° and a 400% increase in lift-to-drag ratio. Grundmann and Tropea (2007) successfully

employed DBDs to delay transition in a high Reynolds number subsonic flat plate boundary layer.

The application of DBD actuators for supersonic flow control applications is relatively new. A few previous workers have used DBDs to create actuation in supersonic flows. For example, Kosinov et al. (1990) used DBDs as a trip to cause transition in Mach 3.5 laminar boundary layer. DBDs have also been used to control the vortex shedding at the wake of a cylinder placed in a Mach 1.4 flow (Corke et al. (2009)). Roth and Sherman (1998) and Roth (2003) speculated about coupling a multitude of individual DBD actuators that individually induce a velocity of a few m/s to obtain much larger velocities (hundreds of m/s). This concept has not been realized yet, but if it ever is, there is no doubt that DBD actuators would be more widely employed for control of supersonic flows.

1.2.2 MHD forcing

Flow actuation using predominantly the Lorentz force has been a subject of interest for several years. The major constraint in using the Lorentz force to cause flow actuation is that the force scales with ion number density; hence, it usually requires a significant ion/electron number density to be effective. However, at higher ion number densities, the effect of Joule heating becomes quite significant and can mask the effect of the Lorentz force. This is seen from the parameter called the "load factor", which is defined as the ratio of energy deposited by Joule heating to the work done by the magnetic fields. The value of the load factor for a typical discharge current of few hundred milliamps and magnetic field of a few Teslas is about 500. This implies that the energy deposited by electrothermal heating is about 500 times larger than the work done by external magnetic fields. Hence, the direct effect of

the Lorentz force is not felt compared to the effect of Joule heating. However, some previous work has been done to isolate the effect of the Lorentz force by imposing an external magnetic field in an RF discharge. The RF discharge ionizes the flow to achieve adequate ion/electron number density without heating the flow appreciably. Cheng et al. (2002) studied the effect of imposed Lorentz force on the turbulence level inside a Mach 3 and Mach 4 boundary layer. On applying an accelerating Lorentz force (i.e., Lorentz force along the incoming flow direction) they observed a decreased turbulence intensity inside the boundary layer by over 20%. Later Nishihara et al. (2005) showed that a retarding Lorentz force (i.e., Lorentz force opposite to the incoming flow direction) induced high density fluctuations inside the boundary layer. However, they failed to observe a noticeable effect with an accelerating force. Nishihara et al. (2006) measured the fluctuation in velocities inside a Mach 3 turbulent boundary layer. They clearly showed that both accelerating and decelerating Lorentz force caused much lower fluctuations compared to the one without forcing. They also noted that an accelerating force results in smaller fluctuations than a decelerating force.

Studies were also performed with an external magnetic field in the presence of glow and arc discharges. In these actuators, there is a dominant role of electrothermal heating and the magnetic field manifests its effect subtly by changing certain discharge characteristics. These "hybrid" actuators will be discussed in the section 1.1.4.

1.2.3 Electrothermal heating

Electrothermal (Joule) heating is perhaps the most common actuation mechanism employed in supersonic flows. Electrothermal heating occurs when the energetic electrons and ions transfer a part of their energy to the neutrals via collisions, thereby

heating the bulk flow. Filamentary arcs and glow discharges have been traditionally used to produce significant Joule heating. These filamentary arcs have been shown to be more efficient than glow discharges since they are closer to equilibrium owing to higher ion/electron number densities. It should be mentioned that other actuation mechanisms act simultaneously with Joule heating in arcs and glow discharges.

Bityurin et al. (2002a) and subsequent workers (Bityurin et al. (2002b,c) and Leonov et al. (2005)) used a surface mounted arc discharge with a power of 1- 10 kW to actuate a Mach 2 boundary layer. With low input power, thickening of the boundary layer was observed as shown in fig 1.3 (a) (reproduced from Leonov et al. (2003)). However, with higher input power (>2kW or 10% incoming flow enthalpy), they were able to achieve global separation and thermal choking of their wind tunnel as shown in fig 1.3 (b) taken from the same reference as figure 1.3 (a). In a later study Leonov et al. (2009) employed filamentary arc discharges with an input power of 90 MW to enhance mixing in subsonic and supersonic flows significantly. Menart et al. (2007) employed a surface arc with 1.25 kW d.c. power in the presence of an external magnetic field to actuate a Mach 5 boundary layer. The applied magnetic field was directed "away from" (upward) or "towards" (downward) the floor on which the actuators were mounted. They measured the average static and Pitot pressure change due to the applied electric and magnetic fields. The upward-directed magnetic field caused an increase in surface pressure whereas a downward-directed magnetic field causes the wall pressure to level off beyond certain magnitude of the applied field. The authors suggested that the increase in surface pressure with an upward-directed magnetic field is possibly due to lifting up of electrons and ions due to the applied magnetic fields. This creates a larger volume in which the electrons and ions can move and collide, and hence causes electrothermal heating. However, with the

magnetic field directed downwards, the authors argue that the applied field confines the electrons and ions close to the actuator surface, and thus restricts the region of electrothermal heating, which leads to leveling off of the surface pressure. Yan et al. (2007) studied the use of a pulsed arc discharge as a thermal trip for a Mach 1.5 boundary layer. The pulsed arc was numerically simulated by a sudden rise in wall temperature in the actuator area by 500 K. With the simulation, the authors showed that a steady d.c. arc creates a stronger counter rotating vortex pair compared to a pulsed d.c. arc. The authors reported that the pulsed discharge causes vortex shedding behind the actuator. In both cases the authors observed creation of a generalized inflection point in the boundary layer which was absent in the unforced case.

Previous workers have also attempted to use other phenomena that are present in arc discharges for flow control. Notable among them is the utilization of "double layers" for improved heating efficiency. The studies will be mentioned in this survey briefly. Bletzinger et al. (2003) and Bletzinger et al. (2005) have quoted several studies in addition to their own, in which formation of a "double layer" is reported for arc discharges that have high ion number densities. A double layer is formed when the component of the gaseous mixture is heated inhomogeneously by the arc. They argue that these double layers can be used to cause very efficient gas heating that could alter the shock front. In a drag reduction application, Elias et al. (2007) sought to understand the role of the double layer that is formed behind an oblique shock generated by a cone placed a Mach 3 flow. The study involved identifying the formation of double layers with different discharges from low current coronas to arcs. For the values of current tested (< 0.25 A), the authors could only infer the presence of a double layer. They also found that there was no noticeable drag reduction for

the range of electrical current tested. They attributed this to inefficient heating of the gas because their theoretical model indicated that about 90% of the input energy is locked in vibrational modes.

Kuo et al. (2000) employed a 1.2 kW "spray-like" plasma discharge mounted on a conical nose placed in a supersonic flow in order to control the bow shock in front of the cone. The authors found that when the discharge was generated the bow shock moved upstream. At the instance of the most intense discharge, the bow shock completely disappeared. However, the bow shock returned to its unforced position as the discharge intensity decreased. It should be noted that in this study the mechanism of flow actuation is not the electrothermal heating alone. The authors argue that the propagation of the electrons upstream of the separation shock plays a considerable role in flow actuation. Even though it is very clear that the arc discharges can cause significant flow actuation, one of the primary disadvantages is that the average power consumption is of the order of several kWs to MWs per discharge. This implies that if one has to scale up the number of actuators, to cover large surface area, the power requirement is going to be exorbitant. Hence, several strategies were employed to bring down the average power, without seriously compromising the actuation authority (i.e., improving the efficiency of the actuator). The most promising among them are the pulsed arc discharges and glow/ abnormal glow discharges.

Pulsed arc discharges have been successfully employed for flow control by Samimy et al. (2004). The average power consumption of these arcs (Large Area Filamentary Plasma Actuators) is few hundred watts per discharge for a typical duty cycle of 5%. As with other filamentary arcs, the mechanism of actuation is predominantly by Joule heating. The average temperature rise due to the discharge is

reported by Keshav et al. (2007) to be about 2000 K. Samimy et al. (2004); Keshav et al. (2007); Samimy et al. (2007) and Kim et al. (2007) have successfully employed these discharges to control high subsonic and supersonic jets. They showed global changes in mixing characteristics and noise production by exciting several instability mechanisms that are inherently present in the jet. For instance, Kim et al. (2007) used an array of 8 plasma actuators operated at different phases with respect to one another. They demonstrated that their actuator could excite different instability modes present in the jet. This led to substantially higher mixing. Upon employing these actuators, Samimy et al. (2007) reported that the far-field noise level was reduced by 2-4 dB. More recently, Fischer et al. (2009) successfully employed the LAFPA to control the noise level of a heated M = 0.9 jet. Overall, the noise level in the far-field was reduced by more than 2 dB upon actuating with the LAFPA. They argued the reduction of the noise is because actuation diverts the energy to the instability modes other than the fundamental instability mode (m=0). They also found that the effectiveness of the actuator increases with increasing temperature of the jet fluid. Pulsed arc discharges (LAFPA) were also employed by Caraballo et al. (2009) for controlling impinging shock/boundary layer interactions generated by a 10° shock generator placed in a Mach 1.9 flow. They employed 8 actuators that operated either in phase or out of phase with one another. They found that the velocity profile measured downstream of the interaction appeared fuller upon actuation. They attributed this observation to the formation of streamwise vortices caused by the plasma discharge. However, they could not observe any noticeable changes in the wall pressure fluctuations downstream of the interaction, and neither could they find any observable changes in the schlieren imaging of the structure of the SWBLI. More recently, Wang et al. (2009) employed pulsed plasma arcs in the presence of external magnetic field to control separation shock generated by a 20° compression ramp placed in a Mach

2.1 flow. The tests with plasma discharge in the absence of external magnetic field made the separation shock move upstream, simultaneously decreasing the shock angle. They observed a corresponding decrease of 8.6% in surface pressure proving that the actuation indeed had weakened the separation shock. Further weakening of the separation shock was observed by adding external magnetic forcing directed both in the upstream and downstream directions. In particular, the authors found that the downwind-directed magnetic forcing was more effective. The authors argue that the enhancement of the actuation with magnetic force is because the magnetic fields alter the character of the discharge from continuous pulses to a periodic burst mode, as the discharge could not sustain itself in the presence of the external magnetic field. This caused enhanced peak power per pulse and hence higher joule heating since the power supply was set to maintain the same average current. Other than pulsed DC discharges, recently Kim et al. (2009) developed a RF pulsed discharge for actuation. They report much higher heating efficiency by the pulsed RF discharge compared to pulsed DC arcs that they were using previously. The gas temperature increases by about 4 times more than the pulsed DC discharges. They employed this actuator to control a Mach 0.9 jet. Though the peak gas temperature with pulsed RF discharge was significantly higher than that with pulsed DC arcs, the jet mixing characteristics on actuation with RF pulsed arcs were not different from those using pulsed DC arcs.

Another main type of low power discharge that is being used for supersonic flow control is the glow and abnormal glow discharge. Glow discharges have been traditionally used as a trip (an acoustic disturbance) to cause transition in laminar supersonic boundary layers. In one of the first experiments to study the supersonic boundary layer transition, Kendall (1975) employed surface mounted glow discharges to trip the laminar boundary layer developed over a flat plate from M = 1.5 to 5.6.

During later studies, the glow discharges were also employed to trip boundary layers developed over other canonical bodies, e.g., cones at an angle of attack (e.g., Ladoon and Schneider (1998)). Recently glow discharges have been employed as a trip to cause transition in a hypersonic boundary layer at M = 6 (Maslov et al. (2001)).

In recent years, glow discharges have been employed to create a much stronger disturbance, compared to a boundary layer trip, and to cause considerable flow actuation of supersonic flows. Some of the recent works employing glow discharges for supersonic flow control are reviewed by Braun et al. (2008). Kimmel et al. (2004) employed a surface discharge with discharge current between $50 - 200\,mA$ in the presence of external magnetic field to actuate a Mach 5 flow. They reported a rise in surface pressure by about 10% when the discharge was turned on. They also reported that the rise in surface pressure increased with increasing input power. At large values of discharge current (few 100 mA) or magnetic field (few Teslas) the discharge switched from a diffuse structure to a constricted one, which caused significant changes in flow actuation. Kimmel et al. (2005) compared the plasma actuation using linear (plate-like) and pin-like electrodes. They showed that while linear electrodes produced a largely 2D disturbance, the pin-like electrodes produced a 3D disturbance. Surface glow discharges were also employed by Shin et al. (2006) in a Mach 3 flow. They were able to demonstrate that the actuation took place within 200 μs of the start of discharge. Similar to Kimmel et al. (2004), Shin et al. (2006) also reported a change in discharge structure, from a diffuse glow discharge to a constricted discharge, with increasing discharge current. They also showed that the diffuse discharge is more efficient in flow actuation as compared to the constricted discharge. They argued that this is probably due to a significant role of electrostatic forcing in the diffuse discharge that is absent in a constricted discharge. Menart et al. (2006) performed an

assessment of lift on a flat plate, placed in a Mach 5 flow, caused by plasma discharge with different cathode sizes and location. The discharge current employed was 9 and 24 mA. They found that bigger cathode size provided greater lift to power ratio. However, the changes were within a factor of two, compared with the uncertainty estimate of about 10%.

Zaidi et al. (2007) successfully employed a "snowplough" discharge in the presence of an external magnetic field to control impinging shock wave boundary layer interaction generated by a 10° and 14° shock generator placed in a Mach 3 flow. Theoretical predictions of these actuators are found in Macherert (2006). Essentially, this actuator consists of a pair of diverging electrodes along which a transverse discharge propagates. The Joule heating of the bulk flow causes less than a 10% increase in the static temperature as shown by Macherert (2006); Kalra et al. (2009). This implies that the role of Joule heating is negligible. The external magnetic field is applied such that the Lorentz force is directed upstream or downstream to the incoming flow. Using an upstream directed Lorentz force at low discharge currents ($\approx$ 80mA), Kalra et al. (2009) were able to create a local separation bubble in an otherwise incipient SWBLI generated by 10° shock generator. At higher discharge current ($\approx$200 mA) and with downstream directed Lorentz forcing, they were able to demonstrate a considerable reduction in the extent of the separation bubble created by a 14° shock generator.

Recently arc discharges have been employed by Grossman et al. (2003) and subsequent researchers (Grossman et al. (2004); Cybyk et al. (2004, 2005, 2006) and Haack et al. (2008)) to generate a pulsed jet, which they termed a "spark jet". Grossman et al. (2003) performed numerical simulations using a one dimensional heat addition model to predict the velocity of the spark jet for different input energies.

They found that for the range of input power tested jet velocities as high as $1000\,m/s$ could be obtained (e.g., Grossman et al. (2003) and Cybyk et al. (2005)). Grossman et al. (2004) performed a parametric study of the dependence of the jet exit velocity on different discharge and geometric parameters, both numerically and experimentally. They found that the jet exit velocity increased with decreasing cavity volume and increasing orifice diameter. Cybyk et al. (2006) mounted the spark jet actuator in a miniature thrust stand to measure the impulse generated by the spark jets. They found that the typical magnitude of the impulse is about $1\mu N - s$ for an input energy of about 0.05 J per pulse. They also noted that the impulse increases linearly with input energy. Cybyk et al. (2006) and Haack et al. (2008) performed high resolution particle image velocimetry and digital speckle tomography to obtain detailed velocity measurements of the spark jet. They showed that the peak velocity of the entrained fluid was 53 m/s. It should be noted that the actual velocity of the spark jet was expected to be much higher than velocity of the entrained fluid reported here. Haack et al. (2008) measured the time variation of the temperature of the spark jet using digital speckle tomography. They observed that the temperature increases from room temperature to 1600 K in $75\,\mu s$. The temperature then suddenly drops between 75 and 100 μs and then gradually drops beyond 200 μs. They noted that the time period of the sudden drop in temperature corresponds to the duration at which the spark jet was issued.

The studies presented above clearly demonstrate the potential for employing plasma based actuators for supersonic flow control applications. In the present study, the plasma actuators are employed to control shock wave/ turbulent boundary layer unsteadiness. A brief survey of the mechanisms of the shock wave boundary layer interaction and the previous attempts to control it using mechanical actuators is

presented in the next two sections.

1.3 Shock wave boundary layer interaction

Shock wave / boundary layer interactions (SWBLI) represent complex flow phenomena that are associated with a wide range of flows including transonic airfoils, supersonic inlets, control surfaces of high-speed aircraft, missile base flows, reaction control jets, over-expanded nozzles and many others. Often the shock induces significant boundary layer separation, which leads to a highly unsteady flow field that can cause aircraft buffeting, inlet instability, severe thermal loading of hypersonic vehicles, and aero-structure fatigue when the pressure oscillations couple to panel resonant frequencies. SWBLI is a topic that has seen extensive study over the past 50 years (Dolling (2001)) after it was first identified by Kistler (1964), and there already exist many excellent reviews of past work on SWBLI. Dolling (1993) and Smits and Dussague (1996) reviewed work in supersonic SWBLI through the early to mid nineties, including discussions of the unsteady flow fields and include some early thoughts on driving mechanisms. Other notable reviews include those by Delery and Marvin (1986), Zheltovodov (1996) and Andreopoulos et al. (2000). Dolling (2001) gives a perspective on what issues remain unaddressed regarding the unsteadiness of SWBLI. These include understanding the source of low-frequency unsteadiness, developing improved computational capabilities, investigating more complex three-dimensional flows and developing techniques for active control of shock-induced turbulent separation. Knight and Degrez (1998) provide reviews of computational work in this area.

1.3.1 Driving mechanisms of shock boundary layer interaction unsteadiness

The shock induced separated flow unsteadiness is characterized by motions that span a wide range of time scales. These scales range from small values that correspond to the characteristic upstream boundary layer fluctuations (δ/U) through very large values that correspond to time scales about 10 to 100 times larger. It is the low frequency unsteadiness that is of practical importance since it is these frequencies that couple to the resonant frequencies of aircraft structures. The driving mechanism for the low frequency unsteadiness of the separation bubble is still not resolved. Almost all of the previous studies on SWBLI unsteadiness show that the separation shock seems to respond to large-scale pulsation of the separation bubble. So the real question that is explored in the SWBLI studies is what drives the large-scale pulsations of the separated flow? Dussauge (2001) mentions that the cause of separation bubble unsteadiness could be one or more of

(i) Influence of upstream boundary layer unsteadiness

(ii) Intrinsic instabilities inside the separation bubble

(iii) Combined interaction between the above mechanisms

Previous studies have focused on exploring the role of each of the above and there is convincing evidence that in certain situations the upstream boundary layer influence dominates whereas in other situations the separation bubble instabilities control the separation bubble motion. A survey of the evidence for each of the mechanisms is presented in the following sections.

1.3.1.1 Upstream Mechanism

One of the first experimental studies to suggest an upstream boundary layer mechanism was by Andreopoulos and Muck (1987), who made wall pressure measurements under a Mach 3 compression ramp interaction. They found that the separation bubble motion scales with the bursting frequency of the incoming boundary layer, hence attributing the reason of the separation bubble motion to the upstream boundary layer. Erengil and Dolling (1991, 1993) performed wall pressure fluctuation measurements underneath a Mach 5 compression ramp interaction. They observed a correlation between the incoming boundary layer fluctuations with high frequency jitter of the separation shock. They concluded that the high frequency jitter of the separation shock is because of the passage of the turbulent eddies. For the low frequency motions, they found a strong correlation between the separation bubble pulsations and the low frequency oscillations of the separation shock foot. However, they were unable to determine what drives the motion of the separation bubble. Later Hunt and Nixon (1995) performed VLES on SWBLI and found that the shock velocity fluctuations are directly correlated to the velocity fluctuations of the incoming boundary layer structures. Wu and Miles (2001) performed MHz rate planar laser scattering visualization to study the response of the separation shock to the passage of turbulent eddies. They showed that different incoming structures caused different effects on the separation shock. The structures that were inclined at 90° caused the maximum upstream motion and the ones inclined at 45° caused the least motion.Beresh et al. (1997) performed simultaneous planar laser scattering and wall pressure fluctuation measurements in a Mach 5 compression ramp interaction. They showed convection of the upstream structures does change the outer region of the separation shock, but the shock foot remained relatively at the same location. Brusniak and Dolling (1994)

made wall pressure measurements in a SWBLI generated by a blunt fin placed in Mach 5 flow. They correlated the pressure signals at different locations and found that the correlation contains a narrow peak due to convection of the turbulent eddies and a broad peak due to separation bubble unsteadiness. They also found a low frequency signature in the wall pressure fluctuations measured in the incoming boundary layer. They concluded that "the most obvious result is that a correlation does exist between signals from under the incoming undisturbed boundary-layer flow and both the intermittent and separated flow regions." McClure (1992) performed simultaneous Pitot pressure measurements at a specific wall normal location in the incoming boundary and wall pressure measurements underneath a SWBLI generated by a compression ramp in a Mach 5 flow. McClure found that the separation shock location correlated with positive / negative fluctuations of the Pitot pressure at a fixed location in the upstream boundary layer. Unalmis and Dolling (1994) also performed Pitot probe measurements in the incoming boundary layer in a Mach 5 SWBLI. Based on their result and that of McClure (1992), they argued that thickening and thinning of the boundary layer is associated with upstream and downstream motion of the separation shock. Beresh et al. (2002) performed a simultaneous wall pressure fluctuations measurement and velocity fluctuation measurements using particle image velocimetry in the streamwise plane of the SWBLI in a Mach 5 flow. They reported a systematic correlation between the velocity fluctuations in the lower part of the upstream boundary layer and the separation shock location and motion even though they did not observe the thickening and thinning mechanism observed earlier by Unalmis and Dolling (1994). They found larger velocity fluctuations in the upstream boundary layer correlated with greater excursion of shock foot and the correlation between upstream fluctuation and the separation shock foot increased at locations close to the wall. Ganapathisubramani et al. (2006) performed particle image velocimetry in a

spanwise plane in the logarithmic region of a Mach 2 turbulent boundary layer. Ganapathisubramani et al. (2006) found the presence of elongated ($> 8\ \delta$ long) regions of positive and negative velocity fluctuations organized in the spanwise directions, similar to the ones found in incompressible boundary layers. Later Ganapathisubramani et al. (2007) studied the SWBLI generated by a 20 compression ramp placed in a Mach 2 flow using particle image velocimetry at different wall normal planes. By systematic analysis of the velocity fields, Ganapathisubramani et al. (2007) observed that the separation bubble surrogate was located downstream (upstream) at the spanwise locations where the incoming boundary layer was populated with high (low) momentum streaks. Based on this evidence they suggested that these streaks drive the low frequency motion of the separation bubble. Ganapathisubramani et al. (2009) studied the same interaction in a time resolved fashion by performing particle image velocimetry in the spanwise plane in the logarithmic region at 10 kHz. Ganapathisubramani et al. (2009) traced the motion of the separation bubble surrogate and the fluctuations of the incoming boundary layer in a time resolved manner. From the time histories of the upstream velocity fluctuations and the separation bubble surrogate motion, they argued that the global unsteadiness of the separation bubble is driven by the mean momentum of the incoming flow. They observed that the fluctuations in the momentum of the incoming boundary layer precede the separation bubble motion by about 7 flow time scales. Humble et al. (2007) performed tomographic PIV on an incident shock wave turbulent boundary layer interaction. They observed the presence of hairpin vortical structures in the incoming boundary layer and a spanwise organization of structures in the boundary layer. However, they noted that this spanwise organization is not found in many realizations. They found the reflected shock structure (spanwise wrinkling) conformed very closely to the spanwise structure of the incoming boundary layer. Based on their observations they propose

that the wrinkling of the reflected shock is caused by the spanwise organization of the structures in the incoming boundary layer and the streamwise motion is caused by the mean momentum of the incoming flow.

1.4 Downstream Mechanism

Several earlier works have also been done to study the influence of separation bubble instabilities in a SWBLI. Bulk of the studies was performed on an impinging shock wave boundary layer interaction for different incident shock strengths. Dupont et al. (2006) performed wall pressure measurements in the SWBLI region generated by a 10 shock generator. They found a very high coherence (>0.8) between the wall pressure fluctuations near the vicinity of the reflected shock and the reattachment region. This strong coherence led the researchers to conclude that the separation bubble and the separation shock oscillate as a quasilinear system. Motivated by this result, measurements were made inside the separation bubble using PIV in order to locate some dominant feature that could cause the low frequency unsteadiness of the separation shock. Dupont et al. (2005) and later Dussauge et al. (2006) performed particle image velocimetry at a spanwise plane of the SWBLI generated by a 10° shock generator placed in a Mach 2.1 flow. They found the presence of strong tornado vortices with frequency similar to the low frequency unsteadiness of the separation shock. Dussauge et al. (2006) mentioned that apparently "these eddies are the only vortical structure in the flow field able to generate unsteady motions in the appropriate frequency range". However, these tornado vortices were not present in SWBLI generated using smaller angles of shock generator (weaker separation). Hence, later works explored other mechanisms inside the separation bubble that could possibly drive the separation shock unsteadiness.

Dupont et al. (2006) made a detailed study of the space-time organization of the impinging SWBLI. They made the simultaneous wall pressure measurements with different separation distances between the transducers. Their measurements spanned the entire SWBLI region. From the evolution of the strouhal number of the dominant frequency along separation bubble, they found a similarity in the structure between supersonic separation bubble and a canonical subsonic mixing layer. They also showed that a mixing layer was formed just downstream of the separation shock. This mixing layer grew in size along the separation region before it shed after a critical size. They also showed that this growth and decay of the mixing layer was more pronounced for a strong separation bubble compared to a weak bubble. Dupont et al. (2006) also measured the growth rate of the mixing layer along the separation bubble from the streamwise evolution of the dominant strouhal number and they were able to obtain similar growth rate from theoretical considerations accounting for the compressibility effects. Dupont et al. (2008) performed PIV in the streamwise plane along the impinging SWBLI in order to in order to make detailed quantitative measurements of the mixing layer. They studied the mixing layer that developed downstream of the reflected shock from 8° and 9.5° shock generators. They found that the vortices in the mixing layer, while present in the two cases studied, were more organized for an 8° shock generator case and less organized for a 9.5° shock generator case. Recently Piponniau et al. (2009) also performed streamwise PIV of an impinging SWBLI in a Mach 2.1 flow. They studied the correlation between the size of the separation bubble and the location of the reflected shock. They found that the reflected shock was often located upstream (downstream) for a large (small) sized separation bubble. Piponniau et al. (2009) proposed a simple model to explain the driving mechanism of the separation bubble in the SWBLI. They proposed that the mixing layer that develops downstream of the separation shock entrains the low momentum fluid in-

side the separation bubble causing a partial vacuum. This causes flapping of the separation bubble in order to entrain fluid from downstream to replenish the partial vacuum created by the mixing layer. By estimating the time scale associated with the entrainment, Piponniau et al. (2009) obtained a good collapse in the corresponding Strouhal number of the separation bubble generating in the subsonic through the supersonic flows. This collapse shows that the mixing layer entrainment mechanism is indeed instrumental in the flapping motion of the separation bubble. This flapping motion causes thickening and thinning of the separation bubble, which in turn drives the reflected shock.

Ringuette et al. (2008) performed direct simulation of the SWBLI of a 24° compression corner placed in M = 2.9 flow at a $Re_\theta = 2300$. They reported the presence of long streamwise streaks of velocity fluctuations in the logarithmic region, similar to the ones found by Ganapathisubramani et al. (2006). Wu and Martin (2008) analyzed the DNS data of Ringuette et al. (2008) and found a relatively low correlation between incoming large scale structures and shock position. However, they reported a much higher correlation between mass flux at the reattachment and the separation shock location with fluctuations at the reattachment leading the separation shock location. Hence, they proposed that shock motions are related to some feedback loop between the separation bubble, the separated shear layer and the reattachment region, similar to the wake instability found in a cavity flow.

Pirozolli and Grasso (2006) performed DNS of an incident shock at M = 2.25. Based on their results, they proposed an acoustic feedback mechanism inside the interaction region similar to that of a cavity flow. They also made predictions on the resonant cavity tones of the separation bubble, which agreed with the experimental values. Touber and Sandham (2008) performed LES on impinging SWBLI at M =

2.1. They showed the presence of a global instability mode whose node is inside the separation bubble. They also showed that this location also coincided with the source of slowly propagating upstream disturbance, similar to subsonic separated flows. They proposed that the balance between topological changes in the separation bubble cause by the global instability and the natural momentum balance and possible an acoustic feedback loop is the mechanism that causes the low frequency motion of the separation shock.

Thus, it is quite clear that there is a definite contribution from both upstream velocity fluctuations and separation bubble instabilities to drive the separation bubble pulsations. Therefore, several control schemes were designed that modulates either or both of upstream boundary layer and separation bubble in order to modulate the separation shock motion and/or suppress the separation bubble. A detailed survey of the various separation shock control strategies employed is given the next section.

1.5 Control of shock-induced turbulent separation

For the last few decades, researchers have studied the control shock wave boundary layer interaction through various means. The main objectives of these previous studies on the shock-induced separation control have been:

1. To reduce in size or completely eliminate the separation bubble
2. To shift the frequency of the separated flow unsteadiness to a frequency band that does not coincide with the resonant frequency of structural panels.

The motivation for developing the control strategies for the separated flow unsteadiness stems from the studies (discussed in the previous section) that showed that the

separation shock responds to disturbances in both the incoming boundary layer and the separation bubble. Hence, several strategies to cause modulation of both the upstream boundary layer and inside the separation bubble have been developed with some success. A detailed survey of the various means used for controlling SWBLI until the late 1980's are given by Viswanath (1988).

The control devices are classified as active and passive depending on whether the user has the control over when the actuator is activated. Passive control devices are the ones that are not activated by the users, but are permanently present in the flow. Examples of passive control devices include vortex generators, aerodynamic mesoflaps, sub-boundary layer ramps, etc. Active control devices carry the advantage of less parasitic drag when compared to passive control devices. Examples of active control devices include external suction and blowing, piezoelectric membranes, shape memory alloys, plasma actuators etc. A brief survey of the different flow control devices and their corresponding impact on SWBLI is presented in subsequent sections.

1.5.1 Passive control devices

Control of the SWBLI has been demonstrated using passive control devices such as streamwise slots (e.g., Holden and Babinsky (2005)), three dimensional bumps (e.g., Babinsky et al. (2008)), vortex generators (e.g., McCormick (1992)), etc. There had been varying degrees of success in improving pressure recovery downstream of the interaction, suppression of the separation bubble, reduction of amplitude of separation shock unsteadiness, etc., using these passive control devices. A few of these devices that have been employed for separation shock control applications are discussed in the following paragraphs.

One of the most common passive control devices that are employed for SWBLI

control is the vortex generator (VG). Vortex generators work by inducing streamwise vortices, which carry high momentum fluid to deep within the boundary layer, and thus energize the boundary layer and make it more resistant to separation. McCormick (1992) used Wheeler doublets to control separation shock in an M=1.6 axisymmetric flow. The doublets were located 20δ upstream of the separation shock, and were able to reduce the interaction length by a factor of 2.3 and suppress the separation bubble. However, the authors reported that the Wheeler doublets resulted in a larger total pressure loss. Barter and Dolling (1995a,b) employed passive VGs to control the interaction generated by a 28° swept (Barter and Dolling (1995a)) and the unswept (Barter and Dolling (1995b)) compression ramp placed in a Mach 5 flow. They placed the VGs 16δ upstream of the separation shock. They reported a reduction in the length of the intermittent region and upstream influence region by about 60% and the amount of energy in the structural resonance band by about 50%. However, they could not detect noticeable effect on the SWBLI generated by a blunt fin at the same Mach number. Bueno et al. (2006) demonstrated dynamic suppression of the separation bubble generated by a 20 compression ramp placed in a Mach 2 flow using counter-rotating-vane type VGs, by raising and lowering the VGs during a run. They performed time-resolved planar laser scattering and phase-locked PIV to study the interaction. They showed that the scales of the separation bubble were reduced by about 50% when VGs were fully raised. They also showed that the velocity profile downstream of the vortex generators became fuller when the VGs were raised. Holden and Babinsky (2004) studied two different VGs, a wedge type VG and an array of counter-rotating vane type VGs, to control the separation bubble created by a normal shock boundary layer interaction in a Mach 1.5 flow. They performed wall pressure measurements, schlieren imaging and oil streak visualization to study the interaction. They reported a suppression of the separation bubble and an overall

improvement in the total pressure recovery using both the VGs. They also reported that the vane type VGs were more effective at reducing the separation compared to the wedge-type VGs. Holden and Babinsky (2007) and Pitt Ford and Babinsky (2007) employed the sub-boundary layer vortex generators for the SWBLI control in M = 2.5 flow. The sub-boundary layer VGs have a much lower drag penalty compared to a conventional vortex generator. The authors reported that the regions of downwash showed considerable reduction in scale of the separation bubble. Although these VGs could not completely eliminate the separation bubble, they were able to break the 2D separation bubble to smaller 3D bubbles.

Another passive control device that has been used for SWBLI control application is the aerodynamic mesoflap. The schematic of a mesoflap (reproduced from Lee et al. (2004)) is shown in figure 1.4. The mesoflaps are made up of a matrix of small flaps that cover a cavity. When there is no shock over the mesoflap the pressure inside the cavity and free stream are equalized and the mesoflap is deactivated. However, when the separation shock is on top of the flap, the pressure inside the cavity is in between the upstream and downstream pressure of the shock. This deflects the portion of the mesoflap downstream of the shock down so that air downstream of the shock is drawn in to the cavity. Simultaneously, the portion of the mesoflap upstream of the shock opens up and a wall jet issues from the cavity towards the shock, which energizes the upstream boundary layer. The mesoflap both bleeds the separation bubble and forms a wall jet, which synergistically reduce the separation bubble scale and displace the separation shock downstream. Successful application of the mesoflaps has been made for separation shock control by many previous researchers (e.g., Gefroh et al. (2002), Loth et al. (2004), Sreenivasan et al. (2004), etc.). Gefroh et al. (2002) employed the mesoflaps to control flow separation caused

by impinging shocks generated in an $M = 2.45$ flow. They found that the boundary layer downstream of the SWBLI region was thinner when the mesoflaps were employed. They also showed a slightly better pressure recovery of the static and the stagnation pressures downstream of the SWBLI region by using the mesoflaps. Loth et al. (2004) employed the mesoflaps to control the normal SWBLI generated in a Mach 2 inlet. They showed that the mesoflaps caused a modest improvement in the pressure recovery of the inlet without significantly altering the inlet flow uniformity. By comparing the performance of the mesoflaps with a conventional bleed system, they found that the pressure recovery caused by the mesoflaps was lower than that of a conventional bleed system.

1.5.2 Active control devices:

Active control of the SWBLI is more desirable than passive control because it enables one to design a control scheme so that the actuation is performed only when required. This prevents a permanent interference of the control device with the flowfield and hence reduces the drag penalty associated with passive control devices. The common active control strategies that have been studied for the last several years are boundary layer suction and blowing and vortex generator jets. Viswanath (1988) in his review classified jet injection for SWBLI control into U-type and D-type jets. The jets that are injected upstream of the separation shock are termed U-type jets and the jets that are injected downstream of the separation shock into the recirculation region are termed D-type jets. U-type jet injection studies are more common in the literature than D-type injection. Peake (1966) studied the use of wall jets control of separation from shock generated using a flap in M = 1.8 flow. The flap could be deflected from 0 to 12°. The authors reported that they were

able to prevent separation till a static pressure ratio of 3 using a U-type wall jet. They also reported that the optimal location of the wall jet was 6δ upstream of the compression corner. Viswanath et al. (1983) employed both U-type and D-type wall jets to suppress the separation in an M = 2.5 flow. They demonstrated that D-type wall jets were more effective in suppressing separation compared to U-type wall jets. Selig and Smits (1991) performed control of a SWBLI generated by a 24° compression ramp placed in an M = 2.84 flow by pulsed jets injected normal to the flow. The jets were injected from both upstream of the separation shock and into the recirculation bubble at frequencies of order a few kHz. They demonstrated that the separation shock unsteadiness frequency got locked to the pulsing frequency of the jets upon jet injection. They reported that they could achieve control from both U-type and D-type jets. They also indicated that the effectiveness diminishes with reducing blowing ratio of the jet.

One of the most important types of jets that are being used for separation control is the pitched/skewed jets or vortex generator jets. Incidentally the first use of pitched/skewed jets was made by Wallis (1960) for reducing separation in a supersonic flow. They observed that the pitched/skewed configuration generates streamwise vortices that are embedded in the flow. Johnston and Nishi (1990) studied the characteristics of pitched and skewed jets in subsonic flows in detail. They observed that the vorticity field created by the pitched/skewed jets was very similar to those generated by vortex generators and hence they coined the term "vortex generator jets". These vortex generator jets have found extensive application for separation control in subsonic boundary layers. Compton and Johnston (1992) studied the effect of changes in pitch and skew angles on the strength of the streamwise vorticity and found that a pitch angle between 30-60°and skew between 60 – 90° produces the

maximum strength. Zhang and Collins (1997) studied the role of jet-to-free-stream velocity ratio on separation control effectiveness. They found that the VG jets that were embedded inside the boundary layer caused the maximum effect. Bueno et al. (2006) employed steady and pulsed VG jets at pulsing rates of 10 and 100 Hz to control SWBLI generated by a semi-infinite cylinder placed in an M = 2 supersonic flow. They performed phase-locked PIV measurements to study the interactions. They showed that the boundary layer thickness at a location just downstream of the jet injection increases, but showed a thinning of the boundary layer farther downstream. They also showed a downstream shift in the separation shock with pulsed and continuous injection of jets.

1.6 Objectives of the current study

Control of shock wave / boundary layer interaction has certainly come a long way in the past 50 years. However, still the control authority is considerably limited. It is also desired to have an active control device to develop a control scheme, in order to minimize parasitic drag penalty. Pulsed VG jets as an active control device is a promising option as demonstrated by several previous researchers. However the problem with using solenoid valves to modulate te jet flow rate is that they are limited to frequencies of less than a few hundred Hz, which is lower than the low frequency motion of the separation bubble unsteadiness ($\mathcal{O}$ (kHz)). The objective of the present research is to study a high-amplitude high-frequency pulsed jet system using arc discharges (referred to as "pulsed-plasma jet" in this work). The design of the actuator is very similar to that of the "spark-jets" developed by Grossman et al. (2003), described earlier. The velocity and thermal characteristics of the pulsed-plasma jet issuing into stagnant air at a pressure of 45 Torr is studied in order to assess its

effectiveness for SWBLI control. A detailed phase-averaged and time-resolved study of a Mach 3 SWBLI control using the pulsed-plasma jet array is made using schlieren imaging. The effect of forcing on the shock-induced separation bubble unsteadiness would also be studied quantitatively using wall-pressure fluctuation measurements.

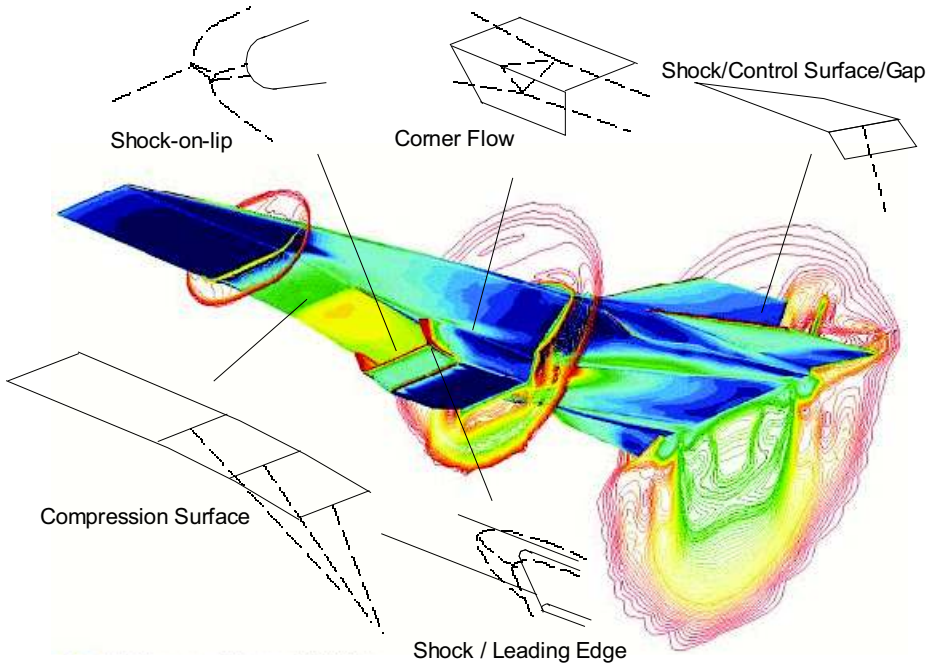

Courtesy: Nasa/Langley Research Center (Vehicle), Jackson L.R. et al. (SWTBLI examples)

Figure 1.1: Examples of shock wave / boundary layer interaction in a hypothetical hypersonic air vehicle

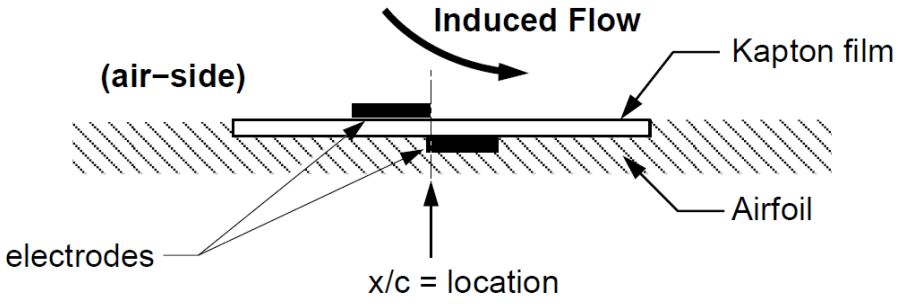

Figure 1.2: Schematic of a DBD actuator. The figure is reproduced from Corke and Post (2005)

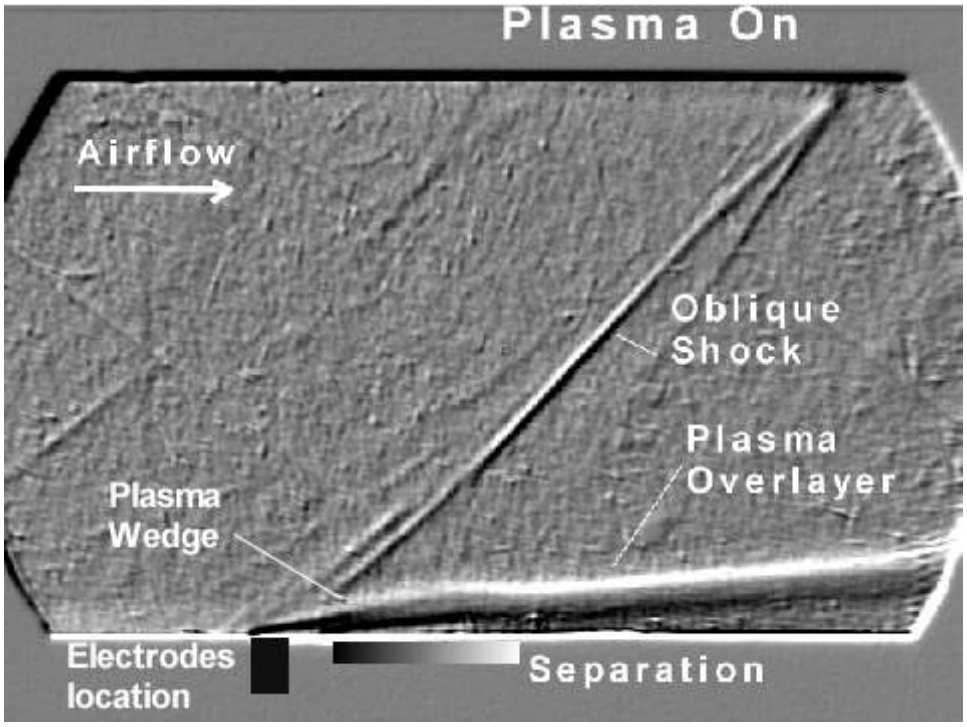

(a)

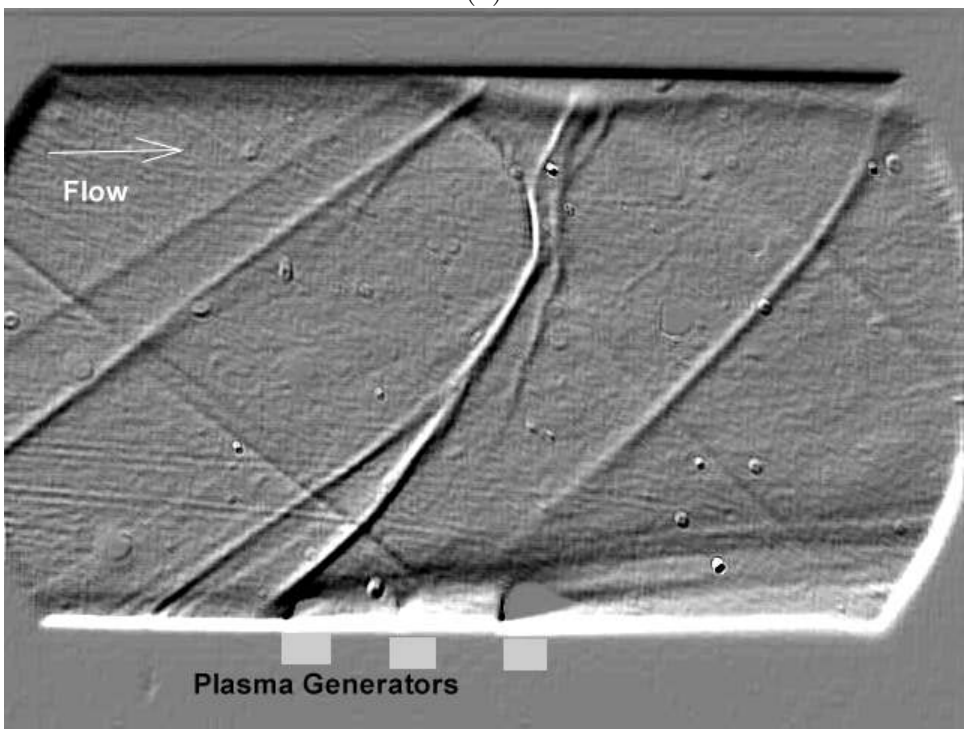

(b)

Figure 1.3: Thickening of the boundary layer (a) and global separation (b) caused by a filamentary arc discharge. The figure is reproduced from Leonov et al. (2003).

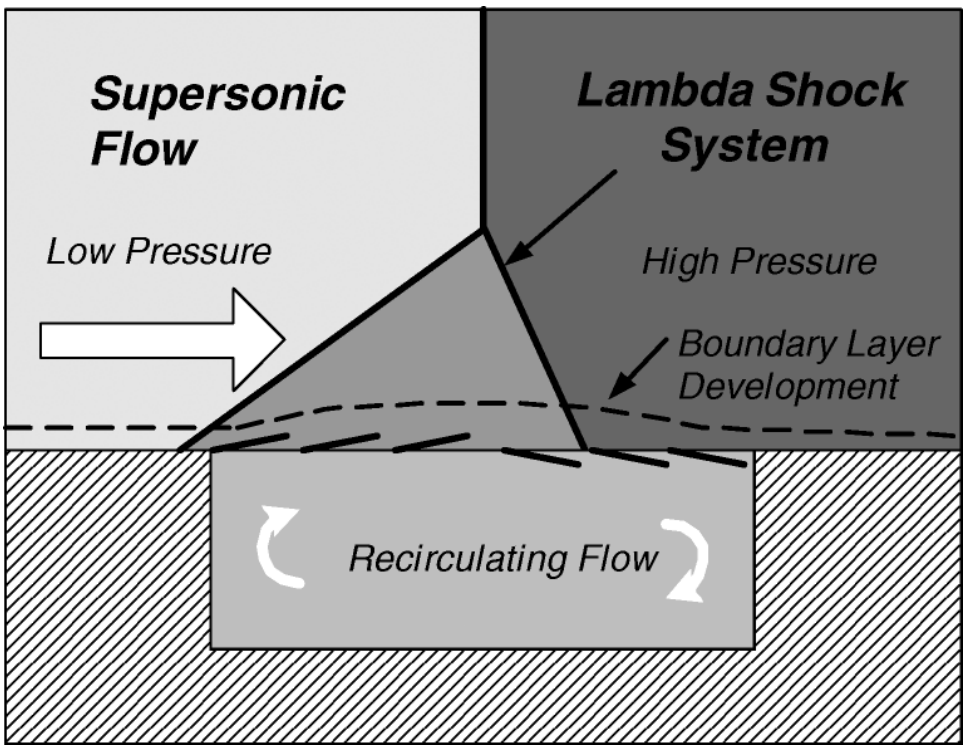

Figure 1.4: Schematic of the working of an aerodynamic mesoflap (reproduced from Lee et al. (2004))

Chapter 2

Design of the pulsed plasma jet actuator

2.1 Principle of operation

The pulsed plasma jet operates by striking a short-duration, high-current electric arc in a closed cavity containing a small orifice. The gas inside the cavity is electro-thermally heated by the discharge, which leads to a rapid increase in pressure within the cavity. This high-pressure gas issues through the orifice and forms the pulsed plasma jet. The velocity of the plasma jet is related to the cavity pressure, which in turn depends on the rate of deposition of energy. Inside the cavity the compression process that drives the jet is followed by a rarefaction wave that draws fluid back into the cavity, and hence recharges it for the next pulse. Since the actuator operates without an external gas supply, the pulsed plasma jet is a synthetic jet, which has zero net mass flux across the orifice.

2.2 Construction and design

The schematic of a single pulsed plasma jet actuator with wall normal injection is shown in figure 2.1. This design is a modification of the design used in Grossman et al. (2003). A cylindrical cavity of 2.4 mm dia. was made in a ceramic plate and electrodes (2.4 mm dia.) were inserted from opposing sides to form a cavity bounded by the electrodes. Different materials (alumina, Macor and boron nitride) were tested for making the body of the cavity. The thermal conductivity of the materials are listed

in table 2.1. Based on the jet exit velocity of the pulsed plasma jet and the ease of machining Macor and boron nitride were both used during the experiments. Whereas the Macor cavity was used to make a detailed study of the static performance, the boron nitride cavity was employed for flow control studies. It was found that the plasma jet issuing from the boron nitride cavity had a jet exit velocity about 30% higher than that of the Macor cavity, while the dependence of the performance on geometric and discharge parameters was identical in both the cavities.

The electrodes that formed the faces of the cavity were made of copper. Tests were also performed using steel as the electrode material. No noticeable change in jet exit velocity was noticed on changing the electrode materials. The gap between electrodes could be varied between 5 mm to 11 mm (0.2 to 0.4 inches) to provide different cavity volumes. A small hole, of 1.7 mm dia (#49 drill), was drilled in the middle of the cavity. It should be noted that no tests were performed to study the influence of the position of the orifice with respect to the electrodes. The tip of the cathode was sharpened to decrease the breakdown voltage. The lead wires that connect the electrodes to the external power supply were crimped onto the electrode, thus eliminating any soldering between electrodes and wires. Soldering was avoided becase during operation the electrodes would get much hotter than the melting point of the solder.

Different jet injection angles were fabricated for testing. Figure 2.2 shows the CAD drawing of the actuator with wall-normal injection of the pulsed plasma jet. Figure 2.3 shows the CAD drawing of the actuator with pulsed plasma jet injection pitched at an angle (α) = 60 deg with respect to the wall normal direction. It can be seen that the orifice for the pitched injection is located exactly at the middle of the actuator. This means that the location of the orifice inside the cavity for the pitched

Name of the Material	Thermal Conductivity (W/°K)
Boron Nitride	27-31
Macor	1.46
Alumina (Al_2O_3)	40

Table 2.1: Thermal conductivity of cavity materials

injection actuator is slightly off center. It was found from the experiments that this does not cause any noticeable change in the actuator performance. Figure 2.4 shows the CAD drawing of an actuator with jet pitch angle of $\alpha = 45\,\text{deg}$, and skew angle of $\beta = 90\,\text{deg}$. The definitions for pitch and skew angles are shown in fig 2.5. It can be seen from the CAD drawings that the pitched-skewed plasma jet actuator is longer (length = 1.2") compared to the normal injection and pitched unskewed injection actuator (length = 0.8"). The reason for this is that the normal and pitched injection actuator were used for injecting plasma jets from both upstream and downstream of the separation shock, and it required a smaller actuator to enable this. Even though the dimensions of the actuators are different, the separation between cathode and anode, cavity volume and cross sectional area of the cavity are identical for all the jet injection cases tested.

2.3 Electrical Design

The schematic of the circuitry of the pulsed plasma jet is shown in fig. 2.6. A high voltage DC power supply (Spellman, SL2PN1200), rated at 2 kV and 1.2 kW (max), was employed to provide the breakdown voltage ($\approx 1.8\,kV$) and the current to drive the circuit ($600mA$, avg). A capacitor ($0.22\,\mu F$) was charged by the DC power supply until the discharge was formed between the electrodes. Upon breakdown, the capacitor provided the high current burst required to sustain a non-equilibrium

arc between the electrodes. The rise time of the discharge current was measured to be about $3\,\mu s$. A ballast resistor was used between the capacitor and anode, which limited the current that flows through the pulsed plasma jet circuit and hence determined the strength of the jet. For a discharge current of $2\,A$, the value of the ballast resistor was about $1\,k\Omega$.

A timing circuit, which included digital delay generators (Berkeley Nucleonics, model 500B) and power MOSFET switches (STMicroelectronics, Model: STP4N150), was made to repeat the charge-discharge cycle at kilohertz rates. A detailed description of the switching circuit is given in the next subsection. Peak discharge currents (discharge set-point currents) ranging from 1.2 to 11 A were tested. The typical pulse width of the discharge was about $20\,\mu s$, and above this value the jet velocity was independent of the pulse width. During the experiments to characterize the performance of the pulsed plasma jet in the stagnant chamber, the pulse width of the discharge was set at $20\,\mu s$. However for the experiments in which the pulsed plasma jet is employed to control the separation shock, the pulse width was varied between 20 and $50\,\mu s$. Pulsing frequencies up to $5\,kHz$ were achieved at $2\,A$ discharge current per cavity. For flow control studies, the majority of the tests were performed at pulsing frequency between 1 and $3\,kHz$.

2.3.1 Switching circuit

One of the most important components used for generating plasma jet pulses is the Metal Oxide Semiconductor Field Effect Transistor (MOSFET) switch. The MOSFET switch operates such that when a high voltage ($> \mathit{threshold\ voltage}$) is applied across the gate and source (V_{GS}) terminals, the channel between drain and source terminals becomes conductive. This happens because of the "field effect",

wherein the applied voltage between gate and source terminals creates a pool of electrons which can freely migrate between drain and source. This causes the channel between drain and source to become conductive, which corresponds to a closed switch. However when the applied voltage is below the threshold value, the electrons in the channel are depleted, which makes the resistance between drain and source very high and this corresponds to an open switch.

One of the major drawbacks of the MOSFET switch is that the maximum voltage and current that the switch can handle are very small ($\mathcal{O}(10\,V\,and\,100\,mA)$). With the advent of the power MOSFETs the maximum voltage has been improved to from a few hundred volts to a few kVs and the maximum current has been improved to few amperes. For switching higher voltages and currents normally Insulted Gate Bipolar Transistors (IGBT) are used. The disadvantage with using IGBTs compared to MOSFET switches is that the IGBTs take a very long (few milliseconds) time to transition to the open state from the closed state.

The MOSFET switch used for the present application is from STMicroelectronics Inc. (Model STW4N150). The performance chart of the MOSFET limits its operation to $1.5kV$ and $4A$ current. Note that in the present study switching of much higher current (up to $11\,A$) was achieved by adding adequate heat dissipating fins to the MOSFET switch and increasing the gate voltage (V_{GS}) to about $13\,V$. However, occasionally the switch would still get damaged because of excessive heating. The damaged MOSFET switch was identified by checking the resistance between gate and source, drain and source and gate and drain without connecting to any circuitry. The values of the resistance would be substantially smaller (few tens of $k\Omega$) when damaged, compared to the working MOSFET switch, whose resistance values would be of the order of few $M\Omega$s.

A schematic of the circuitry employed for switching is shown in fig. 2.7. The schematic shown is for an individual pulsed plasma jet circuit. When an array of pulsed plasma jets were used, multiple copies of the same switching circuitry were used. The lead from the cathode was connected to the drain terminal of the MOSFET switch. The gate terminal of the MOSFET switch was connected to a function generator (Berkeley Nucleonics Inc. Model 500B) through an optoisolator. The optoisolators used are manufactured by Optek Semiconductors (Model OPI1270). It was found that these isolators are superior to other optoisolators because the fiber optic cable that connects the LED source to the photoresistor is not embedded inside the IC chip as it is in conventional optoisolators. An optoisolator consists of an LED The function generator is capable of providing square pulses whose amplitude, duty cycle and frequency could be controlled. The MOSFET switch was closed during the time when the voltage from the function generator was above the threshold voltage ($4.6\,V$). The source of the MOSFET switch was connected to the ground through a $1.2\,\Omega$ ($2\,W$ maximum power) resistor. The current through the pulsed plasma jet was measured from the voltage drop across this $1.2\,\Omega$ resistor. The ground was common to all components of the circuitry, namely the high voltage source, capacitor, the MOSFET switch and the function generator.

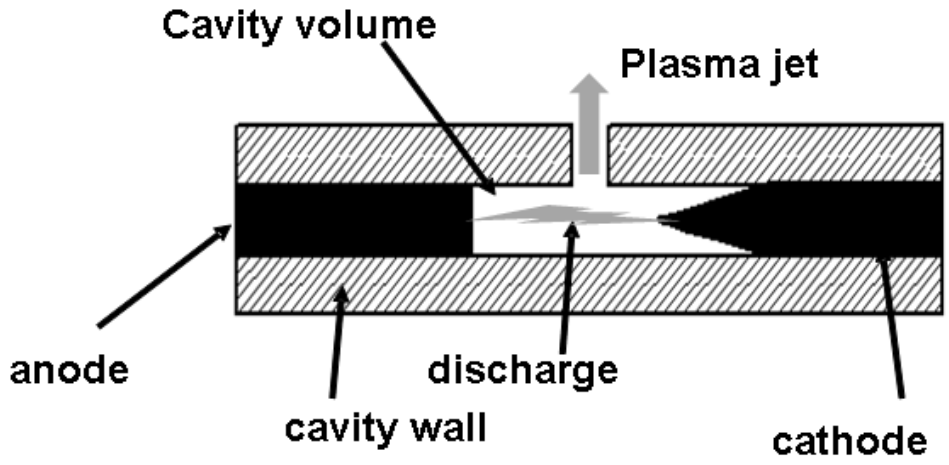

Figure 2.1: Schematic of a pulsed plasma jet actuator with normal injection

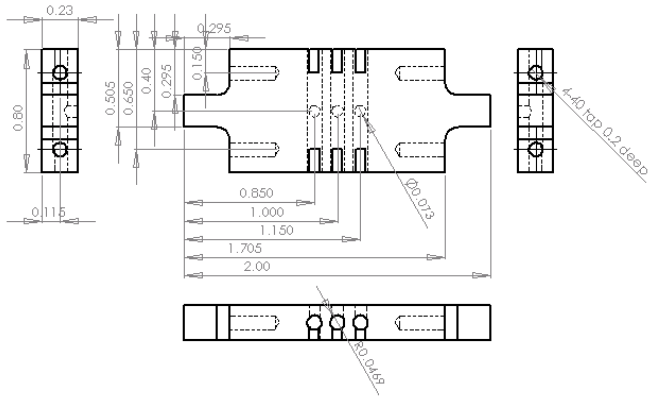

Figure 2.2: CAD drawing of a normal injection pulsed plasma jet

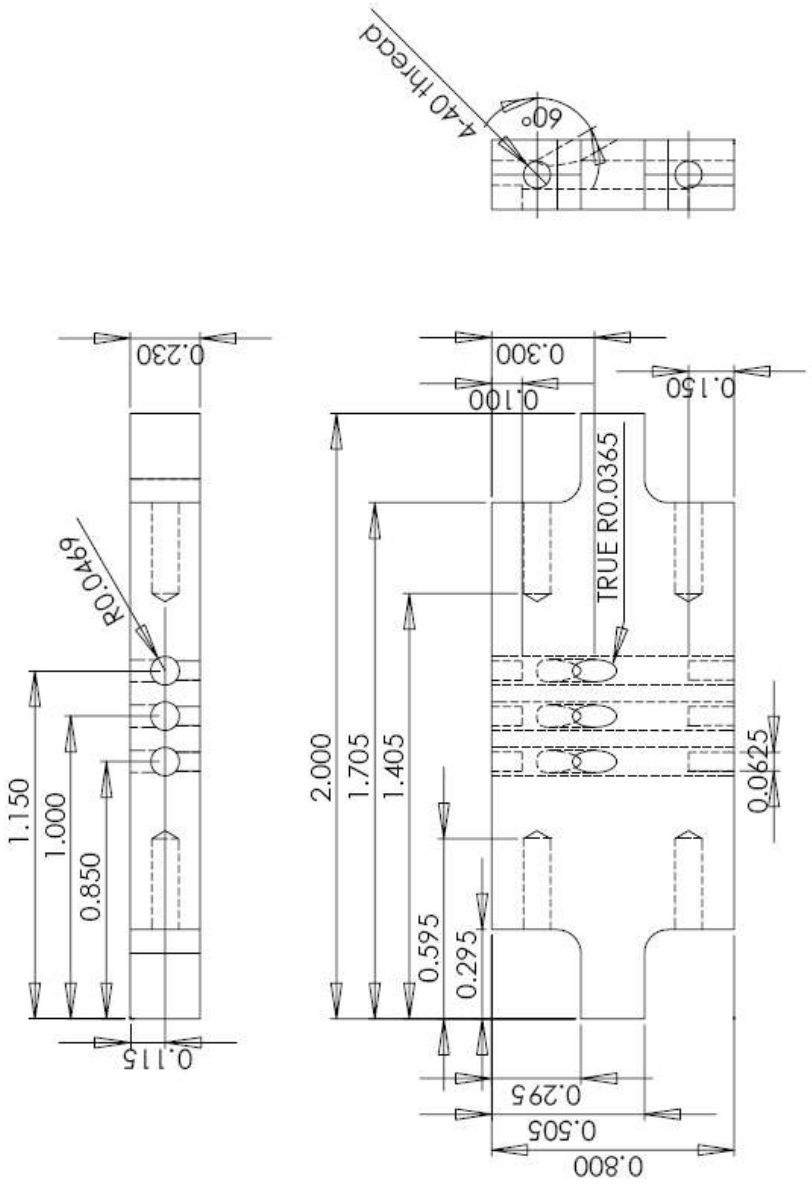

Figure 2.3: CAD drawing of 30° pitched injection actuator

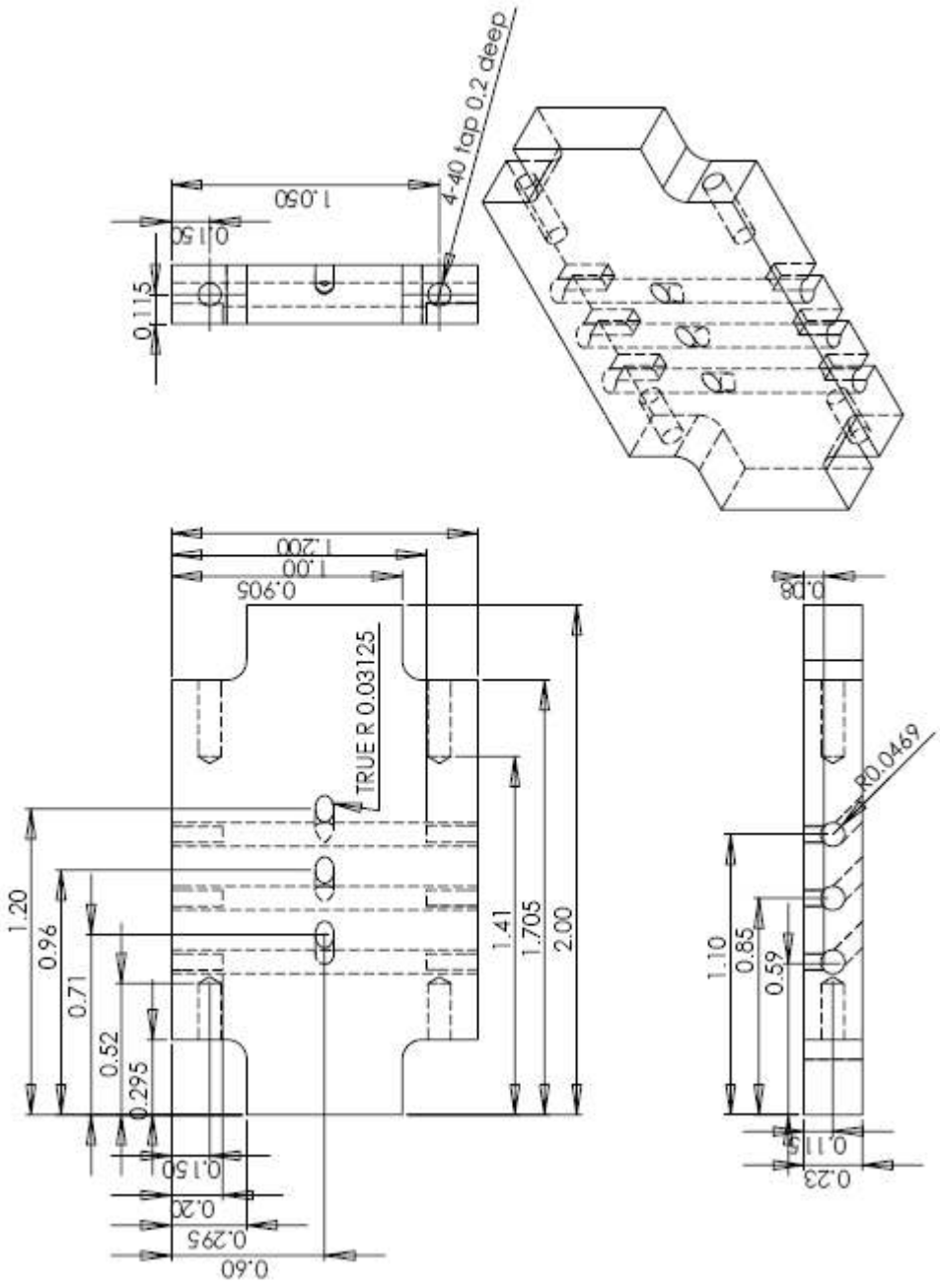

Figure 2.4: CAD drawing of a 45° pitched and 90° skewed pulsed plasma jet actuator

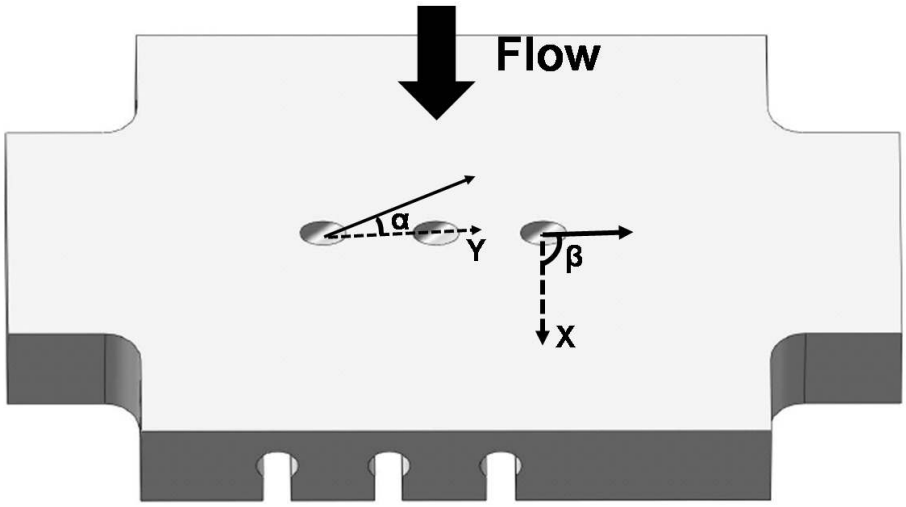

Figure 2.5: Schematic showing the definition of pitch and skew angles

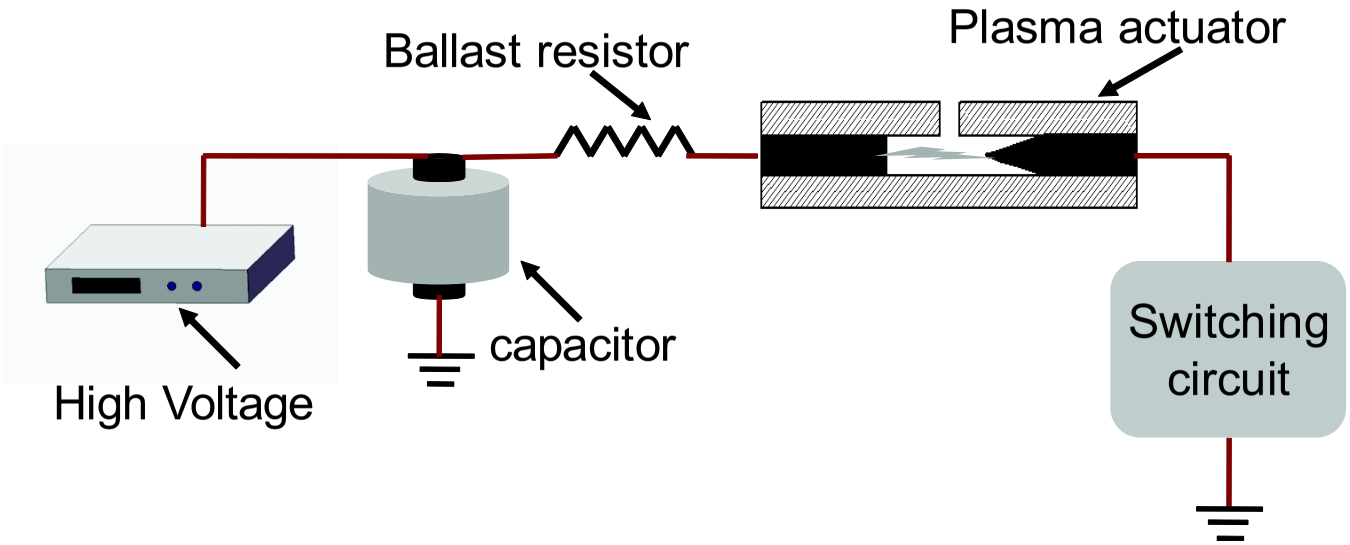

Figure 2.6: Schematic of the circuitry of the pulsed plasma jet actuator

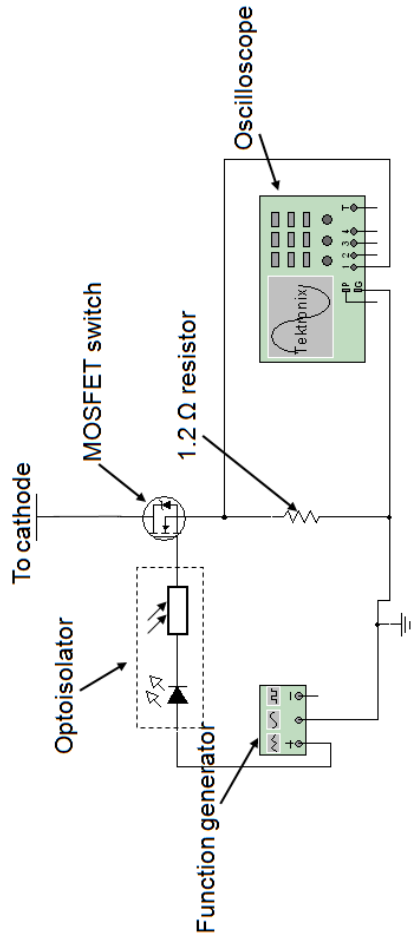

Figure 2.7: Schematic of the switching circuitry

Chapter 3

Experimental Program

3.1 Static performance of the pulsed plasma jet

All experiments that study the static performance of the pulsed plasma jet were performed in a stagnant vacuum chamber made of acrylic. The chamber was evacuated to 45 torr to match the static pressure of the wind tunnel in which the pulse plasma jet was employed for separation shock control studies. The imaging was done through a $100\,mm \times 25\,mm$ fused silica window placed roughly at the center of the chamber. The actuator used for testing was placed on a stand mounted inside the chamber. This stand raised the actuator close to the center of the chamber to facilitate optical diagnostics of the pulsed plasma jet. The wires from the actuators were drawn out of the vacuum chamber through tiny holes made at the bottom of the chamber. The holes were plugged with jewelers' wax in order for the chamber to sustain the vacuum.

3.2 Separation shock control studies

3.2.1 Wind Tunnel facility

The experimental work was conducted in a Mach 3 wind tunnel located at The University of Texas at Austin. Figure 3.1 shows the schematic of the tunnel showing the relative location of the splitter plate, the actuator plate and the compression ramp. A detailed drawing of the wind tunnel and its components are given in Lachney (1995).

The wind tunnel test section has a cross sectional area of $5\,cm \times 5\,cm$ and a length of $40\,cm$. An acrylic splitter plate extended from the plenum section into the test section. The plasma actuator was placed in a plate that mounted at the trailing edge of the splitter plate. The compression ramp was mounted on a plate that was attached to the trailing edge of the plasma actuator plate. Pressurized air from a $500\,m^3$ high-pressure tank was fed to the tunnel and was discharged into a $1000\,m^3$ vacuum tank. The test section static pressure was maintained at $45\,torr$ for all the cases studied. The incoming boundary layer was allowed to undergo a natural transition to a fully developed turbulent boundary layer. The boundary layer profile was measured in this tunnel for different stagnation pressures in order to characterize the change in boundary layer parameters with changes in the stagnation pressure. Table 3.1 lists the measured boundary layer parameters at different stagnation pressures. Similar values of boundary layer parameters were also reported by previous researchers who used this tunnel (e.g. Lachney (1995); Sanders (1995); Smith (1995)). However, the boundary layer profile measurements reported earlier had a relatively coarse spatial resolution ($\approx 0.75\,mm$). The new measurements reported in this work are better resolved spatially ($\approx 0.5\,mm$). The current measurements clearly show that boundary layer parameters should be relatively constant for small changes in the stagnation pressure that happens during the experimental runs.

For the flow control application employed in this study the boundary layer thickness was approximately $4.5\,mm$ and the Reynolds number based on momentum thickness, $Re_\theta = 3300$. The boundary layer profile scaled on inner and outer scales at the operating conditions is shown in fig 3.2. The friction velocity at the operating conditions was $u_\tau = 15m/s$. The incoming boundary layer was turbulent as observed from the boundary layer profile; however, the slope and the offset of the logarithmic

Stagnation pressure ($\times 10^5\, kPa$)	Static pressure ($torr$)	Boundary layer thickness (δ)(mm)	Momentum thickness (θ)(mm)	Re_θ
1	21	2	0.13	1100
1.8	45	4.5	0.26	3300
2.7	69	4.5	0.26	5500

Table 3.1: Boundary layer parameters at different stagnation pressures

region have not converged to that of a fully developed turbulent boundary layer. This indicates that this is an evolving turbulent boundary layer in which the scales of turbulence are not fully developed.

3.2.2 Pulsed plasma jet actuator array for supersonic flow control

An array of three plasma jets was used for the flow control studies presented here. The individual plasma jets were separated by $4\, mm$ from one another. The typical operating discharge current for the flow control study was $3.9\, A$ per individual plasma jet with a pulse width between 20 to $50\, \mu s$. Different geometries of jet orifices were studied to optimize the geometric parameters for the maximum effect on the separation shock. The pitch angle of the jet was varied from 90°(normal injection) to 30°. The skew angles that were studied were 0° and 90°. The different geometries and the corresponding injection locations are tabulated in table 3.2. A schematic of the pulsed plasma jet injection for flow control application is shown in figure 3.3.

3.2.3 Assembling the facility

In order to achieve a high degree of flexibility in changing the actuators, a modular assembly was designed and fabricated. An illustration of the design is shown

Configuration	Pitch angle (°)	Skew angle (°)	Injection scheme (Upstream/Down-stream of separation shock)	Injection location (from the compression corner)
Normal	0	0	US/DS	$10\delta/1.7\delta$
Pitched	30	0	US/DS	$10\delta/1.7\delta$
Pitched	-30	0	DS	1.7δ
Pitched and skewed	45	90	US	10δ

Table 3.2: Table showing the various geometric configurations of the pulsed plasma jet and injection locations tested

using the CAD drawing in figure 3.4. It can be seen that there are filleted slots at the edges of the actuators. There are also four $4-40$ threaded holes close to the corners of the actuator. Similar slots and threaded holes were also made in the splitter plate of the wind tunnel. The actuator was attached to the splitter plate through a union made of aluminum or acrylic that fits snug in the slot. A similar procedure was also adopted in assembling the other components to the actuator. This way of "linking" different components enabled changing and replacing the actuators and other components. A frequent change of actuators was normally necessitated because the copper electrode that was used in the actuator often became corroded by the discharge. Once the copper electrode became corroded, the plasma discharge could not be generated even with the maximum voltage that could be provided by the power supply. Another reason for frequent change in actuator was that a substantial portion of this study was a developmental effort of the pulsed plasma jet; hence, different geometric configurations had to be tested in the course of this work.

3.2.4 Bottom housing

It was earlier mentioned that that the pulsed plasma jet actuator was mounted at the trailing end of the splitter plate (fig. 3.1). This required that the wires from the electrodes pass through the lower half of the test section. However, these wires caused a cylindrical obstruction to the incoming flow and as a result, a bow shock was formed in front of the wires. When multiple wires passes through the lower part of the test section, the bow shocks generated caused the tunnel to unstart. Hence, a housing (referred to in this work as the "bottom housing") was designed and fabricated to pass these wires through. The schematic of the bottom housing and a CAD drawing are shown in fig 3.5 and 3.6. The housing was built out of acrylic so that there was no

discharge between the wires and the housing. The bottom housing was about 3 mm (0.125") thick. There were six through holes in the housing, one for each electrode wire as shown in the schematic. The diameter of the hole was such that there was enough clearance for the wires from the electrodes to pass through. The electrode wires used were solid 24 gauge wires whose outer diameter was about 1 mm. The schematic and CAD drawings of the housing (figs. 3.5 and 3.6) also show the clearance holes for the wires from the transducers to pass through. These holes were used only during pressure measurements. The housing was mounted to the center plate leading edge from below using 1 inch long #0 bolts. It should be noted that the included angle of the housing wedge was about 10°; hence the strong bow shocks that were initially formed in front of the wires were replaced by a weak oblique shock in front of the housing. This design made it considerably easier to start the tunnel.

Figure 3.5(b) shows the assembly of the bottom housing with the actuator. Figure 3.5(b) also shows the plate next to the actuator plate with a few holes in it. This plate is the pressure transducer housing that was used during pressure measurements for mounting the transducers flush with the splitter plate. This pressure transducer housing was replaced with one without holes during other experiments.

3.2.5 Compression corner

Two different compression corners were employed for this study. Some of the preliminary studies that characterized the average performance of the pulsed plasma jet for separation shock control were done with a 30° compression corner. This compression corner was chosen because the separation shock generated by this compression corner was quite strong. The demonstration of the control of the shock of this strength would clearly indicate the strength of actuation. This compression

corner had a span of $25\,mm$ (1"), which was about half the width of test section, and thus the separation shock was significantly three dimensional.

Later studies that used planar laser scattering (PLS) and schlieren imaging was done with a 24^o compression corner. This compression ramp had a span of $37.5\,mm$ (1.5"), which spans $\frac{3}{4}$ of the tunnel width. The height of the ramp was $6.25\,mm$ (0.25"), which was about 1.5 times the boundary layer thickness (δ). The trailing part of the ramp had a 30° surface so that there was very little flow separation. Figure 3.7 shows the surface streak visualization of the separation bubble generated by a 24° compression corner using kerosene and titanium dioxide mixture. From the figure, it can be seen that the separation bubble was relatively two dimensional. The separation location was about 3δ upstream of the compression corner. It should be noted that no fences were added to the compression ramp during the study, which caused an overall spanwise curvature to the separation shock at the corners (not seen in the figure). The pulsed plasma jets were placed near the spanwise centerline so that the jets interact with the "two dimensional" portion of the separation shock.

3.3 Diagnostic techniques

3.3.1 Optical Emission Spectroscopy

Optical emission spectroscopy was used to obtain temperature information in the plasma discharge. These measurements were performed for normal jet injection cases only. The light emitted from the discharge was collected with a $63\,mm$ focal length confocal lens ($50\,mm$ diameter) through a glass side window and was focused on to a fiber optic cable with a 400 μm core. The orientation of the lens was such that it imaged directly into the cavity, i.e., along the jet axis. The fiber optic was connected to the entrance slit ($5\,\mu m$ slit width) of a 1/4 m imaging spectrometer (Spectra-

Physics, MS260i). The nominal spectral resolution of the setup was 0.13 nm with an 1800 lines/mm grating. A study was performed to measure the spatial resolution of the optical setup by scanning a 25 μm pin hole, which was back-illuminated by a flash lamp across the object plane. The spatial resolution was limited by the fiber optic cable core diameter and the magnification of the system, and was approximately 400 μm.

3.3.2 Schlieren imaging

Schlieren imaging was performed to characterize the static performance of the pulsed plasma jet and to study the interaction between the pulsed plasma jet and the separation shock. Schlieren imaging is one of the oldest and most-widely used techniques for flow visualization in high-speed flows. It is based on the deflection of light rays by gradients in index-of-refraction and provides line-of-sight integrated details about the index-of-refraction gradients. It is known that the index-of-refraction in gases is related to the density, and hence, schlieren imaging gives information about the density gradients. The variation in intensity of schlieren is related to the index-of-refraction by the following equation (Merzkirch (1987)):

$$\frac{\Delta I}{I} = L \int (\frac{\partial}{\partial x} + \frac{\partial}{\partial y}) \, ln\,(n)\, dz \tag{3.1}$$

where I is the intensity with no gradient, ΔI is the change in intensity due to the presence of gradient, n is the index-of-refraction and L is the length of the phase object (wind tunnel width in the present study). The density can be related to the index-of-refraction, in gases, using the Gladstone-Dale relation:

$$n = 1 + K\rho \tag{3.2}$$

where K is the Gladstone-Dale constant for the particular gas and ρ is the density of the gas. Thus, it is clear that the schlieren effect is proportional to the first derivative of the index-of-refraction and the density of gas. In high speed flows, there are density gradients present due to the boundary layer and separation shock.

In the current experimental setup, a high brightness LED lamp was used as the light source. The pulse duration of the lamp was short enough to freeze the flow during illumination. The light beam was passed through an iris with less than $1\,mm$ opening to provide a point source. The iris was placed at the focus of a $750\,mm$ (30") focal length convex mirror which produced a collimated beam. The collimated beam was made to pass through the test section. After passing through the test section, the beam was focused using a mirror similar to the collimating mirror. A knife edge was placed at the focus of the converging beam. The knife edge was raised half way into the focused beam to achieve maximum sensitivity to density gradients. The image was captured using a CCD or CMOS camera that was electronically shuttered to reduce plasma luminosity.

Schlieren imaging was performed at two frequencies, $60\,Hz$ and $10\,kHz$. The low frequency imaging ($60\,Hz$) was conducted in order to obtain phase average information about the interaction of the pulsed plasma jet with the separation shock. The high frequency imaging ($10\,kHz$) was performed to obtain time resolved motion of the separation shock while it interacts with the pulsed plasma jet. For the $60\,Hz$ schlieren imaging the light source used was a high brightness LED lamp manufactured by EG&G Optoelectronics. The pulse duration of the light pulse was about $2\,\mu s$. A custom-made pulsing circuit was used to operate the LED lamp. The images were captured using a CCD video camera (Pulnix progressive scan Model: TM-6710) capable of acquiring images at $60\,fps$ (maximum). The camera resolution was

$512 \times 512\,pxl$ and the spatial resolution achieved was roughly $80\,\mu m$ per pixel. For the 10 kHz schlieren imaging, the light source employed was a high brightness LED lamp (Innovative Sciences Inc.) capable of providing high intensity light pulses at a maximum rate of 50 kHz. The pulse duration of the light pulse was $6.3\,\mu s$, which was short enough to freeze the motion of the flow. The images were acquired at 10 kHz using a CMOS camera (Photron FASTCAM-Ultima APX) and the resolution was $512 \times 256\,pxl$. The spatial resolution achieved was about $80\,\mu m$ per pixel.

3.3.3 Planar Laser Scattering

Planar laser scattering imaging of a seeded CO_2 fog was performed to track the average motion of the pulsed plasma jet at the wall normal locations of $\frac{y}{\delta} = 0.2$ and 0.45. A frequency doubled Nd YAG laser (Spectra Physics PIV400) was employed to provide 532 nm light beam in 10 ns pulses at 10 Hz. The energy per pulse was about $45\,mJ$. This beam was passed through a 750 mm focal length convex lens and 45 mm focal length plano-concave lens in order to form a laser sheet. The thickness of the laser sheet was measured by scanning the spatial intensity profile using a knife edge and was found to be about 0.3mm. The thickness of the sheet did not vary significantly across the field of view. The laser scattering images were acquired using a Kodak Megaplus ES 1.0 camera fitted with a 50 mm focal length lens and a 5 mm extension ring. The extension ring was needed to reduce the working distance of the imaging system. The field of view of the image was $5\,cm\,(streamwise) \times 2\,cm\,(spanwise)$, which in terms of boundary layer thickness is $10\delta \times 4\delta$. In the streamwise direction, the imaging domain extended from about 2δ upstream of the compression corner to 12δ upstream of the compression corner. The plasma actuator plate and subsequent splitter plates were painted black using a flat black paint in order to minimize the

background. The average background intensity was negligible when compared to dark noise of the camera.

Compressed carbon dioxide gas was seeded in small amounts (<2%) far upstream ($\approx 5\,m$) of the settling chamber to allow for complete mixing with main flow. A schematic of the experimental set up is shown in fig. 3.8. The seeded CO_2 gas undergoes isentropic cooling while it expands through the nozzle of the Mach 3 tunnel to form a very fine fog ($\mathcal{O}(10\,nm)$) of solid CO_2. These particles cause the scattering of the light sheet that would be detected by a Kodak Megaplus ES 1.0 camera. Considering the small size of the scattering particles, the scattering regime roughly falls under the Rayleigh regime.

An estimation of the change in Mach number of the tunnel due to the heat addition resulting from the phase transition of gaseous to solid CO_2 was also made. The heat of sublimation of CO_2 is 571 kJ/kg. For a seeding density of 2% used in the experiments, the mass flow rate of CO_2 was 0.01 kg/s. Assuming a complete phase transition, the heat released during the solidification is about 5.71 kJ/s. For this heat addition and assuming an initial Mach number of 2.85, the modified Mach number due to heat addition as calculated from Rayleigh flow theory is about M = 2.7. Hence, it can be seen that there was only a relatively small change in the flow condition with the addition of CO_2 during PLS imaging.

3.3.4 Particle Image Velocimetry

The quantitative study of the interaction between the separation shock with the pulsed plasma jet was performed using particle imaging velocimetry (PIV). In a typical PIV experiment, the tracer particles, which are seeded into the flow, are illuminated by a laser light. The images of these particles are obtained at very short

intervals of time using a frame straddled camera or multiple cameras. To obtain the displacement, two successive images are cross-correlated using one of several available techniques and the location of the peak in the cross-correlation corresponds to the displacement of the tracer particles. The velocity of the tracer particles can be found from the displacement and the time interval between images. Note that the tracer particles and their diameters should be determined with care so that the particles follow the flow. The Stokes number defined as the characteristic response timescale of the tracer particles to the flow time scale should be less than 0.5 (Samimy and Lele (1991)) for the particles to faithfully follow the flow. Otherwise, the PIV measurement will give the velocity of the particles, which might not necessarily be the flow velocity. A detailed description of the PIV measurement technique and data analysis is given in Raffel et al. (2001).

For the present experiments, the seed particles were produced using a six-jet atomizer (TSI model 9306 six-jet atomizer), which generates polydisperse seed particles at high concentration. Extra virgin grade olive oil was used in seeding and the nominal diameter of the olive oil particles produced by the atomizer as quoted by the manufacturer was 0.6 μm. The seed particles were injected in the same manner as the CO_2 gas for the PLS imaging described earlier. These particles were illuminated by a laser sheet (thickness $\approx$ 1 mm) produced by a frequency doubled Nd-YAG laser and the scattered light was captured by a Kodak Megaplus ES1.0 frame straddled camera, stopped at $f_{\#} = 5.6$. A schott glass filter was also mounted in front of the camera in order to prevent the luminosity from the pulsed plasma jet from interfering with the PIV images. About 150 images were taken during each run, which corresponds to a tunnel run time of 15 seconds. Images from the camera were then transferred to a hard disk and were processed to compute the vector fields using LaVision's DaVis

7.2 software. Multipass processing algorithm was used starting with an initial interrogation window size of $64 \times 64\, pxls$ with 50% overlap to a final interrogation window size of 16×16 pixels with 50% overlap. The cross-correlation between the two images was found by using an FFT algorithm and the peak was found by Gaussian peak fit. The maximum pixel displacement was about 24 pixel, which corresponds to the freestream. The vector fields were validated and the missing vectors were interpolated using a 3×3 local mean technique. The resolution of the resulting vector field was about 0.5 mm × 0.5 mm, which corresponds to a resolution of $\delta/8 \times \delta/8$, in terms of boundary layer thickness δ. The number of spurious vectors was less than 4% in the region outside the boundary layer and separation bubble. However inside the boundary layer (close to the wall) and inside the separation bubble only about $50 - 60\%$ of the vectors were valid. This is because of the decreased density inside the boundary layer and inside the separation bubble, which leads to a corresponding drop in the seeding density. Because of the relatively poor quality of the vector field inside the separation bubble, only average flowfields are considered. About $50 - 100$ images were included for averaging in each data set.

3.3.5 Wall pressure fluctuation measurements

Fluctuating wall pressure measurements were made at several streamwise locations along the SWBLI region. Separate measurements of the wall pressure fluctuations were made with and without forcing. In both cases, fast-response pressure transducers were used. During pressure measurements with forcing, only a single pulsed plasma jet was employed. The pressure fluctuation measurements with and without forcing were made by using a high frequency response transducer manufactured by Kulite Semiconductor Products, Inc. (model XCQ-062-05A). The transducer had a

nominal diameter of 0.0625 inch and a silicon sensing membrane whose diameter as specified by the manufacturer was 0.71 mm. The natural frequency of the membrane was 150 kHz. Perforated screens above the diaphragm protected the transducer from being damaged by dust particles in the flow. However, the protective screen limited the frequency response of the transducer to about 50 kHz. These transducers were housed in a copper tube, which was inserted into the pressure transducer housing (shown in fig. 3.5 (b)) through one of the transducer holes of the bottom housing. The entire unit was mounted flush with the floor of the splitter plate. The signals from the pressure transducers were low pass filtered with a cut off at 50 kHz using Ithaco filters (model 4200). The filtered signals were digitized to 12 bits at a rate of 125 kHz with a data acquisition board (National Instruments AI-16E-4) installed in a Pentium 4 personal computer running LabVIEW software.

Measurement of wall pressure fluctuations without forcing was straightforward and did not require any additional procedures. However, modifications to the present experimental setup were required to make pressure fluctuations with forcing owing to the presence of charged species from the pulsed-plasma jet in the vicinity of the transducer. The problem arises because the transducer casing has to be grounded to minimize noise during measurement. This grounded casing drains the ions that convect past it. The ions thus attracted to the casing strike the sensing element of the transducer causing permanent damage to the transducer by causing:

1. loss of frequency response,

2. a permanent DC offset

3. loss of sensitivity to applied pressure

4. permanent physical damage to the sensing element because of heat load from the reacting ions

To protect the transducers from the incoming ions and obtain meaningful wall pressure fluctuation measurements, a second pulsed ground electrode was used upstream of the transducer. This electrode drained the incoming charged species before they could reach the transducer. A detailed description of the procedure is given in appendix A.

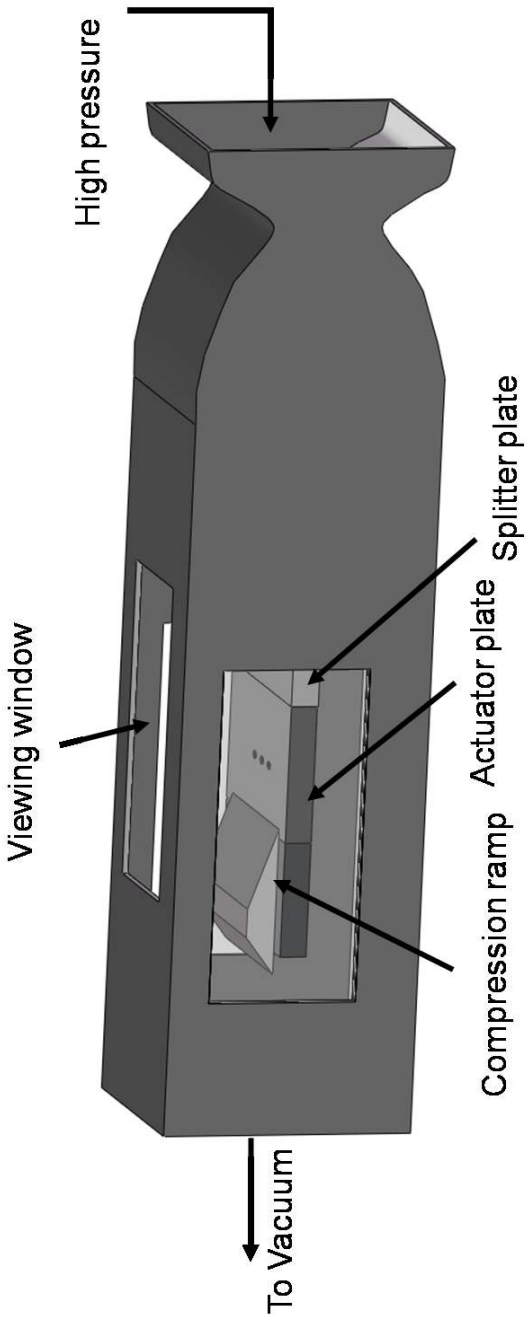

Figure 3.1: Schematic of the wind tunnel

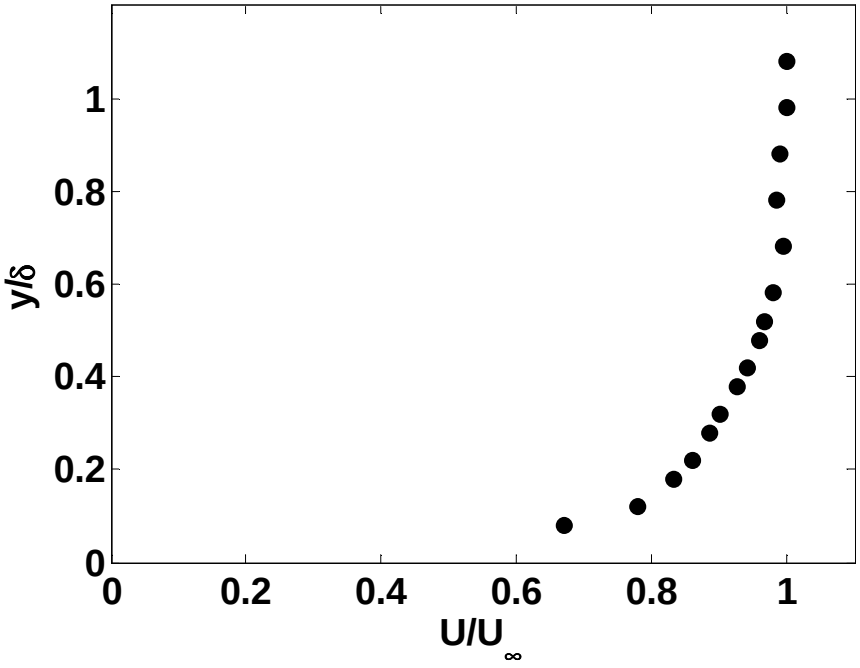

(a)

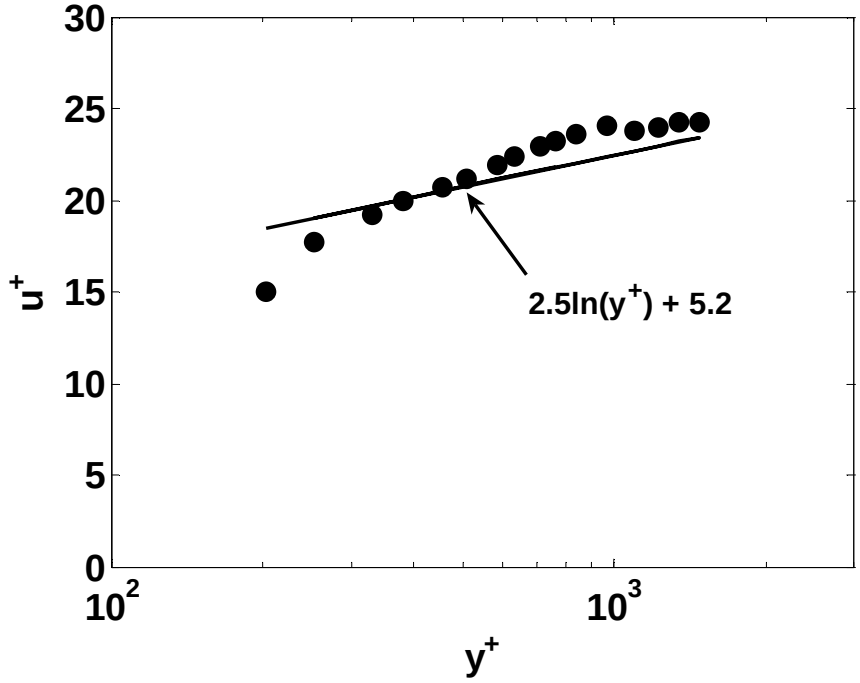

(b)

Figure 3.2: Boundary layer profiles (a) scaled on outer variables (b) scaled on inner variables

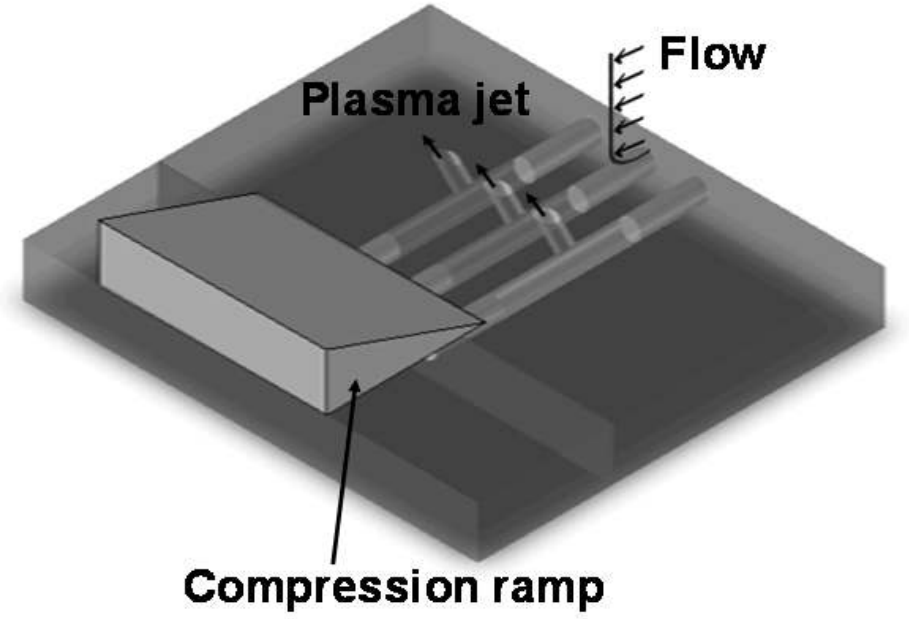

Figure 3.3: Schematic showing the pitched skewed injection

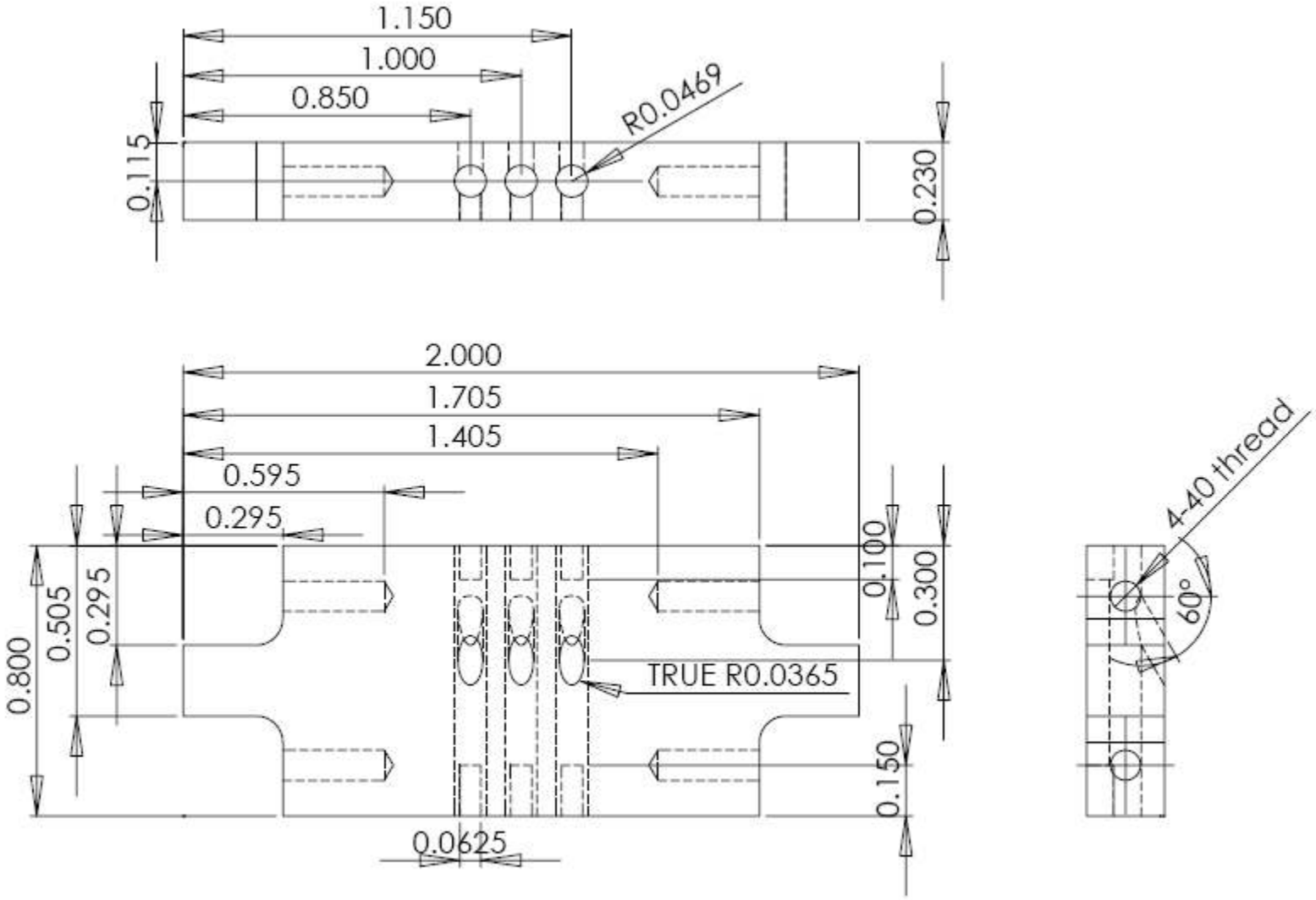

Figure 3.4: Illustration of mounting mechanism

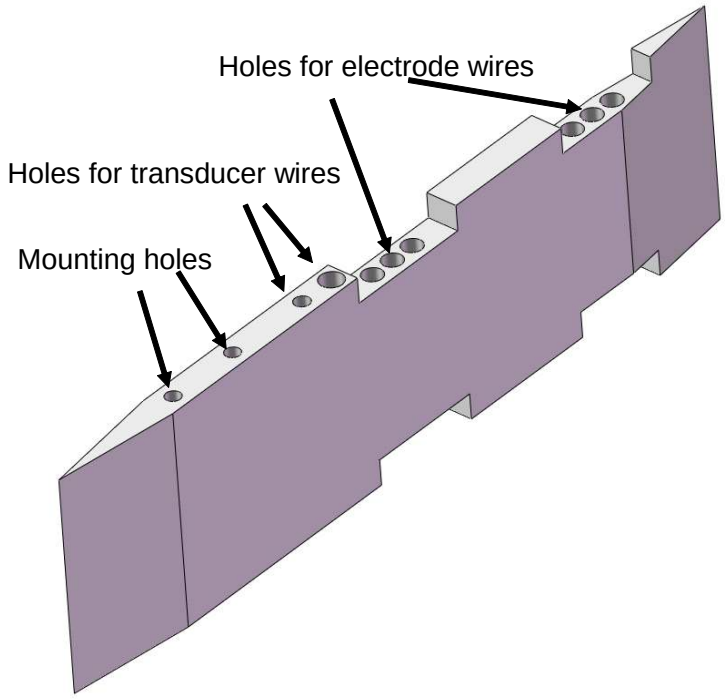

(a)

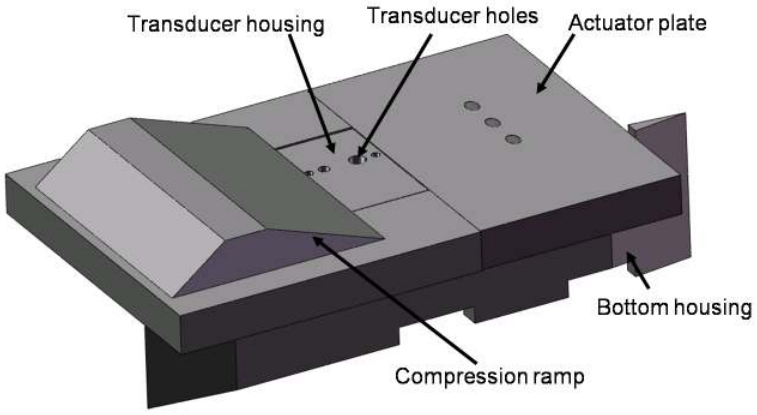

(b)

Figure 3.5: (a) Schematic of bottom housing and (b) assembly of the bottom housing with the actuator

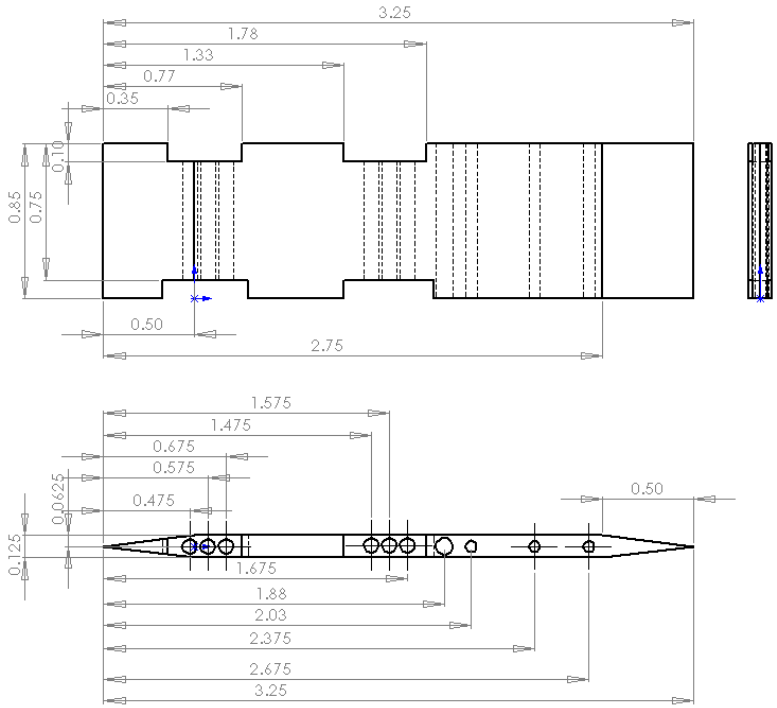

Figure 3.6: CAD drawing of the bottom housing

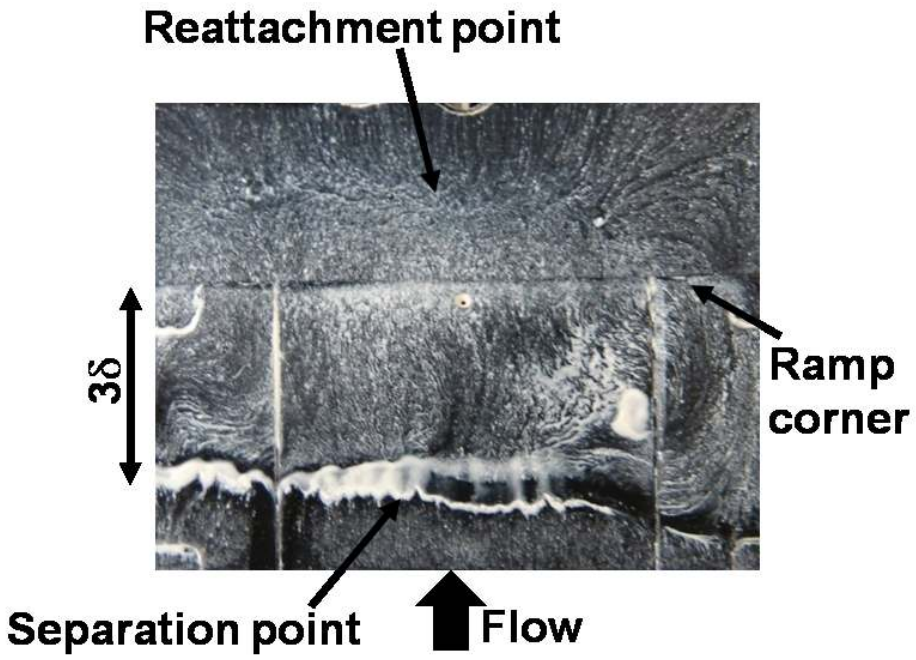

Figure 3.7: Surface streak visualization of the separation bubble caused by a 24° compression corner

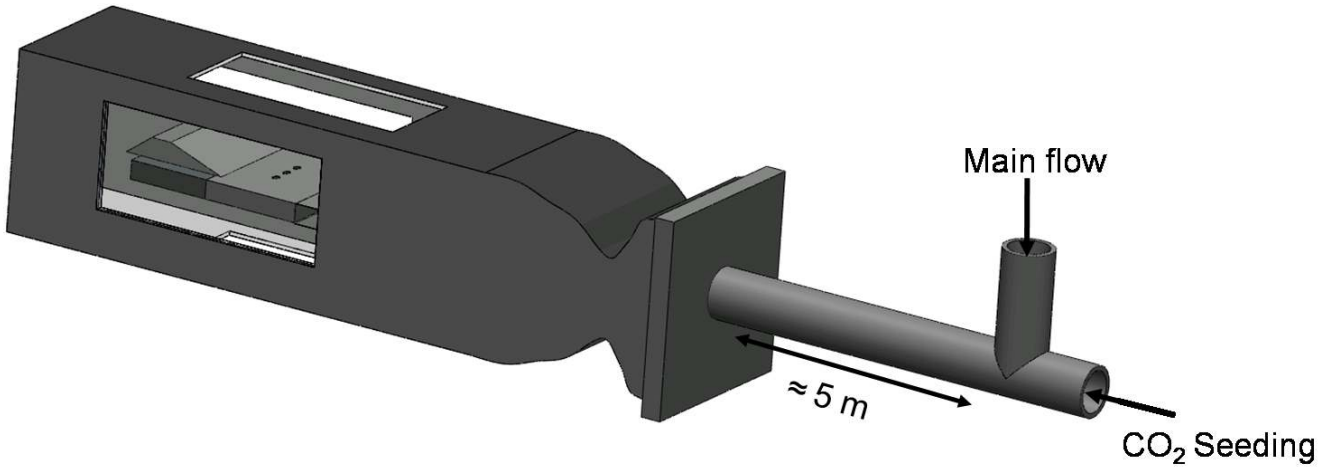

Figure 3.8: Schematic of PLS set up

Chapter 4

Characterization of the pulsed plasma jet

A detailed study was undertaken to characterize the pulsed plasma jet in terms of its discharge and fluid-dynamic properties. The discharge characteristics studied were the nature of the discharge, rotational temperature of the bulk gas and the degree of non-equilibrium. The degree of non-equilibrium has a direct bearing on the gas heating efficiency and hence on the strength of the pulsed plasma jet. An attempt was also made to estimate the duration of gas heating by the discharge in order to estimate the gas heating rate. Previous studies on blast waves show clear dependence of the precursor shock velocity and contact surface velocity on the energy deposition rate (e.g. Freeman, 1968; Director and Dabora, 1977; Milinazzo et al., 1979; Oved et al., 1979).

The fluid-dynamic property of interest is the momentum of the jet as this gives a direct indication of how effectively the jet will perturb the flow. However, no density measurement of the jet could be made, and so the jet exit velocity is used as the metric for the strength of the jet in this study. The jet exit velocity measured was the contact surface velocity when the jet just exits the orifice. All the tests were performed in a stagnant chamber whose pressure is set at about $45\,torr$. This pressure was very close to the static pressure of the Mach 3 tunnel in which the pulsed plasma jet actuator is employed for flow control studies. The discharge was pulsed at a frequency of 60 Hz unless stated otherwise.

4.1 Current-Voltage Characteristics

The potential difference across the anode and cathode *vs* the discharge current (current-voltage trace) gives a rough indication of the nature of the discharge. The current-voltage trace also gives a direct estimate of the amount of energy deposited. The anode voltage was measured using a high voltage probe with GHz bandwidth (Tektronics P6015A) and the discharge current was inferred from the voltage drop across a $1.2\,\Omega$ resistor placed downstream of the cathode. The measurement uncertainty of the high voltage probe quoted by the manufacturer is $\leq$ 3%. Typical time histories of anode voltage (cathode close to ground) and discharge current during a pulse are shown in fig 4.1. The pulsing frequency of the discharge was $60\,Hz$. Once the discharge was initiated, the anode voltage decreased from $2\,kV$ to about $0.8\,kV$ in less than $5\,\mu s$ and then decreased to about $600\,V$ after $20\,\mu s$. The discharge current reached the set point value ($\approx 1.1\,A$ in fig. 4.1) in about $5\,\mu s$. The discharge current density, based on the electrode cross-sectional area, is estimated to be about $105\,mA/cm^2$. Based on this current density we infer that the discharge is essentially a highly constricted arc with possibly a high degree of non-equilibrium associated with the large gradients due to the small discharge volume (Kothnur and Raja (2005)). From the V-I plot shown, the input power into the discharge is estimated to be about $1\,kW$ and the total energy input during the $20\,\mu s$ time period is about $20\,mJ$. The current-voltage trace was found to be the same for all the discharge currents tested in this study. It should be noted that only square-wave discharge pulses were used to ensure that the energy was deposited at the highest rate. The rate of deposition of energy depends on the slope of the discharge current, which is maximum for a square waveform. In addition, it was demonstrated that the maximum exit velocity of the jet does not depend on the pulse width, for pulse widths larger than $20\,\mu s$.

4.2 Flow structure around the plasma jet

The flow structure of the plasma jet was observed by using phase-locked schlieren imaging at various delay times from the start of the discharge trigger. Figure 4.2 shows the typical flow structure for a time delay of 30 μs. The plasma jet is seen to develop as a typical mushroom shaped structure. It can be seen that the plasma jet is relatively brighter in intensity compared to the ambient air. This indicates a low density, and hence, a high temperature jet. A spherically symmetric precursor shock produced by the impulsively started jet is also seen above the jet contact surface. The absence of a Mach disk within the jet indicates that the local Mach number of the jet is subsonic. To test the repeatability of the contact surface and precursor shock trajectories more than three runs were made at each discharge current and time delay. The standard deviation of the contact surface trajectory at different time delays estimated from phase locked imaging was found to be less than 10 % (see fig. 4.4) for a 1.2 A plasma jet.

4.3 Contact surface trajectory

A phase-averaged schlieren time sequence was generated by capturing approximately one hundred images at several delay times. For each time delay, the locations of the phase-averaged contact surface and precursor shock (with respect to the jet exit) were measured. The resulting trajectories of these flow features are shown in fig. 4.3. For this figure the peak discharge (set-point) current was 3.9 A. Figure 4.3 shows that the trajectory of the precursor shock is linear over the entire time period, which indicates its velocity is constant over the range of times considered. In contrast, the contact surface slows down with increasing distance from the orifice. Figure 4.4 shows a comparison of the contact surface trajectories at the two discharge set-point

currents of 1.2 A and 3.9 A. For the 1.2 A case, the contact surface first becomes visible 15 μs from the start of the discharge trigger, whereas for the 3.9 A case, it takes only 10 μs. In addition, the slopes of the trajectories indicate that the 1.2 A discharge generates a lower velocity jet as compared to the 3.9 A discharge. This is expected since a higher discharge current causes more rapid heating when compared to a lower discharge current. Hence, a higher rate of pressurization in the discharge cavity is obtained with higher discharge current. The short time delay between the discharge trigger and the appearance of the jet indicates that the jet responds very rapidly. However, the bandwidth of the actuator is determined by the startup transient as well as the time required to refill the cavity with gas. This will be discussed further below.

4.4 Jet velocity measurements

The contact surface velocity was measured from the slope of the contact surface trajectory close to the jet exit. It must be noted that the contact surface velocity is not necessarily the same as the local jet fluid velocity because the jet velocity can be influenced by trailing expansion waves. As a consequence, it is expected that the contact surface velocity is an upper limit to the local jet fluid velocity. With this caveat in mind, the following discussion will refer to the measured contact-surface velocity as the "jet velocity". A survey was made of the factors that influence the strength of the jet as quantified by the jet velocity close to the jet exit. One of the main factors that affect the jet velocity is the discharge current since it dictates the input energy. Figure 4.5 shows the variation of the jet velocity with discharge current. In all cases the separation between the electrodes was $0.5\,cm$ and the orifice diameter was $1.8\,mm$. The velocity increases from about $230\,m/s$ at $1.2\,A$ set-point current to

about $320\,m/s$ at $12\,A$. Thus there is just a $30\,\%$ increase in velocity for a 10-fold increase in discharge current. This issue will be discussed further in the next section. It was also found that the strength of the jet depends on the material of the cavity. For example, the jet velocity increased by about $30\,\%$ when boron-nitride, which has a higher thermal conductivity and corrosion resistance, was used instead of Macor™ ceramic. A possible explanation for this observation is given in section 4.5.

4.4.1 Variation with geometric parameters

A preliminary study of the effect of the geometric parameters on the exit velocity of the jet was also performed. The two parameters varied were the orifice diameter and the cavity volume. Orifice diameters were varied from $0.25\,mm$ to $1.8\,mm$. The jet exit velocity variation with respect to the orifice diameter is shown in fig. 4.6. It can be seen that the magnitude of the velocity is roughly the same for all the diameters tested. The effect of the cavity volume on the jet exit velocity was investigated for two volumes. The cavity volume was changed by changing the separation distance between the electrodes while leaving the cross sectional area of the cavity the same. A $1\,cm$ (0.4") separation distance corresponded to a cavity volume of $\approx\ 0.04\,cm^3$, whereas a $0.5\,cm$ (0.2") separation corresponded to a volume of $\approx\ 0.02\,cm^3$. The trajectories of the contact surface measured using phase locked schlieren imaging is shown in fig. 4.7. It is seen from fig. 4.7 that the trajectories of the jet for the two cavity volumes (0.04 and $0.02\,cm^3$) are approximately the same. It is also noted that the jet exit velocities are also very similar in both the cases. Thus it can be concluded that the jet exit velocities are relatively insensitive to the particular choice of the jet exit diameter and cavity volume used in the current study.

4.5 Effect of pulsing frequency on plasma jet performance

One of the important objectives of developing the pulsed plasma jet is that the pulsing frequency of the jet should be in the range of the separation bubble unsteadiness. When the pulsing frequency is in the range of unsteadiness there is a high possibility that one can lock the separation bubble oscillations to the pulsing frequency. In other words, the energy in the broadband frequency of the separation bubble unsteadiness would be transferred to the pulsing frequency. Hence pulsing frequency is a very important parameter of interest. From the synthetic jet generation perspective, the pulsing frequency essentially determines the cavity recharge time available between pulses. Figure 4.8 shows a train of discharge current pulses for two frequencies: $5\,kHz$ and $10\,kHz$. Figure 4.8(a) corresponds to $5\,kHz$ pulsing, whereas fig. 4.8 (b) and (c) correspond to two different experimental realizations at $10\,kHz$. At $5\,kHz$, a discharge pulse occurs reliably for every trigger signal. In addition, the discharge current remains unchanged during each pulse. In contrast, at $10\,kHz$ (figs. (b) and (c)) it is observed that the pulsing behavior is somewhat erratic where some pulses in the pulse train are occasionally missed. It can also be seen that occasionally the peak pulse current gradually decreases during a continuous pulse train until the pulse train completely pauses without any discharge activity for a few hundred microseconds before the pulse discharge activity resumes once again.

The erratic pulsing at higher frequency may be because of some inherent limitations in the electrical circuitry (such as the capacitance of the circuit, including the electrode gap), the high voltage power supply used, and/or due to the finite time for replenishment of the fluid in the cavity. Some experiments were conducted to test the limitations of the circuitry at high frequency. First the cathode and anode were replaced with a resistor that was equivalent to that of the discharge. In this

configuration, pulsing rates of over $100\,kHz$ were obtained reliably. Then a pulsed DC discharge circuit was made, except the electrodes were exposed to the ambient pressure ($35\,torr$) in a low pressure chamber rather than being enclosed in a cavity. This test takes into account the limitations inherent to the circuitry and also the capacitance of the electrode gap. The circuit was able to maintain repeatable pulsing to frequencies as high as $20\,kHz$ without loss of current. Moreover from fig. 4.1 it can be seen that the anode voltage recovers to its original value before the plasma was switched on ($\approx 2.1\,kV$) in less than $60\,\mu s$.

A study was also made of the role of the power supply on limiting the maximum possible pulsing frequency. Normally the power supply operates in two modes – "voltage-limited" mode and "current-limited" mode - depending on the operation settings. In the "voltage limited" mode, the operating settings are such that the power supply cannot supply the average set point current even at the maximum voltage that it can supply. In other words the voltage that the power supply can provide is smaller than what would be needed to sustain the average set point current. Figure 4.9 (a) shows the current voltage characteristics of the plasma discharge in voltage limited mode. The plasma is pulsed at $5\,kHz$ with $10\,\mu s$ pulse duration. The ballast resistor is set to draw a mean current of $100\,mA$. Note that the voltage before the start of the discharge pulse is about $2.1\,kV$, which is the maximum the power supply can provide. In the "current limited" mode, the maximum voltage that the power supply can provide is in excess of what is required to sustain the average set point current. In other words the current is "limited" from drawing the maximum voltage that the high voltage source can supply. Figure 4.9 (b) shows the current voltage characteristics of the plasma discharge in current limited mode. The plasma is pulsed at the same frequency and mean set point current as fig. 4.9 (a). However the ballast

resistor is set to draw much larger peak current than the peak current of the voltage limited mode. Note that in this case the maximum anode voltage before the start of the discharge is about $1.6\,kV$. Thus it is clear that in the current limited mode the maximum voltage that the power supply supplies could be substantially lower than its maximum rating.

Simultaneous current and voltage trace measurements were made using a high voltage probe for $5\,kHz$ and $10\,kHz$ pulsed plasma jets to investigate the role of the power supply in limiting the pulsing frequency. It should be noted that for both the frequencies the mean current was $200\,mA$ and the pulse duration in both cases was set at $20\,\mu s$. For a given mean current setting and pulse duration, the current required per pulse is higher for a $5\,kHz$ discharge compared to a $10\,kHz$ discharge. Thus while the power supply operates in voltage limited mode at $5\,kHz$ pulsing, it operates in current limited mode at $10\,kHz$ pulsing. Figure 4.10 (a) shows the voltage trace at $5\,kHz$ pulsing and fig 4.10 (b) shows the trace $10\,kHz$ pulsing. For a $5\,kHz$ pulsed plasma jet, it can be seen that the anode voltage before the start of the discharge trigger is about $2.1\,kV$ consistently. However, for a $10\,kHz$ pulsed-plasma jet, the anode voltage before the start of the discharge trigger is about $1.4\,kV$. This is because the power supply at $10\,kHz$ pulsing always operates in current-limited mode. It is possible that the maximum voltage supplied by the power supply is not high enough to generate the discharge pulse in the cavity that is recharging from the previous firing. These observations lead us to conclude that the pause of a few $100\,\mu s$ in the discharge activity is a consequence of the cavity replenishment timescale being longer than the inter-pulse period and a smaller maximum anode voltage the power supply can provide in the "current" mode at $10\,kHz$. Given that the pulsing occurs reliably up till $5\,kHz$, one can infer that the minimum replenishment time needed for

producing next reproducible pulse for a $1.2\,A$ pulsed plasma jet is about $200\,\mu s$.

It was also mentioned earlier that a boron nitride cavity resulted in a higher pulsed-plasma jet velocity than a Macor™ cavity. Boron nitride has higher thermal conductivity than Macor™. Therefore, it is likely that the boron nitride cavity remained cooler than the Macor™ cavity due to higher heat transfer to the surrounding material and this led to higher density inside the cavity during the start of each pulse. It is known that the higher gas density leads to less non-equilibrium and hence more gas heating.

4.6 Preliminary theoretical calculations of the jet exit velocity

From the velocity measurements presented in the previous section it is clear that the jet exit velocity is typically about $300\,m/s$ for the range of discharge currents tested. In particular it was also shown that the velocity increased from $250\,m/s$ to $330\,m/s$ ($about\,30\,\%$) for an increase in discharge current from $1.2\,A$ to $11\,A$ (about 9-fold). At this point it is instructive to obtain theoretical predictions of the jet exit velocity assuming an equilibrium discharge causing ideal constant volume gas heating. The assumption of equilibrium discharge means that all the input energy through electrothermal heating is totally converted into a corresponding rise in gas temperature. The jet exit velocity assuming a complete instantaneous conversion of input thermal energy to kinetic energy is given by

$$\frac{1}{2}mv^2 = mC_v\Delta T \quad = Q_{in} = \int V(t)I(t)dt$$

where m is the mass inside the cavity, ΔT is the rise in temperature due to gas heating and Q_{in} is the input heat due to electrothermal heating by the plasma discharge calculated by integrating the input power during the discharge duration. Hence the theoretical value of the maximum possible velocity is given by

$$v = \sqrt{\frac{2\int V(t)I(t)dt}{m}}$$

This velocity would give the upper bound of the jet exit velocity that could be obtained and would shed some light on the efficiency of gas heating. Table 4.1 gives the theoretical estimate of the maximum possible jet exit velocity for two values of discharge current. From the table it is clear that the jet exit velocity for 1.1 A pulsed plasma jet at 100 % efficiency is about 2850 m/s. This is about 10 times higher than the velocity measured (230 m/s). Thus the efficiency, defined at the ratio of measured velocity to the maximum possible velocity, of the 1.2 A plasma jet is about 9 %. For a 3.8 A pulsed plasma jet the maximum possible velocity is about 5100 m/s and the measured velocity is about 300 m/s. Hence the efficiency of the 3.8 A pulsed plasma jet is about 6 %. Thus it is clear that the pulsed plasma jet efficiency decreases with increase in discharge current.

The prime reason for the significant disparity in the measured and predicted jet exit velocity is the assumption of equilibrium heating of gases. Hence, in order to explain the observed jet exit velocity and to obtain further insight into the operation of pulsed plasma jet actuator, a detailed study of non-equilibrium effects in the discharge is made. The assumption of instantaneous heating is addressed subsequently.

Discharge Current (A)	Duration (μs)	Q_{in} (mJ)	v (m/s) (theoretical)	v (m/s) (measured)
1.1	20	12.6	2852	230
3.8	20	40.5	5088	300

Table 4.1: Theoretical predictions of maximum jet velocity

4.7 Non-equilibrium effects in the discharge

To obtain a detailed quantitative estimate of the degree of non-equilibrium, measurements of the N_2 rotational and vibrational temperature were made at different discharge currents, pulsing frequencies and pulse widths. The rovibronic emission spectrum of N_2 in the wavelength range from 365 to 395 nm was measured with a spectrograph. The N_2 second positive system ($C^3\Pi_u \rightarrow B^3\Pi_g$) with band heads at $380.49\,nm$ ($0-2$ vibrational transition), $375.54\,nm$ ($1-3$) and $371.05\,nm$ ($2-4$) was observed. The rotational temperature was found by fitting the observed rotational spectra with synthetic spectra corresponding to different rotational temperatures. The vibrational temperature was found by matching the band head intensities for different vibrational transitions. The procedure is described in detail in a previous work (Shin et al. (2007)) and in Appendix B. The fractional deviation between the measured spectrum and synthetic spectrum fit is estimated to be about $10-15\,\%$ (see appendix B). Figure 4.11 shows a typical spectrum obtained for a $6.5\,A$ discharge with $20\,\mu s$ duration. The rotational temperature is about $800\,K$ and vibrational temperature is about $3100\,K$. In comparison, for a $1.2\,A$ discharge the rotational temperature is about $600-700\,K$ and the vibrational temperature is about $2800\,K$. Thus the pulsed discharge is characterized by high degree of thermal and chemical non-equilibrium through the entire range of discharge currents employed in this work. Note that the measured temperatures are significantly lower than those reported in Utkin et al. (2007) for a non-enclosed pulsed arc at 1 atmosphere. They reported a rotational temperature of about $2000\,K$ for a $250\,mA$ discharge with $20\,\mu s$ pulse width. This temperature is considerably closer to the equilibrium temperature, which is not surprising considering the higher pressure of the discharge. The non-equilibrium distribution can be explained considering the different molecular collisional / relax-

ation processes involved in gas heating in an electric discharge. An illustration of the dominant energy pathways in the plasma is shown in fig. 4.12. The input energy in the electric field is transferred most efficiently to the plasma electron pool via electron Joule heating (energy in the electron being quantified by the electron temperature T_e). The imposed electric field also couples energy to the ion species via ion Joule heating (quantified by a distinct ion temperature T_i). The thermal energy of the ions is however quickly equilibrated with the other neutral heavy species in the discharge owing to efficient collisional transfer resulting in $T_i \approx T_g$, where T_g is a common heavy species (gas) temperature. The electron energy (and hence the electron temperature T_e) remains relatively decoupled from the heavy species (ions and neutrals) thermal energy (i.e., $T_e > T_g$) owing to the large disparity in particle mass between electrons and other species. The high kinetic energy of the electrons is lost via electron elastic collisions with the heavy species (an inefficient process as mentioned above) and electron inelastic collisions (vibrational and electronic excitation) with heavy species. In a molecular gas (such as air), inelastic vibrational excitation of N_2 and O_2 molecules is particularly efficient and can be the dominant pathway for electron energy loss. The vibrationally excited gas molecules can transfer their energy to thermal energy (causing gas heating) via Vibrational-Translational relaxation, which has a characteristic timescale of milliseconds for vibrationally excited N_2 and O_2 under the conditions of the discharge in this study (Raizer (1991) and Vincenti and Kruger (2002)). Since the pulse width of the discharge is about 20 μs, the gas heating due to V-T relaxation during this time period is negligible, resulting in a decoupling of the vibrational energy of molecules from the thermal energy. In summary a large part of the input electrical energy in the discharge can be trapped in the electron thermal energy and the molecular vibrational energies, which is detrimental to the operation of the pulsed plasma discharge for flow actuation

purposes. The following estimates can be made for the conditions of the discharge in this study. From the discharge-current density ($45\,A/cm^2$) and electric field of $400\,V/cm$ (assuming a linear drop of electric potential between cathode and anode), the ion and electron (assuming a quasi-neutral discharge) number densities are estimated to be about $10^{13}\,cm^{-3}$ and the electron temperature (T_e) is estimated to be about 1.2 eV. This estimate was made by solving for the electron number density by using Ohm's law with known current density and electric field. The unknown electron number density is implicit in the electric conductivity. The empirical relations and experimental data given in Raizer (1991) were used. The estimated electron number density is several orders of magnitude smaller than the neutral number density ($10^{18}\,cm^{-3}$). For the computed values of ion and electron number densities, and the applied electric field, the fraction of input electric energy that goes into ion Joule heating is computed to be about 0.06 %. It is thus evident that the contribution from ion-neutral collisions towards gas heating is negligible. Hence almost the entire input electrical energy is used for electron Joule heating. The partition of electron Joule heating into rotational and vibrational modes of neutrals can be estimated by comparing the cross-sections for rotational and vibrational energy transfer. The cross sections of N_2 alone are considered for this analysis, which is justified since N_2 is the dominant species of the air plasma employed in this study. The numerical values of cross-sections are obtained from Engelhardt et al. (1964); Frost and Phelps (1962); Pitchford et al. (1981) and Pitchford and Phelps (1982). For a pressure of $35\,torr$, the reduced electric field (E/N) is about $16\,Td$. It must be mentioned that the cross section values do not change significantly for the reduced electric field in the range of 1 to $200\,Td$ and hence the error introduced by an inaccurate estimation of the electric field is quite small. From the theoretical computations based on cross-section performed for N_2 at $77\,K$ in Engelhardt et al. (1964), it is seen that about 90 % of

the input power goes into excitation of vibrational modes whereas less than 10 % goes into rotational modes. Thus almost the entire input energy is locked up in vibrational modes whose relaxation time scale is orders of magnitude larger than the discharge time scale, and hence the vibrational temperature is expected to be much higher than the rotational temperature. However, at high pressure ($\mathcal{O}$ ($1\,atm$)) and for the same value of electric field, the reduced electric field would be about 50 times smaller. For such small values of reduced electric field, the fraction of input energy that goes into gas heating increases rapidly to about 90 % (as estimated in Engelhardt et al. (1964)), which is close to the value observed in Utkin et al. (2007). A direct measurement of the fraction of input energy that goes into gas heating is performed in Culick et al. (1976) and Smy et al. (1983). Gas heating of pulsed N_2 plasma at $300\,K$ and at different E/N values was studied both theoretically and experimentally in Culick et al. (1976). Based on these results, it is estimated that only about 10 % of input energy goes towards gas heating, whereas 90 % goes into vibrational excitation. Similar heating efficiency is also reported by Smy et al. (1983) who used a plasma jet facility with input energy of about 1 J at 0.1 atm pressure. Assuming that 10 % of the input energy goes into gas heating as estimated from cross-sections and heating efficiency given in Engelhardt et al. (1964), the gas temperature for a $1.2\,A$, $20\,\mu s$ pulse width discharge is calculated to be about $600\,K$ (compared to the measured value of $600 - 700\,K$), and that for $6.5\,A$ discharge is about $1500\,K$ (compared to the measured value of about 800 - 1000 K see fig. 4.11 and 4.13). Thus the calculated values of temperature are within a factor of 2 of the measured temperature.

A revised theoretical estimate of the jet velocity can now be obtained by a shock-tube problem analysis. This analysis was successfully employed in Smy et al. (1982) to obtain the exit velocity from a plasma igniter. Considering the rapidity

of the heating by electric discharge in the present application, we expect that the shock-tube analysis should yield a reasonable estimate of the jet exit velocity for the pulsed plasma jet also. We adopt the nomenclature used in Anderson (2002) for our analysis. The instantaneous energy deposition by the electric discharge (analogous to the rupture of diaphragm in a shock-tube) creates a precursor shock that propagates into the ambient and a train of rarefaction waves that travel into the cavity (analogous to the driver section). The passage of rarefaction waves causes a decrease in pressure of the gas. Hence there is a smooth decrease of pressure from its initial high value (defined here as P_4) at the head of the rarefaction wave to the station just behind the precursor shock (p_3). The latter can be calculated from the normal shock relations with the knowledge of the precursor shock propagation velocity obtained from the shock trajectory in fig. 4.3. The initial high pressure p_4 is the cavity pressure at the end of energy deposition. Its value can be calculated from the ratio of gas temperature (T_g) obtained using spectroscopic measurements and ambient temperature, assuming constant volume heating. The exit velocity of the jet is assumed to be the same as the velocity of the downstream edge of the precursor shock. This assumption is reasonable because close to the jet exit, the precursor shock and the contact surface are close to each other. The exit velocity is thus calculated using the relation

$$v_3 \;=\; a_4 \times \frac{2}{\gamma - 1} \times \left(1 - (\frac{p_3}{p_4})^{\frac{\gamma-1}{\gamma}}\right) \tag{4.1}$$

where a_4 is the speed of sound in the cavity (driver section) after energy deposition. For $T_g = 700\,K$ (as the case of $1.2\,A$ pulsed plasma jet), the jet velocity is estimated from Eq.4.1 to be about $370\,m/s$. Furthermore, for $T_g = 800\,K$ (fig. 4.11), which was measured at a current of $6.5\,A$, Eq. 4.1 yields a jet velocity of about $400\,m/s$. However, the jet velocity obtained is about $230\,m/s$ for $1.2\,A$ pulsed plasma jet and

$300\,m/s$ for a $6.5\,A$ pulsed plasma jet. Though the theoretical velocities computed using the instantaneous heating model are of the same order of magnitude as the measured values, there is still a disparity of about 60 %.

4.7.1 Effect of finite duration of gas heating

The disparity between the predicted and measured velocities is perhaps explained as a limitation of the instantaneous heating assumption. To explore this possibility an attempt was made to measure the temporal evolution of the discharge temperature during the discharge pulse. Since it was not possible to make gated measurements using the spectrometer, an indirect estimate of the temporal evolution of the discharge temperature was made. As the intent was to demonstrate the gradual heating by the electric discharge, this approximate method was found to be adequate. It should be noted that no quantitative conclusions from this measurement are made. Discharge temperature was measured for a $6.5\,A$ pulsed discharge with different pulse widths, viz., $10\ \mu s$, $15\,\mu s$, and $20\,\mu s$. The temperature measured at a given pulse width is assumed to be a representative average of the temperature of the discharge during the discharge pulse. In other words, the temperature measurement of a $10\,\mu s$ pulse width discharge would correspond to an average discharge temperature between 0 and $10\,\mu s$. Similarly a $15\,\mu s$ pulse width discharge would correspond to an average gas temperature between 0 and $15\,\mu s$ and so on. In addition, the temperature of the discharge at an instant within a given pulse width does not depend on the evolution of the discharge after that instant. That is to say, the temperature at the end of say $10\,\mu s$ in a $20\,\mu s$ discharge does not depend on the discharge temperature at time later than $10\,\mu s$. Thus the temperature at the end of $10\,\mu s$ depends only on the discharge evolution between $0 - 10\,\mu s$ and is independent of the discharge evolution at later

times ($t > 10\,\mu s$). By this reasoning, the gas temperature measurement at different discharge pulse widths would, in effect, give a pseudo time series of the temperature of the discharge during the evolution of the pulsed-plasma jet. Figure 4.13 shows the pseudo temporal evolution of the gas temperature of a $6.5\,A$ pulsed discharge. The representative discharge temperature between 0 and 10 μs is plotted at 10 μs and the representative discharge temperature between 0 and $15\,\mu s$ is plotted at $15\,\mu s$, and so on. It is clearly seen that the gas heating is not instantaneous and the time scale of gas heating is about $10\,\mu s$. This suggests a gradual heating of the cavity and hence may explain why the theoretical velocity estimate, which assumes instantaneous gas heating, over-predicted the jet velocity.

Finally, the efficiency of the pulsed plasma jet is defined as the ratio of the total kinetic energy (KE) issued from the cavity over a cycle to the input energy. The total kinetic energy is defined as

$$KE = \int_0^\tau \frac{1}{2}\dot{m}u_j^2 dt$$

where $\dot{m}$ is the jet mass flow rate and τ is the time-period of the discharge. A typical case of $6.5\,A$ peak discharge current is considered for this analysis. The rotational temperature measured from spectroscopy for this case is about $800\,K$, which is taken as the gas temperature. By using this temperature and assuming constant ratio of specific heats, the thermal energy deposited per cycle was estimated to be $1.2\,mJ$. A first-order model of the process was developed in Cybyk et al. (2003) and this was used to estimate the mass expelled from the cavity. The model predicts that 20 % of the mass in the cavity is expelled during each cycle, and we further assume that this mass is expelled at a uniform rate. Combining these values with the previously described velocity measurements, the efficiency of the pulsed plasma jet actuator is

about 4 %. We note that a systematic study of the effect of gas temperature on the discharge current was not made, and so the dependence of the efficiency on the input power is not yet known.

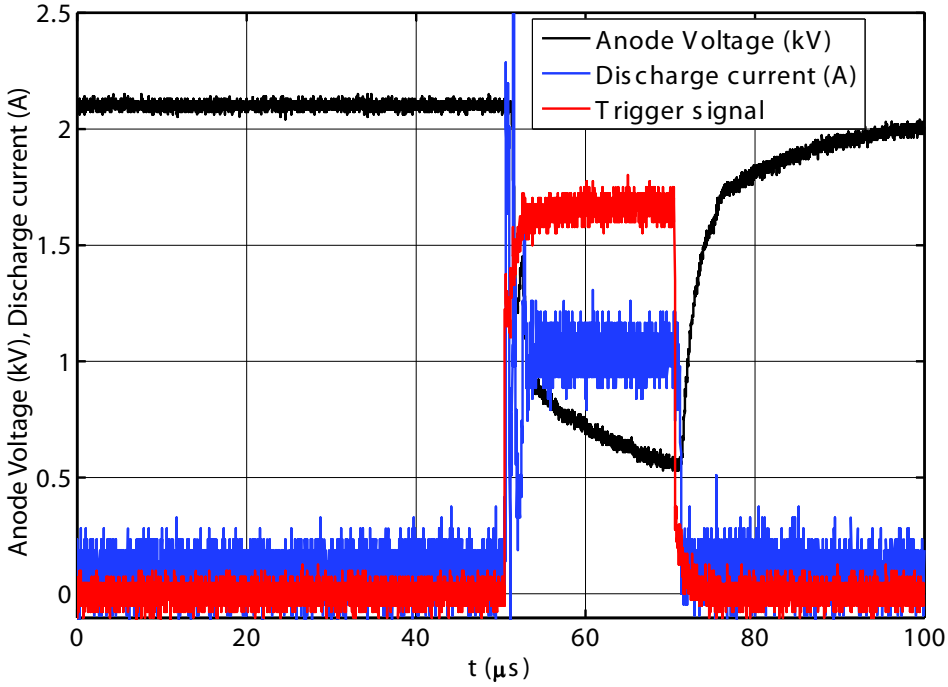

Figure 4.1: Typical current-voltage characteristic of one pulse of the pulsed plasma discharge. The pulsing frequency of the discharge was 60 Hz.

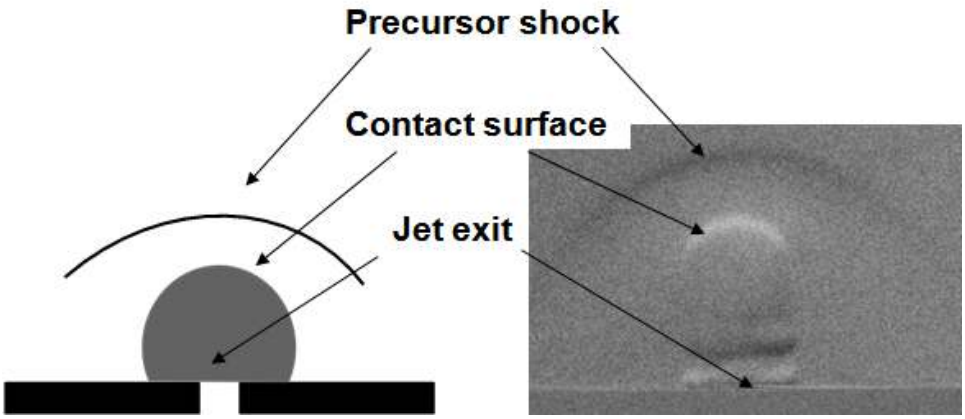

Figure 4.2: Flow structure of one of the jet pulses. The pulsed plasma discharge set-point current is 3.9 A. The image shown is taken 30 μs after the start of discharge trigger.

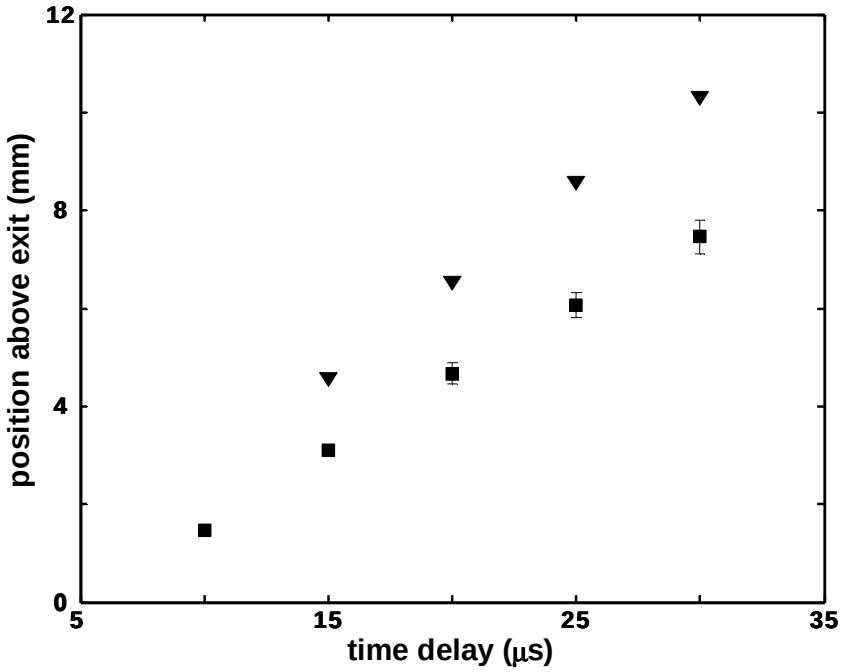

Figure 4.3: Trajectory of the pulsed plasma jet precursor shock (downward triangles) and contact surface (squares) for a discharge set-point current of 3.9 A. Time delays are measured from the start of the discharge trigger. The position of the contact surface is measured from the jet exit.

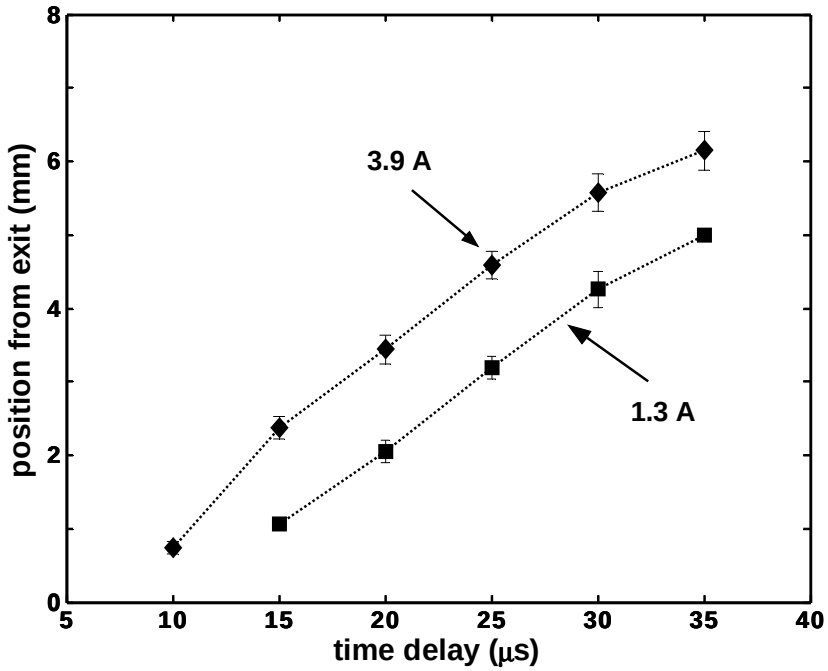

Figure 4.4: Comparison of trajectories of the contact surface of the pulsed plasma jet for two discharge set-point currents of 1.2 A and 3.9 A. Time is measured from the start of the discharge trigger. The position of the contact surface is measured from the jet exit.

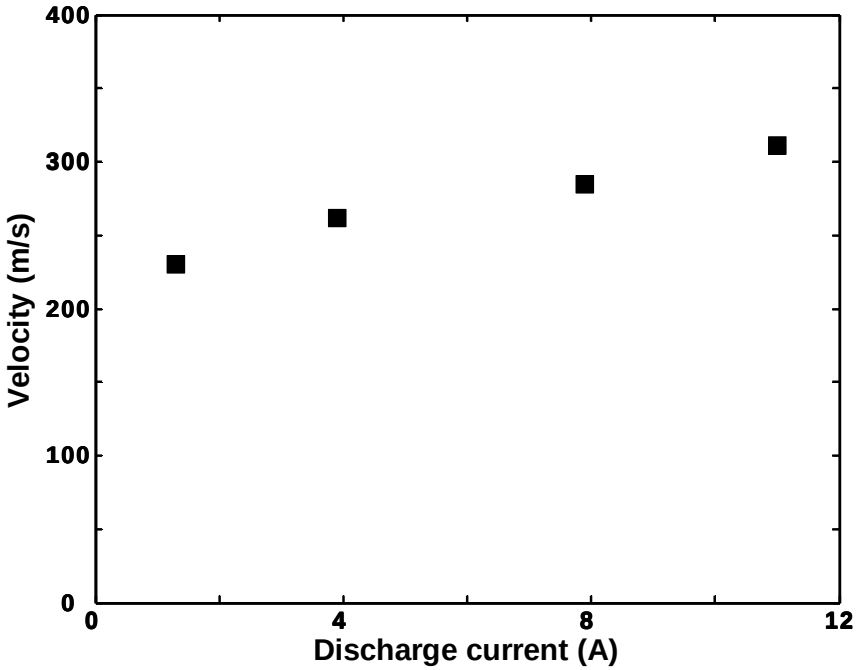

Figure 4.5: Variation of the plasma jet velocity with increasing discharge set-point currents.

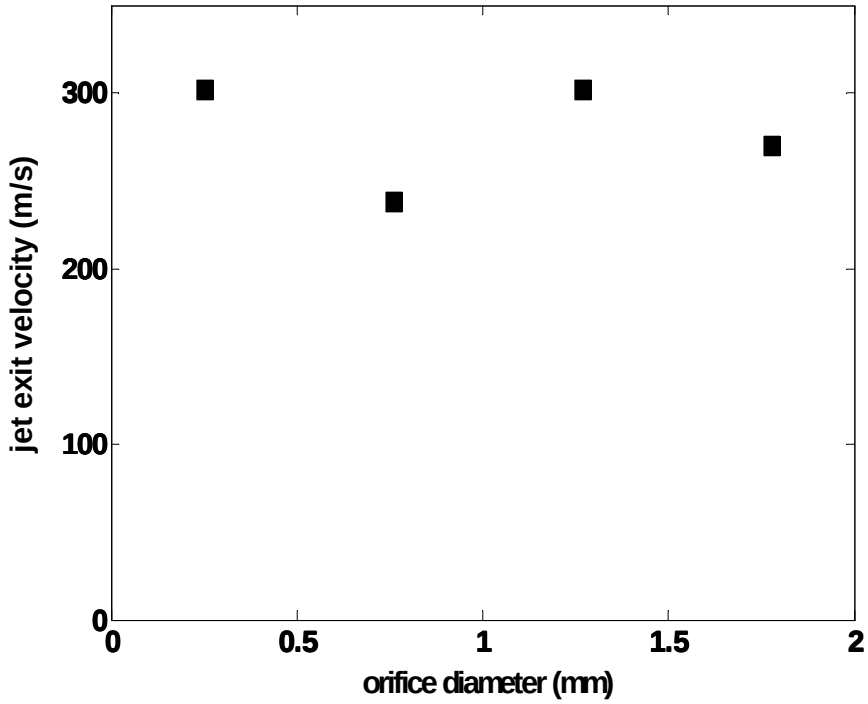

Figure 4.6: Variation of jet exit velocity of the pulsed plasma jet with respect to different orifice diameter. The discharge current is set at 3.9 A.

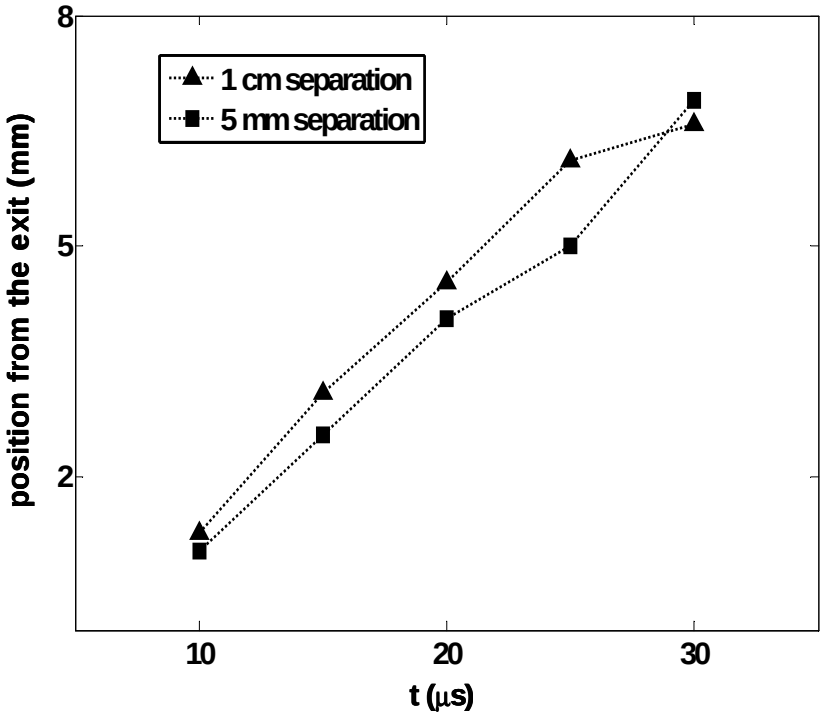

Figure 4.7: Variation of jet exit velocity of the pulsed plasma jet with respect to different cavity volumes. The 1 cm separation corresponds to a volume of 0.04 cm^3 and 5 mm separation corresponds to a volume of 0.02 cm^3 The discharge current is set at 3.9 A.

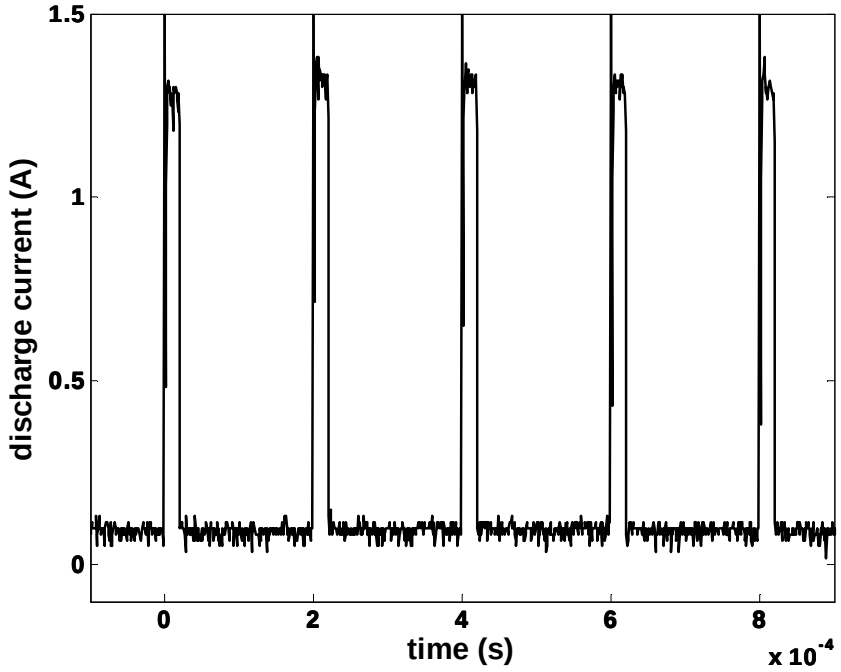

(a)

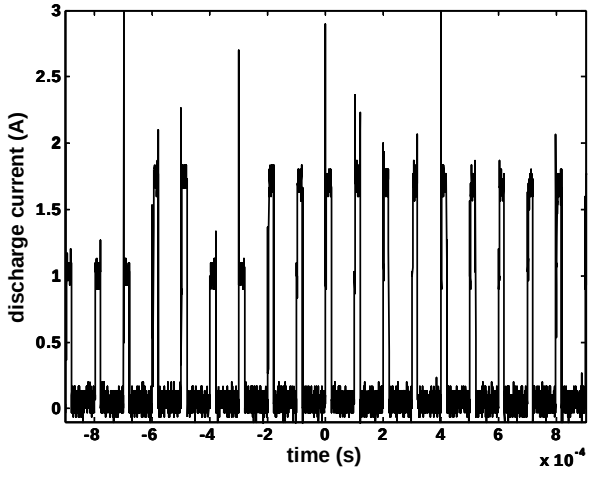

(b)

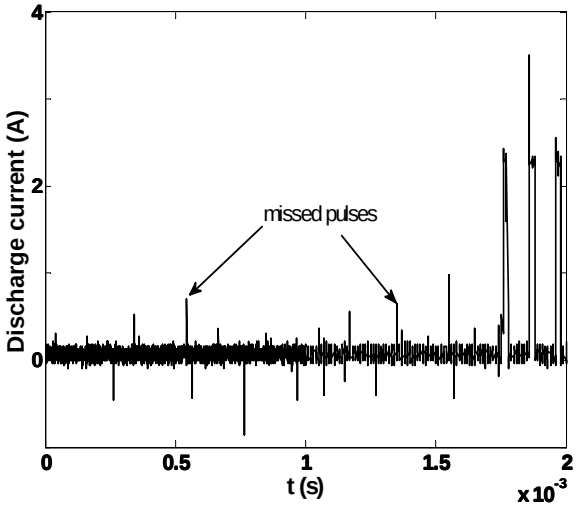

(c)

Figure 4.8: Discharge current pulse transients at different pulsing frequencies for a 1.2 A discharge set-point current. Figure (a) corresponds to a pulsing frequency of 5 kHz and (b) corresponds to 10 kHz.

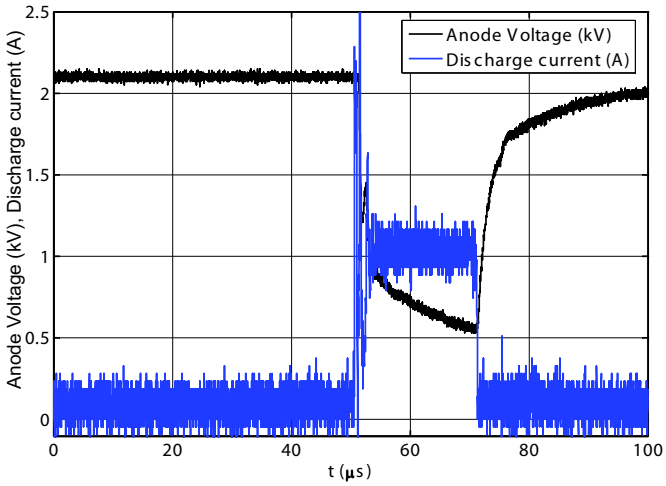

(a)

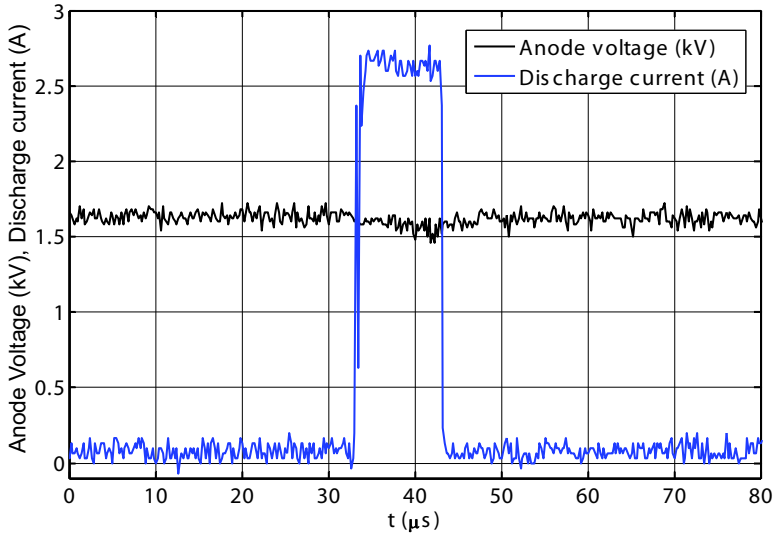

(b)

Figure 4.9: Illustration of operating modes of the power supply: (a) voltage mode and (b) current mode. The mean current was set at 100 mA and the pulsing frequency was set at 5 kHz for both the modes.

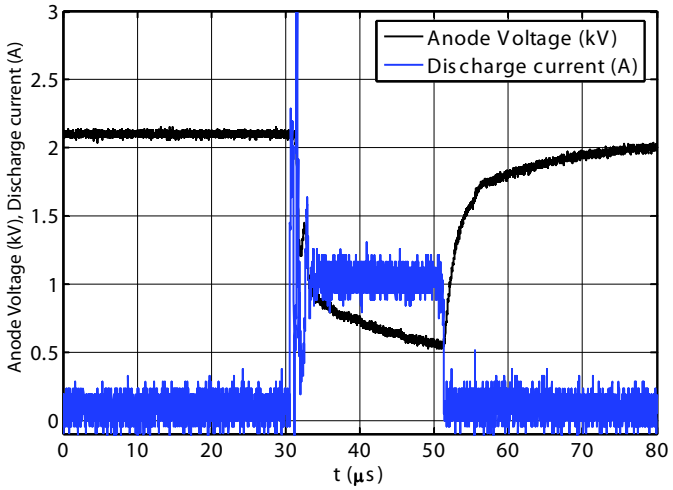

(a)

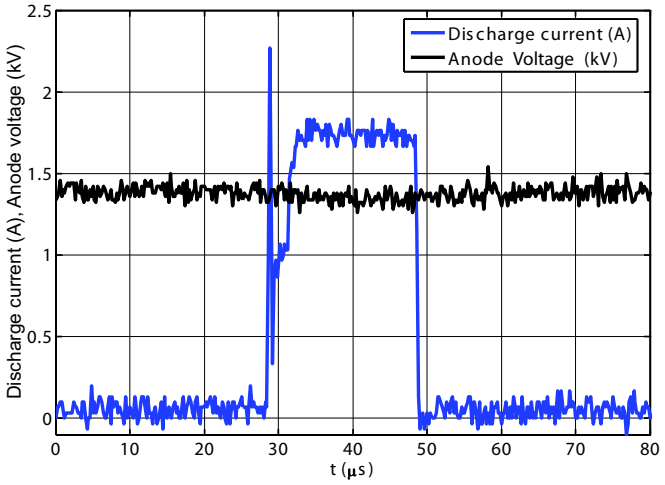

(b)

Figure 4.10: Discharge current and voltage characteristics of pulsed plasma jets at different pulsing frequencies (a) 5 kHz, (b) 10 kHz. The mean current was set at 200 mA and pulse duration was set at 20 μs for both pulsing frequencies

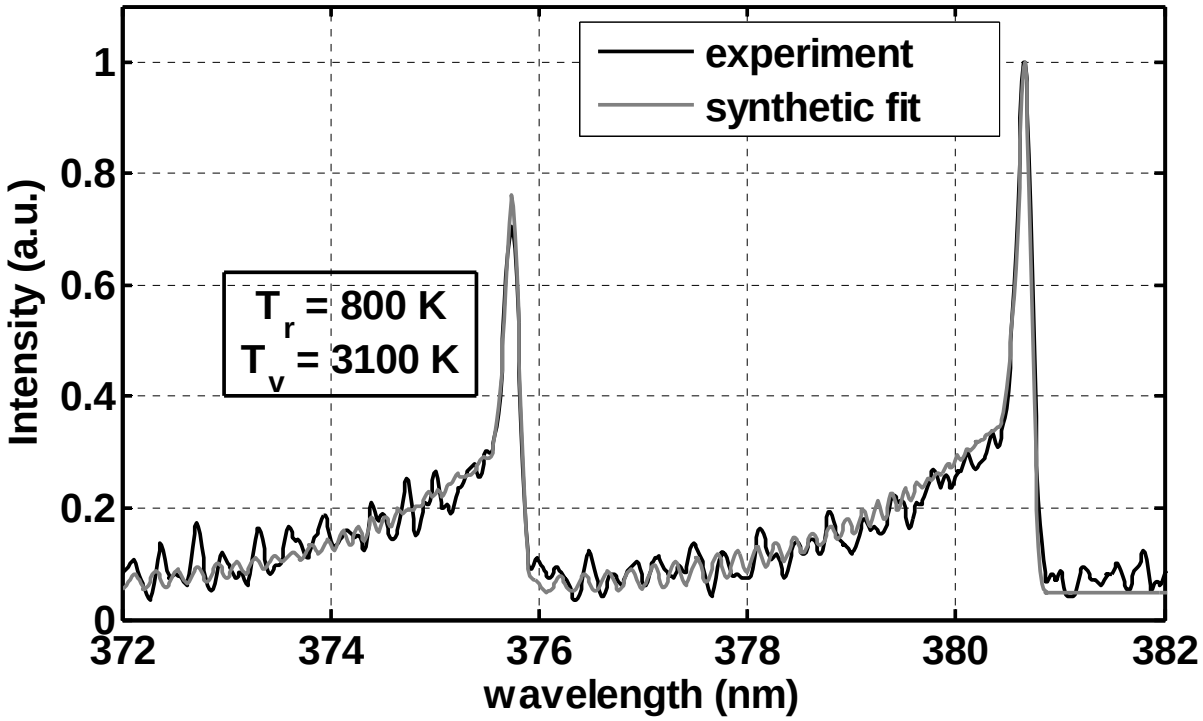

Figure 4.11: Measured (black curve) and synthetic fit (gray curve) of the optical emission spectrum obtained from the 6.5 A pulsed plasma discharge. The rotational temperature (T_r) for the best fit is 800 K and the vibrational temperature (T_v) is 3100 K. The uncertainty in temperature estimate is about 10-15 %.

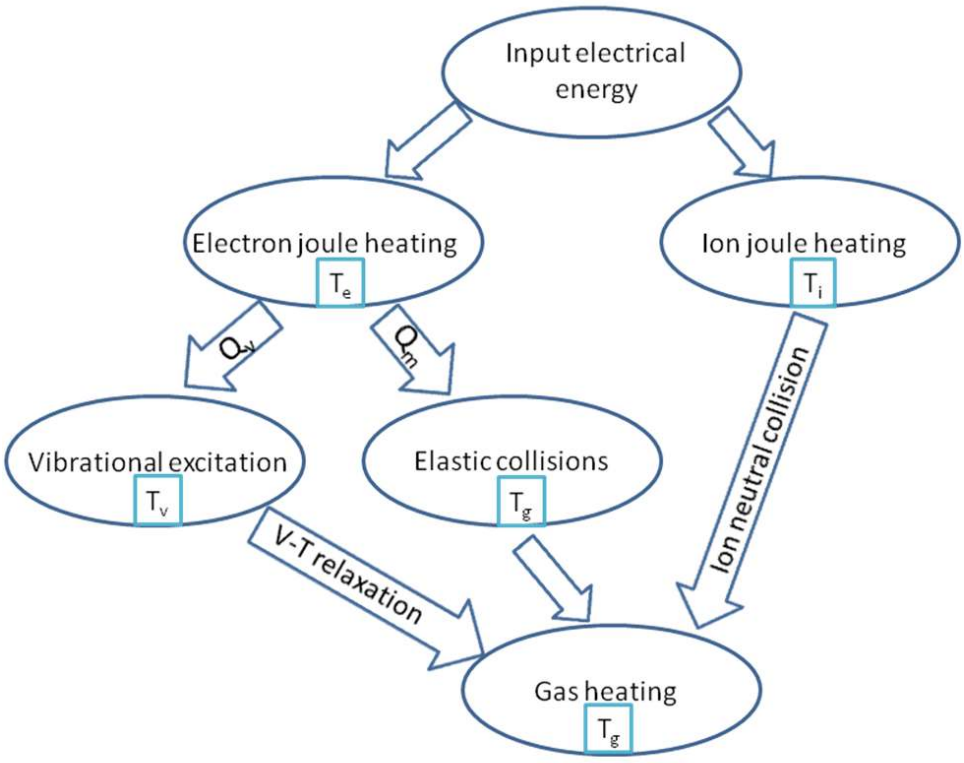

Figure 4.12: Illustration of the important energy transfer pathways that contribute to gas heating the pulsed discharge.

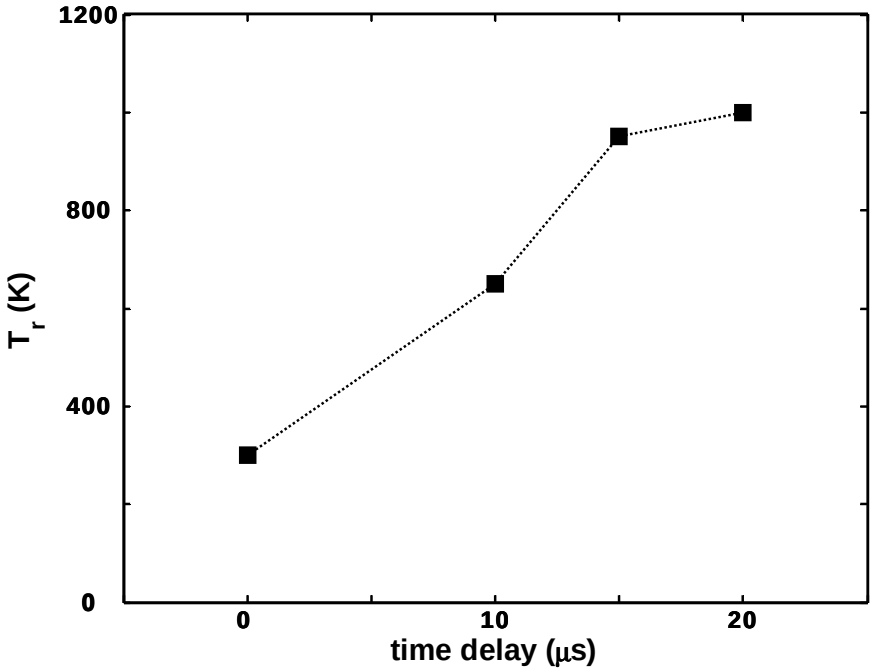

Figure 4.13: Rotational temperature obtained for 6.5 A pulsed plasma jet with different pulse width. Pulse width of 0 μs corresponds to the ambient temperature (no plasma). The variation of the rotational temperature with pulse width is an indication of the time evolution of the rotational temperature of the discharge.

Chapter 5

Interaction between the pulsed plasma jet and the separation shock: Mean flow structure

The mean characteristics of the interaction between the pulsed plasma jet with the separation shock are described in this chapter. The flow diagnostics performed includes schlieren imaging at 60 Hz and planar laser scattering (PLS) at 10 Hz. The details of the experiments were explained in chapter 3. The shock wave boundary layer interaction for this study was generated by a 30° compression corner whose span was 25 mm (1 inch), which spans half of the test section and no fences were used. The separation shock foot was located at about 2δ upstream of the compression corner.

5.1 Assessment of the strength of the pulsed-plasma jet

Initial tests were performed in order to assess the strength of the pulsed-plasma jet. As there were no direct means of measuring the momentum of the pulsed-plasma jet, the strength of the plasma jet was assessed indirectly by studying the penetration of the plasma jet injected normally into the incoming supersonic flow. Toward this, phase-locked schlieren imaging at 60 Hz at different time delays from the start of the discharge trigger was performed. The discharge was also pulsed at 60 Hz. At least 50 images were averaged at each time delay to obtain the phase averaged image corresponding to the time delay. The discharge current of the pulsed plasma jet tested was 1.2 A and a single jet was injected into the flow. The flowfield without pulsed jet

injection is shown in fig. 5.1 (a). The Mach waves, seen as bright and dark lines criss-crossing the image, are due to the imperfections in the ceiling and floor of the test section and they do not seem to affect the flow itself. In addition, it should be noted that the plasma-jet hole itself does not create any noticeable passive shock which would affect the flow. The flowfield around the pulsed plasma jet, during an injection event, is shown in fig 5.1(b). The jet is injected normal to the Mach 3 crossflow. The image was taken 35 μs after the start of the discharge trigger, which was the time of the maximum penetration observed in the schlieren imaging. The injection port is located roughly in the middle of the frame as indicated. The shock (marked shock due to pulsed plasma jet) upstream of the jet marks very closely the upstream boundary of the jet. The jet itself is seen as a relatively bright patch in the figure. The relatively brighter appearance of the jet indicates that it is hot compared to the surrounding fluid. The penetration of the jet was measured "by eye" by estimating the distance of the approximate jet centerline at its maximum penetration from the floor as shown in fig. 5.1 (b). From figure 5.1(b) the penetration of the jet is approximately 1.5δ (three orifice diameters). From the previous studies on penetration of steady jets in crossflow and accounting for the previous observation that pulsing increases the penetration by 12% (Murugappan et al. (2005)), the momentum ratio of the pulsed plasma jet compared to the free stream is estimated to be about 0.6. Similar imaging done with a 45° pitched and 90° skewed jet, which is the configuration that was extensively studied for flow control purposes, showed that its penetration was about 0.6 δ into the boundary layer.

5.2 Interaction of the jet with surrounding flow

Once the jet is injected into the incoming flow, it begins to interact with the surrounding flow. While it interacts with the surrounding flow, the jet may undergo changes in its structure and/or may induce some changes in the surrounding flow. In order to study this interaction, planview PLS images were taken at two wall normal locations, $\frac{y}{\delta} = 0.2$ and 0.5, and at different times. The interaction of the pulsed-plasma jet with the surrounding flow was studied in the context of the cross stream (z direction) force exerted by the plasma jet on the surrounding flow. It is known from previous studies that cross stream momentum addition is an important requirement for vortex generator jets to create streamwise vorticity. A single 45° pitched and 90° skewed plasma jet was employed because the pitched-skewed jets are known to cause maximum streamwise vorticity. Moreover, this particular configuration was chosen for the majority of the results presented in this work because the jet is confined within the boundary layer, which is desirable for effecting changes inside the boundary layer.

Figure 5.2 shows a phase-average PLS image taken with pulsed-plasma jet. The discharge current of the individual pulsed-plasma jet was 4.5 A. About 100 images were used to compute the average. In the figure, the lowest intensity corresponds to blue color, whereas the highest intensity corresponds to red color. Figure 5.2 was taken at 35 μs from the start of the discharge trigger. The direction of the pulsed-plasma jet injection is also marked in the figure. The jet orifice has the highest intensity because of the plasma luminosity and it has nothing to do with the PLS signals. The pulsed-plasma jet itself is rendered as a dark patch (shown as blue color in the figure) due to its high temperature, which causes the sublimation of the seeded solid CO_2 fog. The flow in the region other than the plasma jet is brighter due to the light scattered by the solid CO_2 fog seeded in the flow. The intensity in

the portion of the image that is opposite to the jet injection direction ($\frac{x}{\delta} < 1.5$) is very similar to that in the region upstream of the pulsed-plasma jet orifice, which is not affected by the plasma jet. This implies that the CO_2 fog in the opposite direction of the jet injection ($\frac{x}{\delta} < 1.5$) is undisturbed by the presence of the jets. However a relatively bright patch (seen as red color) can be observed adjacent to the jet boundary in the direction of injection (i.e. $\frac{x}{\delta} > 2$). This bright patch is marked in the figure. The bright region indicates an increased concentration of CO_2 along the border of the pulsed-plasma jet. This increased CO_2 concentration is caused by the cross-stream momentum addition by the pulsed-plasma jet. It has been shown in several previous studies involving pitched and skewed jets that the cross-stream momentum addition is the cause of generation of streamwise vorticity by the vortex generator jets (e.g., Johnston and Nishi (1990)). Thus, from the observation that the pulsed-plasma jet generates considerable cross stream penetration, it is expected that these pulsed-plasma jets could act as vortex-generator jets. The vortex-generator action of the pulsed-plasma jet is explored in detail in subsequent sections. It should be mentioned that the cross-stream penetration of the pulsed-plasma jet takes place only for a duration of about $20\mu s$. After about 20 μs, the pulsed-plasma jet is merely convected in the streamwise direction by the incoming flow.

The streamwise position of leading edge of the pulsed-plasma jet from the jet orifice was measured from the phase-averaged schlieren images taken at different time delays from the start of the discharge trigger. The measured leading edge trajectories are plotted in figure 5.3. The figure shows the trajectory of the leading edge measured at two different wall normal locations in the boundary layer: $\frac{y}{\delta}$ =0.2 and 0.5. The discharge current was set at 3.9 A for both the cases. It can be seen that the distance traveled by the pulsed-plasma jet varies roughly linearly with time. This shows that

the velocity of convection of the pulsed-plasma jets is roughly constant. The velocities were computed by fitting a linear curve to the trajectories obtained at different time delays. The velocities were thus estimated to be about 450 and 580 m/s at 0.2 and 0.5δ respectively. These values are very similar to the local velocity of the undisturbed flow at the corresponding locations seen from the boundary layer profile shown (480 m/s at $\frac{y}{\delta} = 0.2$ and 570 m/s at $\frac{y}{\delta} = 0.5$) in the previous chapter. In addition to the leading edge trajectory, the trajectory of the trailing edge of the pulsed plasma jet was also calculated. It was found (figure not shown) that the trajectories of the leading and trailing edge were parallel to each other. This means that there is no stretching or compression of the pulsed-plasma jet as it convects with the flow. The above results indicate that the pulsed-plasma jet is merely convected with the flow at the local velocity corresponding to its location, without undergoing any changes in its structure. Overall, the interaction of the pulsed plasma jet with the surrounding flow is characterized by initial cross stream momentum addition by the pulsed-plasma jet on the surrounding flow and subsequent streamwise convection of the jet fluid.

5.3 Characterization of the pulsed plasma jet interaction with separation shock wave

5.3.1 Pulsed plasma jet as a low momentum disturbance

As a first test of the effectiveness of the plasma jets for separation shock control, the plasma jets were tested to modify the separation shock generated by a 30° compression corner placed in a Mach 3 flow. An array of 3 pulsed-plasma jets was injected normally from approximately 5 δ ($\delta \approx 4.5$ mm) upstream of the compression ramp. This injection location is 3δ upstream of the separation shock foot location. The discharge current of an individual pulsed-plasma jet was set at 4.5 A.

Figure 5.4 (a) shows an instantaneous schlieren image without the injection. Several compression waves emanate from the intermittent region (locations at 2δ upstream of the compression corner) to form a single shock structure at an elevated location. Since the compression waves are very weak to be able to be captured in the schlieren images, they are not visible in the images. Fig. 5.4(b) shows an instantaneous phase-locked schlieren image at a time delay of 40 μs from the start of the discharge trigger. It can be clearly seen that the entire separation shock is 'bulged out' due to the passage of the plasma jet. In fact, the shock foot moves about 1 δ upstream as the plasma jet propagates into the interaction. The predominant upstream motion is suspected to be due to the convection of the hot plasma jet through the shock. The fact that reacting species of the plasma jet convect through the shock is seen in the plasma luminosity image shown in figure 5.5 captured with a conventional CCD camera. From the optical emission spectroscopy measurements made in a stagnant chamber, the bulk gas temperature of the pulsed plasma jet is found to be about 700 K. It should be mentioned that no temperature measurement of the plasma jet was made in the presence of the supersonic flow. However it is expected, based on relative brightness of the jet boundary in schlieren images, that the jet should be significantly hotter than free stream ($\approx$ 100 K). Previous studies of "hot spots" introduced upstream of normal shocks, show that as the region of hot fluid passes through the shock, the shock responds by moving upstream [Knight et al. (2003) and Adelgren et al. (2003)]. This is because the local speed of sound is higher than in the surrounding freestream and so the local Mach number is lower. It is well known that greater shock standoff distances are associated with lower Mach numbers. It is possible that the heated gas issuing from the jets may have the same effect and drive the separation shock upstream owing to the enhanced speed of sound. A more detailed discussion of the mechanism of the interaction is given in section 6.4.

5.3.2 Pulsed plasma jet as a vortex generator

The interaction of the pulsed-plasma jet with the separation shock is characterized by a predominant upstream motion of the shock, which happens for all the geometric and discharge settings. However, in the previous section it was shown that the pitched/skewed pulsed-plasma jets cause a cross-stream momentum addition. Hence, they have a potential for application as vortex-generator jets. In this subsection, the vortex generator property of the pulsed-plasma jet is demonstrated. Phase-averaged schlieren imaging and CO_2 PLS imaging were performed for the study. An array of three pulsed-plasma jets with a discharge current of 4.5 A per jet was employed for schlieren imaging. A single pulsed plasma jet with 4.5 A discharge current was employed for PLS imaging. In both the cases, the jet(s) were pitched at 45 and skewed at 90.

Figure 5.6 shows a phase-average schlieren image taken 35 μs from the start of the discharge trigger. An array of three 45° pitched and 90° skewed pulsed plasma jets was employed. The discharge current of each individual pulsed-plasma jet was 4.5 A. The locations of the shock with and without the pulsed plasma jet are marked in the figure. It can be seen that the pitched and skewed jet array, caused a downstream displacement of the separation shock by about $\delta/4$, which in turn implies that the separation bubble length scale has reduced by $\delta/4$. The downstream displacement of the separation shock is likely because the plasma-jets energize the upstream boundary which makes it more resistant to separation. The pitched-skewed plasma jet energizes the boundary layer by generating streamwise vortices into the boundary layer. These vortices entrain the high momentum fluid close to the free stream into the boundary layer thereby energizing the boundary layer and hence making it more resistant to separation. Phase-averaged schlieren images taken at subsequent time delays showed

that the downstream motion lasts for about 5-10 μs, after which the shock moves upstream. The maximum downstream shock displacement occurred at the instant when the pulsed-plasma jet was just upstream of the separation shock. It should be mentioned that this is the first study to demonstrate the use of electric discharges to create vortex generator jets.

For the schlieren imaging results shown above, the pulsing frequency of the pulsed plasma jet was 60 Hz. Subsequently the vortex generator action of a single pulsed-plasma jet was also studied for the pulsing frequency in the kHz range using planar laser scattering. It should be noted that the pulsing frequency of the pulsed-plasma-jet array that was employed for separation shock control studies was also in the kHz range. Hence demonstrating the vortex generator action of the pulsed plasma jet at kHz frequency is more relevant for the flow control studies. Figure 5.7 (a) and (b) show PLS images for the unforced and forced cases, respectively. Figure 5.6 (b) is taken at $40\,\mu s$ after the start of the discharge trigger. The origin is at the center of the jet orifice and the axis is positive along the downstream direction. For the forced case, only a single plasma jet was used and it was pulsed at 1 kHz. The images were acquired at 10 Hz. The discharge current of the pulsed plasma jet was 3.9 A. In both cases, the separation bubble is rendered dark because the fluid temperature inside the separation bubble is higher than the sublimation temperature of CO_2.

One of the major difficulties in identifying the boundary of the separation bubble is that the camera noise causes uncertainty in the identification of the boundary. The rms of the intensity count due to camera dark noise is about 8 counts. Hence, in order to estimate the boundary of the separation bubble, a threshold procedure was adopted. In this procedure, a threshold value of 20 intensity counts is assumed and the representative separation bubble boundary from the PLS image is taken to

be the most downstream boundary where the intensity count is above the threshold intensity. The choice of the threshold intensity count is arbitrary, as long as it is considerably higher than the camera noise. Since both the unforced and forced images shown here are taken from the same experimental run, the seeding density, the laser sheet intensity and the camera gain are identical for both the images. This makes the intensity counts for unforced image and forced image very similar. Hence, a single threshold value was adopted for both the images in order to estimate the separation bubble boundary.

Figure 5.6 (c) and (d) shows the zoomed view of the separation bubble boundary (region marked as dotted circle in fig. 5.6 (b)) for the unforced and forced case respectively. The color-map is adjusted such that the red color marks the region where the intensity is above the threshold value. The most downstream location of this red contour is taken to be representative of the separation bubble boundary. It can be seen in fig 5.6 (c) that the estimated separation bubble boundary is located at $4.9\,\delta$ for the unforced case. This separation bubble boundary has shifted to $5.05\,\delta$ when it is forced by the plasma jet as shown in fig 5.6 (d). Hence, it can be seen that the upstream boundary of the separation bubble has shifted downstream by about $0.15\,\delta$ when the pulsed plasma jet was operated. It should be mentioned that the magnitude of the downstream shift is reasonably insensitive to the choice of the threshold value.

Planar laser scattering imaging explained above facilitates a direct visualization of the separation bubble. This can be contrasted with the schlieren imaging employed earlier (fig.5.6) where the separation bubble extent was inferred from the location of the separation shock. Hence, the PLS image provides a direct demonstration of the vortex generator action of the pulsed-plasma jet. However, the significance of the results in fig 5.7 is that, for this experiment, the plasma jet was pulsed at kilo-

hertz frequencies. This is the first time a kHz frequency range vortex generator jet has been demonstrated. The extent of downstream displacement of the separation bubble was about 0.15δ, which is close to the downstream shift of the separation shock found using schlieren imaging of a 60 Hz pulsed plasma jet ($\delta/4$). Thus, it can be observed that the vortex generator performance of the pulsed plasma jet does not change noticeably when the pulsing frequency was increased from 60 Hz to 1 kHz.

5.4 Parametric study on the performance of the pulsed plasma jet

In the previous section the performance of the pulsed plasma jet as a low momentum disturbance and as a vortex generator jet was demonstrated. Detailed studies were made on the various parameters that affect the performance of the pulsed-plasma jet towards separation shock control. The studies were performed to determine how different parameters affect the strength of the perturbation to the flow. Phase-average schlieren imaging was performed for this parametric study and the pulsing frequency of the plasma jet was fixed at 60 Hz. An array of three pulsed-plasma jets was employed throughout this study. The results obtained in this study at 60 Hz pulsing would be extended to kHz pulsing frequencies, which were used for the separation shock control studies.

5.4.1 Effect of discharge current

It was shown in the previous chapter that the exit velocity and the bulk gas temperature of the pulsed-plasma jet increase with increasing discharge current. The effect of increasing discharge current on the upstream forcing of the separation shock was studied. An array of three unskewed pulsed-plasma jets with fixed pitch angle

(30°) were employed. All the discharge and geometric parameters but for the discharge current was fixed during the study. The pulsed-plasma jet array was located $4\,\delta$ upstream of the compression corner. Two discharge currents, 1.2 A and 4.5 A per individual plasma jet, were tested. The array of 1.2 A pulsed plasma jets had a jet exit velocity of about $230\,m/s$, whereas the array of 4.5 A pulsed-plasma jets had a jet exit velocity of about $300\,m/s$. Figure 5.8 (a) and (b) shows the phase-average images for the 1.2 A pulsed plasma jet array and 4.5 A pulsed plasma jet array, respectively, which corresponds to maximum upstream shock motion in each case. Comparing figures 5.8 (a) and (b) it can be observed that the average maximum upstream displacement of the separation shock was $\delta/2$ with 1.2 A pulsed plasma jet array, whereas it is about δ for the 4.5 A pulsed plasma jet array. This shows that the upstream displacement of the separation shock increases as the discharge current is increased. Hence, the upstream displacement of the shock depends on the input peak power. It was earlier reported by Selig and Smits (1991) that the extent of the upstream shift of the separation shock scaled with the strength of external blowing, and thus the present results are consistent with observations made by previous researchers. It should be noted that the time delay at which the maximum upstream displacement occurs was about $50\,\mu s$ after the start of the discharge trigger for both the cases. The time taken by the separation shock to recover to its mean unforced location was also estimated from the phase-average schlieren images taken at different time delays. It was found that the separation shock takes about 100 μs to recover to its mean position with 1.2 A pulsed plasma jet array forcing, whereas it takes about 150 μs to recover with 4.5 A pulsed plasma jet array forcing. Thus, the time scale of recovery of the shock also depends on the strength of the incoming disturbance.

From the above paragraph, it is clear that the discharge current affects the

amplitude of the induced upstream motion of the separation shock and the recovery time scale. The discharge current also has an impact on the VG action of the pulsed-plasma jet. The effect of the discharge current on the VG action of the pulsed-plasma jet was studied by studying the VG action at different discharge current magnitude, keeping all the other discharge and geometric parameters fixed. An array of three unskewed pulsed-plasma jets, pitched at 30° were employed for the study. Two different discharge currents, 1.2 A per jet and 4.5 A per jet, were studied. These discharge and geometric configurations are identical to the ones used in the study discussed in the previous paragraph. Figure 5.9 shows the schlieren image of the flowfield when the pulsed-plasma jet was just upstream of the separation shock. It was mentioned in section 5.3.2 that the vortex generator action occurs for about 5 to 10 μs when the pulsed plasma jet is just upstream of the separation shock. Thus, the time instant at which the schlieren image was captured corresponds to the instant of maximum VG action. The mean separation shock location of the unforced case and the phase average mean shock location for the forced case are marked. In addition, a linear extrapolation of the shock is made to the floor in order to mark the position of shock foot for both the cases. It can be seen in Fig. 5.9(a) that with the 1.2 A pulsed-plasma jet array, no noticeable downstream displacement of the separation shock could be observed. This shows that the streamwise vorticity generated by the 1.2 A pulsed-plasma jet was too weak to cause noticeable downstream shift of the separation shock. Fig 5.11 (b) shows the schlieren image of the flowfield with a 4.5 A pulsed-plasma jet array at the same instance as in Fig. 5.9 (a). It can be seen that there is a slight, but noticeable, downstream shift in the separation shock when forced using the 4.5 A pulsed-plasma jet array. The result shown above indicates that the VG action of the pulsed-plasma jet array increases with increasing discharge current. It was shown in chapter 4 that the jet exit velocity of the pulsed-plasma

jet increases with the discharge current. Hence, a pulsed-plasma jet generated with higher jet velocity (higher discharge current) causes a stronger VG action compared to a jet with lower jet velocity (low discharge current). This trend is consistent with the previous studies (Johnston and Nishi (1990); Compton and Johnston (1992); Zhang and Collins (1997)), which show that the strength of the streamwise vorticity generated by a pitched/skewed jet increases with increase in the velocity of jet.

5.4.2 Effect of geometric parameters

The geometric configurations of the jet exit were modified to study the effect of the geometry on VG action of the pulsed plasma jet. The discharge currents and, hence, the jet exit velocities were kept identical while the exit geometry was varied. First, the experiments were done to investigate the effect of changing the jet pitch angle (without changing skew). It is known that the pitched jet causes momentum addition to the flow and also creates streamwise vorticity. An array of three pitched jets was used. The instantaneous discharge current of each pulsed plasma jet was fixed at 1.2 A and the jet array was located 4δ upstream of the compression corner. Pitch angles of 0° (normal injection), 30° and 60°were tested. It was observed (figures not shown) that as the pitch angle was changed, the global character of the interaction remained the same as that of normal injection, although the shock moved slightly smaller upstream distances with increase in pitch angle (0 to 60 degrees). However, no noticeable downstream displacement of the separation shock was observed. Hence, it was concluded that pitch angle alone was not very effective in causing noticeable VG action from the pulsed plasma jet.

In order to increase the streamwise vorticity produced by the pulsed plasma jet, the jets were pitched at 45° and skewed at 90°. This pitch and skew angle config-

uration has been shown to produce maximum streamwise vorticity in incompressible flow studies (e.g. Zhang and Collins (1997)). An array of three jets was placed 5 δ upstream of the compression corner. In order to study the effect of skewness, the interaction of a 30° pitched and unskewed pulsed plasma jet was compared with that of a 45° pitched and 90° skewed pulsed-plasma jet. The differences in pitch angle (between 30° and 45°) of the jet did not seem to affect the VG action of the plasma jet. The discharge current of the individual pulsed-plasma jet was set at 4.5 A for both cases. Figures 5.10 (a) and (b) show phase-average schlieren images acquired 35 μs after the discharge trigger for the cases of unskewed and skewed pulsed-plasma jet arrays. The average shock position and angle without employing the pulsed-plasma jet is also marked. In addition, a linear extrapolation of the shock is made to the floor in order to mark the position of shock foot for each case. From figure 5.10 (b) it is seen that the pulsed-plasma jet array causes the shock foot to move an average distance of 0.3δ downstream. A small downstream motion of the shock foot can also be seen with the unskewed jet shown in fig. 5.10 (a). However, the magnitude of downstream displacement of the separation shock is considerably higher with the skewed jet as compared to the unskewed jet. This shows that the streamwise vorticity generated by a pitched and skewed jets is stronger than that generated by an unskewed jet. Thus, the pitched and skewed jet seems to work better than an unskewed jet as a vortex-generator. This result is consistent with several previous studies on VG jets in both incompressible and compressible flows.

5.4.2.1 Effect of duty cycle

It was found during the static tests that the jet exit velocity stayed relatively independent of the pulse width of the discharge current beyond a pulse width of about

$20\mu s$. However, no direct impact of increasing the pulse duration on the plasma jet was studied. This issue is addressed briefly in this section. Figure 5.11(a) and (b) shows plan-view PLS images of the flowfield with plasma-jet injection with pulse-widths of 20 (fig. 5.11(a)) and 40 μs (fig. 5.11(b)). The images were taken at a wall normal distance of 0.5δ. A single pulsed-plasma jet was used and the discharge current of the pulsed plasma jet was 3.9 A for both the cases. The pulsed-plasma jet and the wake behind the jet, seen in fig. 5.11 (a) are rendered dark owing to sublimation of solid CO_2, as marked in the figure, while the surrounding flow is seeded with solid CO_2 which scatters light. The dark region thus gives an approximate extent of the pulsed-plasma jet in the flow. Figure 5.11 (a) corresponds to a pulse width of 20 μs and figure 5.11 (b) corresponds to a pulse width of 40 μs. The images shown were taken 50 μs after the start of the discharge trigger so that the jet has fully penetrated to the imaging plane during imaging. It can be clearly seen that the plasma jet with the $40\mu s$ pulse duration extends to a larger streamwise length (extent of the dark patch) compared to the 20 μs pulse duration plasma jet. This illustrates that the jet was issuing for a longer duration for the longer pulse width case. Figure 5.11 (a) and (b) also show that the leading edge of both the jets is located at the same spanwise location with respect to the jet orifice. This implies that the momentum of the 20 μs and 40 μs jets should have been the same when the jets first emerged. Figure 5.12 shows the trajectory of the leading edge of the pulsed plasma jet for both pulse widths at a wall normal height of $\frac{y}{\delta} = 0.5$. It can be clearly seen that both the jets are convected at the same velocity, which corresponds to the local boundary layer velocity. Thus it can be concluded that for this case the strength of the disturbance, viz. the momentum of the plasma jet, is the same for both the cases. However, the jet issues for a longer duration with the 40 μs pulse-width pulsed plasma jet compared to the 20 μs pulse-width plasma jet. Hence, by changing the pulse width of the

pulsed-plasma jet, different duty cycle jets are produced.

The response of the separation shock to changing duty cycle was studied for an array of three pulsed plasma jets with 20 μs and 50 μs pulse durations. The discharge current of the individual pulsed plasma jet was fixed at 2 A for both the cases, which roughly corresponds to a jet exit velocity of about 275 m/s. The separation shock boundary layer interaction was generated by a 24° compression corner whose span was about 75% of the test section width. The plasma jet array was placed 6δ upstream of the compression corner. The time resolution of the phase-average images for this study is 25 μs. Attention has been paid to the magnitude of upstream motion of the separation shock and the time of recovery of the separation shock to its undisturbed mean position. It should be noted that a short duration downstream motion (VG action) was reported in section 5.3.2 with phase-average schlieren imaging with 5 μs time resolution. The present time resolution of 25 μs is too coarse to capture the VG action for both 20 μs and 50 μs pulse-width pulsed plasma jet. The upstream displacement of the separation shock begins to occur at 50 μs from the start of the discharge trigger and reaches its maximum displacement at 75 μs. Figure 5.13 shows the comparison of the location of the separation shock caused by 20 μs pulse-width pulsed plasma jet and 50 μs pulsed-width pulsed plasma jet. Both the images were acquired at 75 μs after the start of the discharge trigger. The time delay of 75 μs corresponds to the time when the entire plasma jet had convected into the separation shock. On comparing the magnitude of upstream motion with changing duty cycle it was found that the separation shock was shifted upstream by about 1 δ with the 50 μs pulse-width pulsed plasma jet, whereas it was shifted by about 0.5δ with a 20 μs pulse-width pulsed plasma jet. The trajectory of the forced separation shock was also followed at different time delays in order to compute the time taken by the perturbed

separation shock to recover to its average unforced position. For the 20 μs pulse-width pulsed plasma jet this recovery time is about 150 μs and for the 50 μs pulse-width pulsed plasma jet it is about 400 μs. Thus it is clear that with increasing pulse width, the separation shock shifts upstream to a greater distance and takes a longer time to recover. The average shock recovery velocity was computed from the maximum upstream displacement of the separation shock and its recovery time. It should be noted that the average recovery shock speed for both the cases was roughly about 12 m/s. A detailed study of the shock speed during and after forcing is presented in the next chapter.

Thus the global characteristics of the pulsed plasma jet / separation-shock interaction with changes in geometric parameters of the plasma jet are as follows:

- The pitched and skewed jet seems to work as intended as a vortex-generator that energizes the upstream boundary layer since it causes the separation shock to move downstream briefly. The maximum downstream shift was observable for a jet with 45° pitch angle and 90° skew angle and 4.5 A discharge current per jet.

- The pitched-only jet and the pitched and skewed jet (at longer times) both caused upstream motion of the separation shock. The upstream motion may be due to the injection of low density (high temperature) fluid into the boundary layer. The extent of upstream motion is found to depend on the location and the strength of the jet.

- The recovery of the shock to its undisturbed position after the jet fires is considerably longer than the time required for the jet fluid to convect past the interaction at the freestream velocity.

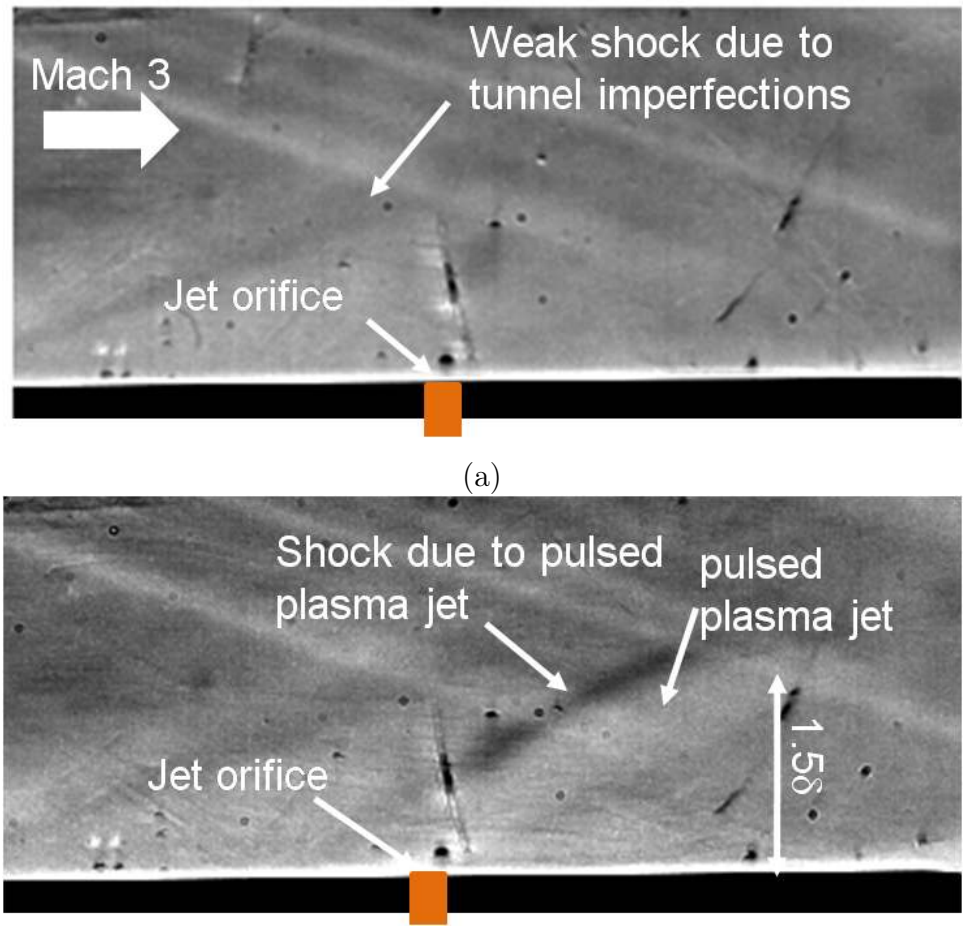

Figure 5.1: Schlieren image showing the penetration of the pulsed plasma jet injected normal to the incoming flow. The discharge current of the plasma jet was set at 1.2 A, (a) schlieren image without jet injection, and (b) schlieren image captured 35 μs after the jet injection.

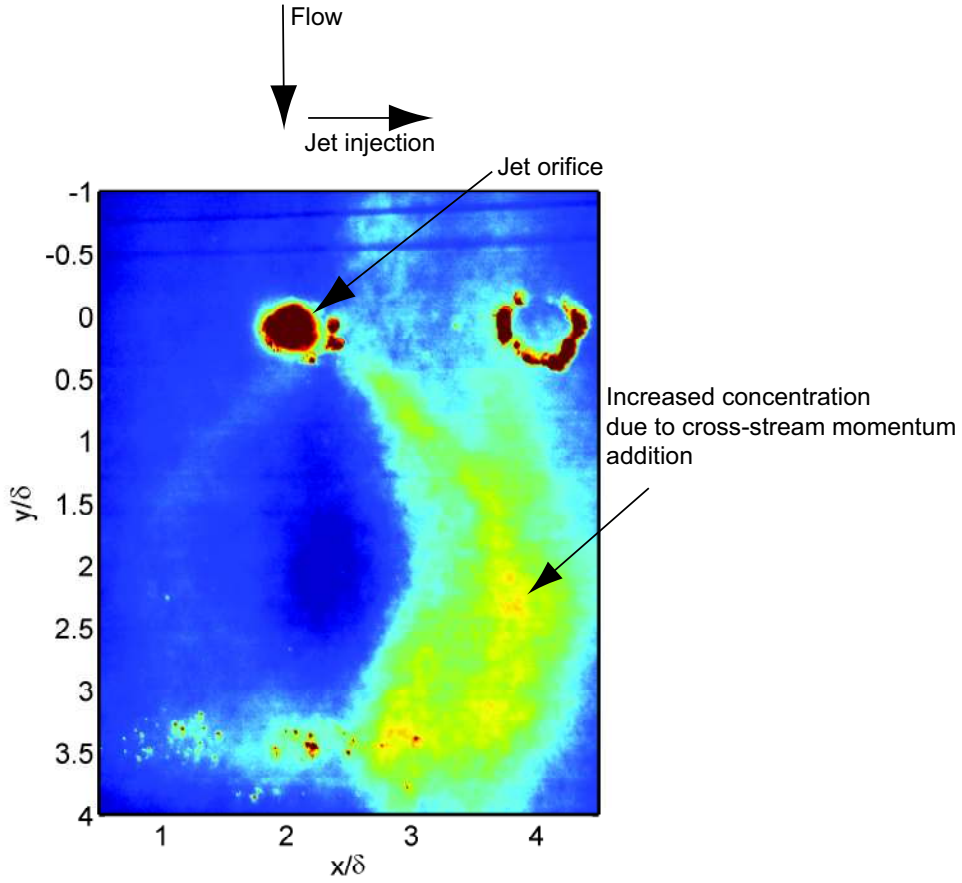

Figure 5.2: Planar laser scattering (PLS) images to illustrate the cross-stream momentum generated by a single pitched and skewed pulsed-plasma jet. The discharge current of the pulsed-plasma jet was 4.5 A. The plasma jet was pitched at 45° and skewed at 90°. The image was taken 40 μs after the start of the discharge trigger.

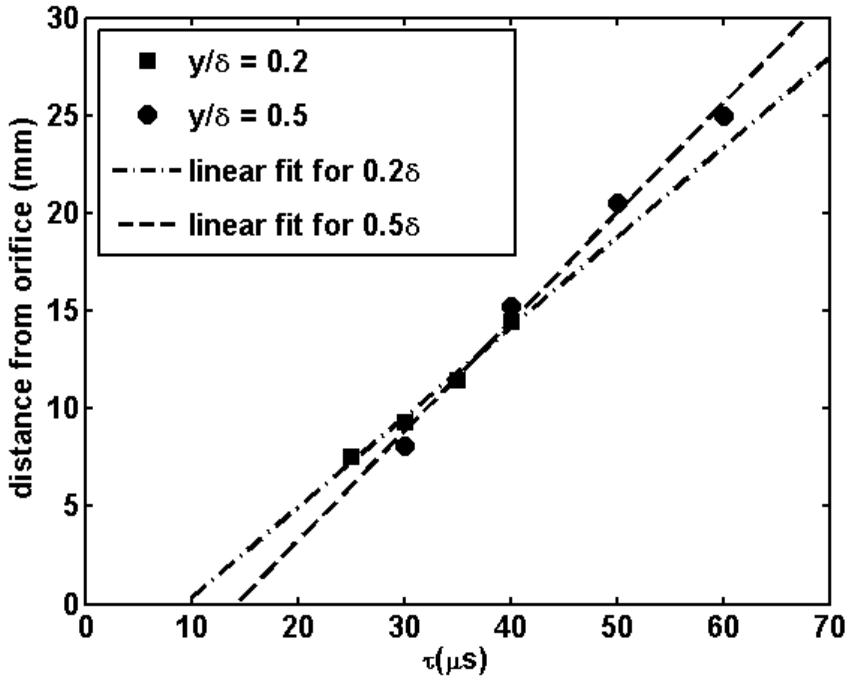

Figure 5.3: Trajectory of the leading edge of the pulsed-plasma jet measured at wall normal locations $\frac{y}{\delta} = 0.2$ and 0.5. A linear fit was made as shown in the figure in order to determine the convection velocity of the pulsed plasma jet at different wall normal locations. The discharge current was set at 3.9 A.

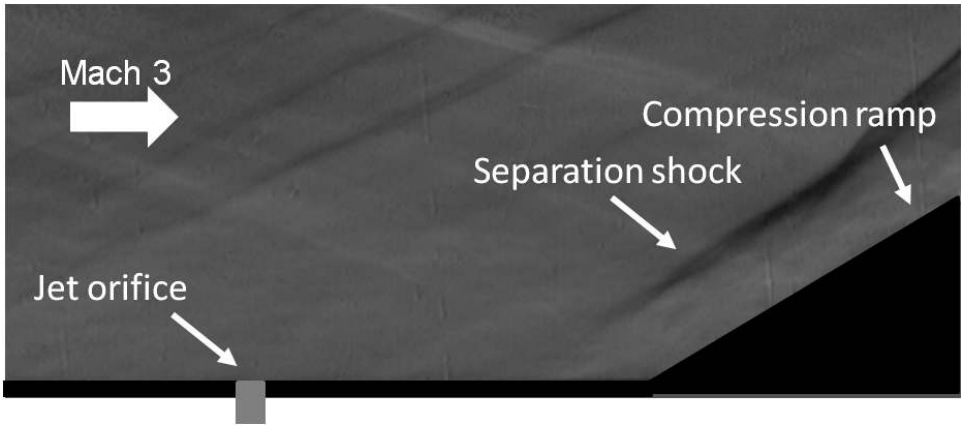

(a)

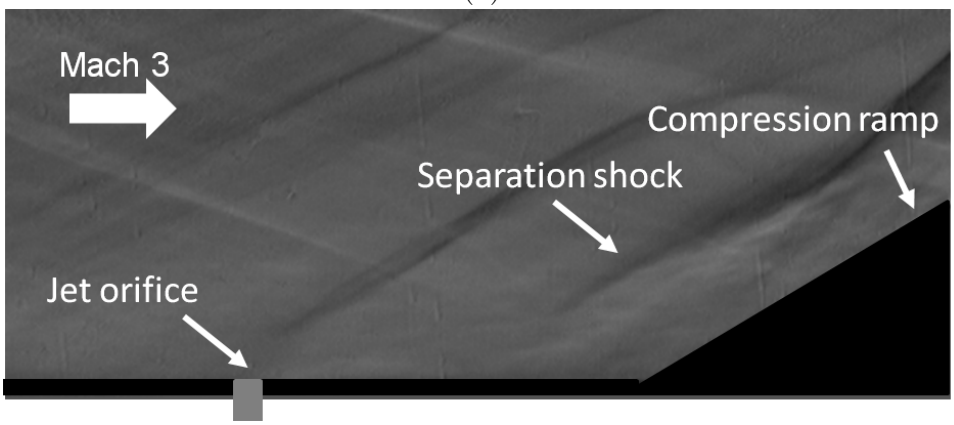

(b)

Figure 5.4: Instantaneous schlieren images to illustrate the effect of the pulsed-plasma jet injection on the separation shock. The plasma jet was injected 5δ upstream of the compression corner (a) unforced case, and (b) forced case. The discharge current of the individual jet was 3.9 A and (b) was taken 40 μs from the start of the discharge trigger.

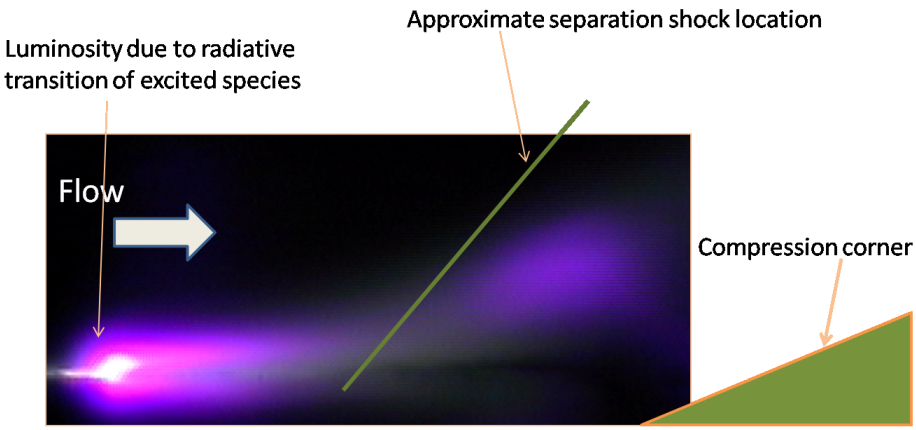

Figure 5.5: Luminosity image of the pulsed plasma jet injected into the Mach 3 flow. The luminosity is mainly due to the radiative transitions of the excited nitrogen molecules.

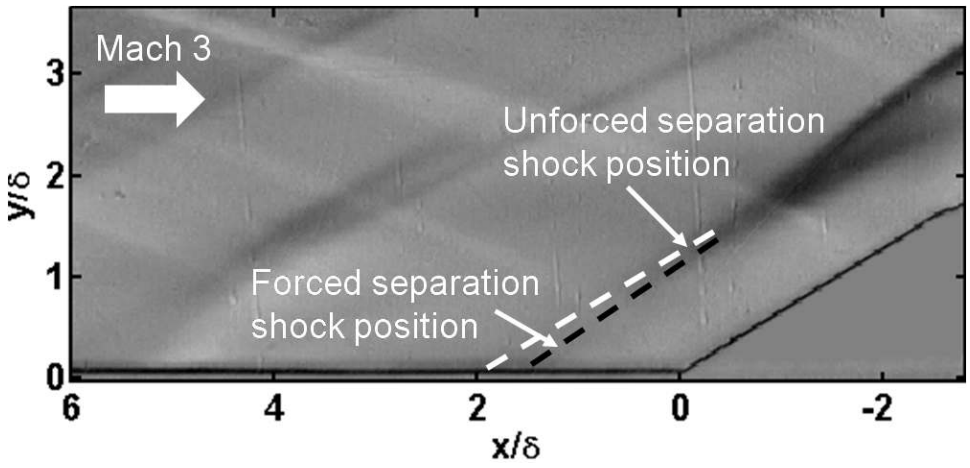

Figure 5.6: Illustration of the vortex generator action caused by a plasma-jet pulsed at 60 Hz. The pulsed plasma jet was pitched at 45° and skewed at 90°. The discharge current of the plasma jet was 4.5 A and the image was taken 35 μs after the start of discharge trigger.

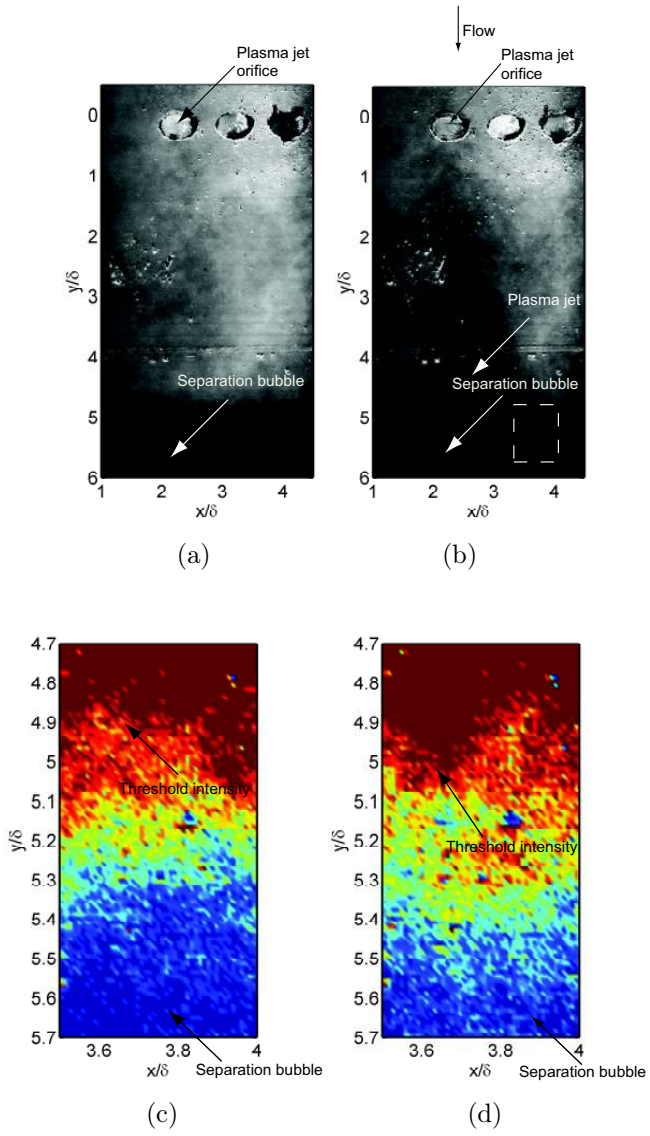

Figure 5.7: PLS images to demonstrate the vortex generator action of the pulsed plasma jet at kHz pulsing rates. (a) PLS image of the unforced case and (b) PLS image of the forced case. (b) was taken 40 μs after the start of the discharge trigger, which corresponded to maximum VG action. The dotted region shown in (b) marks the region shown in (c) and (d). (c) and (d) show the zoomed view of the region close to the separation bubble boundary where the VG action is seen. (c) corresponds to the unforced case and (d) corresponds to the forced case. The region with intensity above the threshold value is shown in red. The plasma jet was pulsed at 1 kHz and the discharge current was 3.9 A.

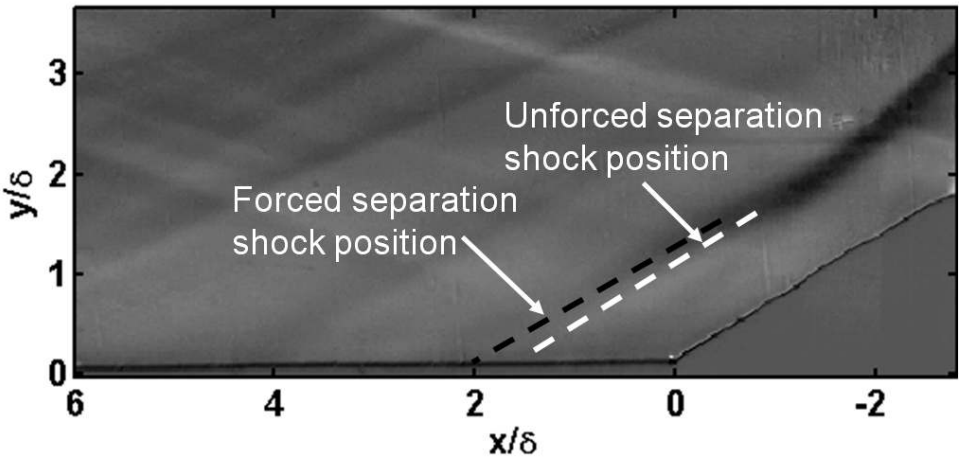

(a)

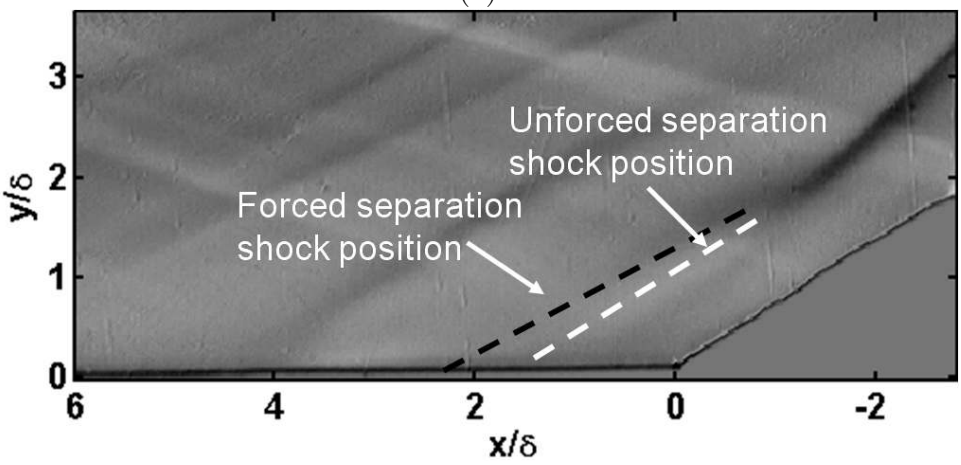

(b)

Figure 5.8: Schlieren image showing the effect of increasing current on the upstream displacement of the separation shock. (a) corresponds to a discharge current of 1.2 A while (b) corresponds to a discharge current of 4.5 A. The plasma jet was pitched at 30°, without skew. All the other discharge and geometric parameters but for the discharge current were identical for (a) and (b). Both images were taken $45\mu s$ after the start of discharge trigger, which corresponds to maximum upstream separation shock displacement

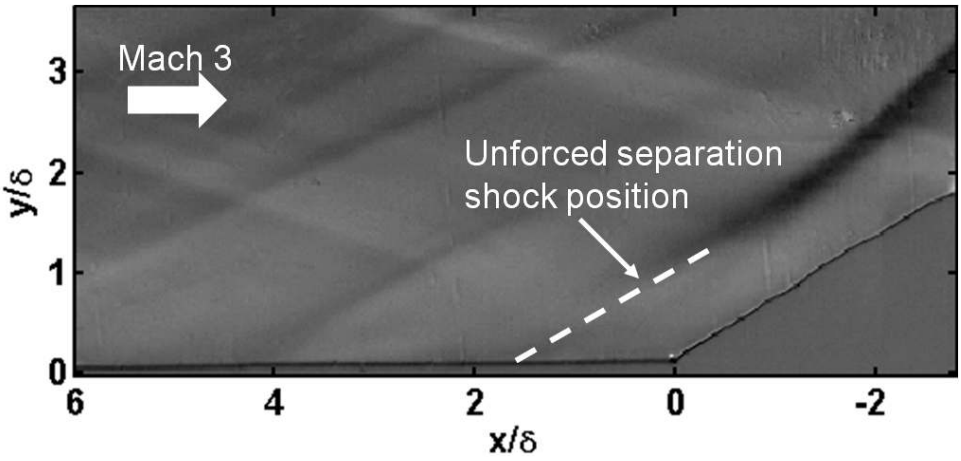

(a)

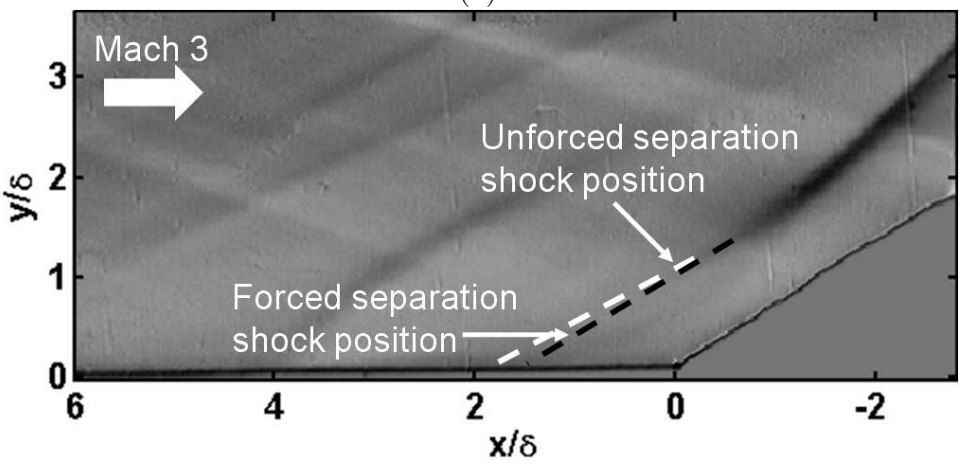

(b)

Figure 5.9: Schlieren image illustrating the effect of increasing discharge current on the vortex generator action of the pulsed plasma jet. (a) corresponds to a 1.2 A discharge current while (b) corresponds to a 4.5 A discharge current. The plasma jet was pitched at 30°, without skew. All the other discharge and geometric parameters but for the discharge current were identical for (a) and (b). Both images were taken 35 μs after the start of the discharge trigger.

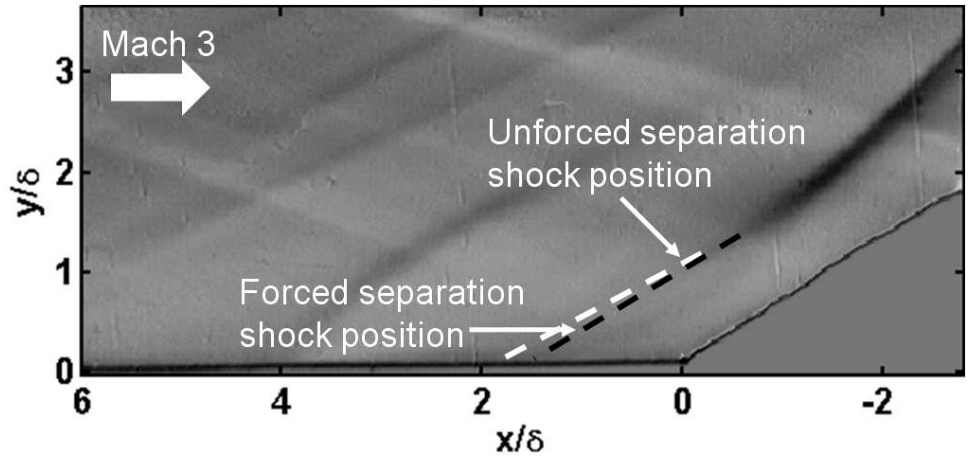

(a)

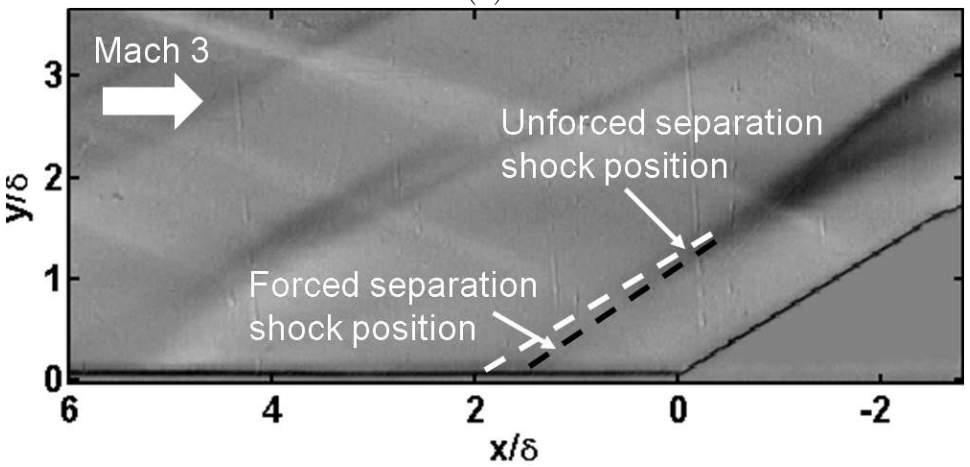

(b)

Figure 5.10: Schlieren imaging showing the effect of the skew angle on the vortex generator action of the pulsed plasma jet. (a) corresponds to an unskewed jet while (b) corresponds to a 90° skewed jet. The discharge current was set at 4.5 A per jet and the jet orifice was pitched at 30° for (a) and 45° for (b).

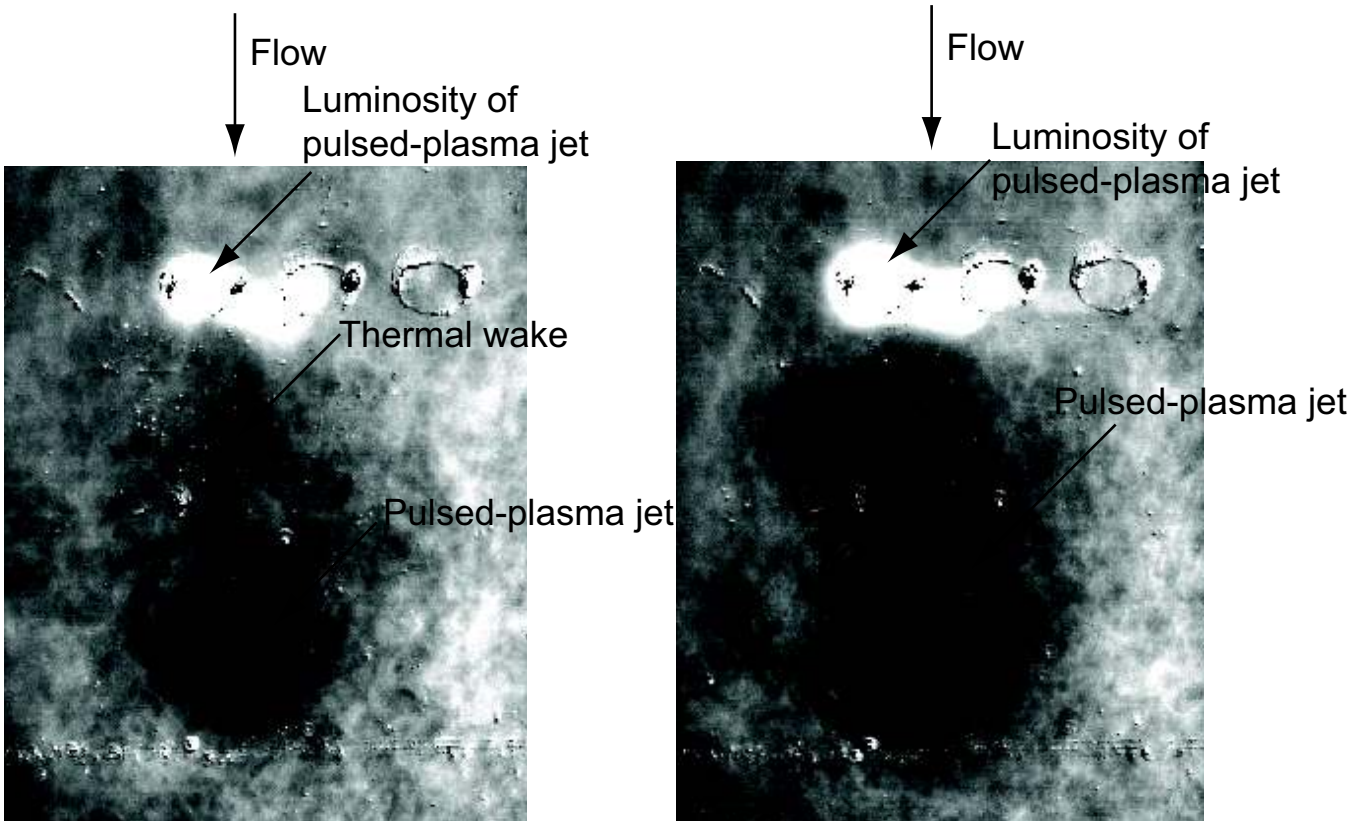

(a) (b)

Figure 5.11: PLS images to illustrate the effect of increasing the pulse width of the pulsed plasma jet. (a) corresponds to a 20 μs pulse duration and (b) corresponds to 40 μs pulse duration. The discharge current for both cases was 3.9 A and the jet orifices were pitched at 45° and skewed at 90°. The images were taken 50 μs after the start of discharge trigger.

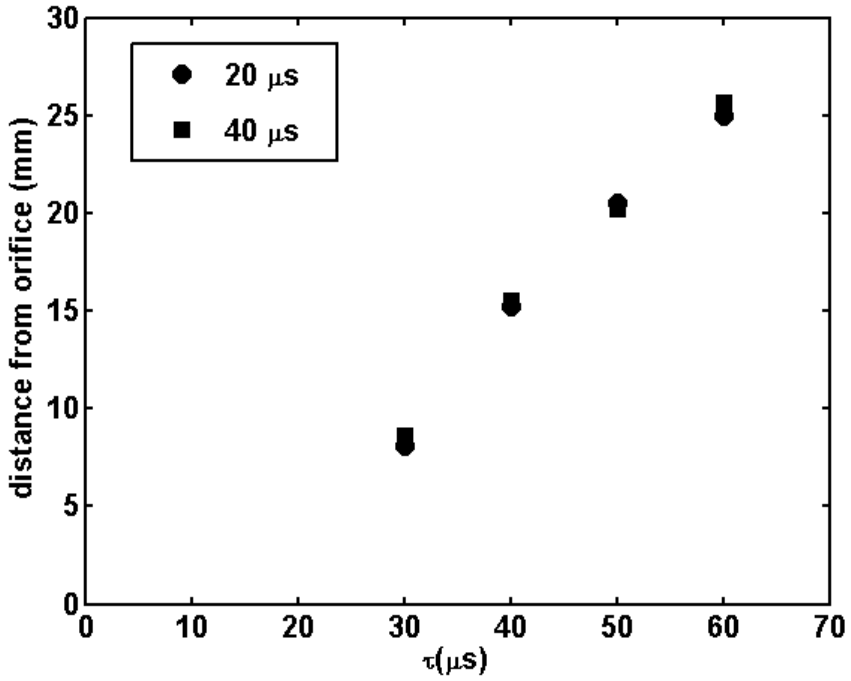

Figure 5.12: Comparison of the trajectory of the leading edge of the pulsed-plasma-jet with different pulse durations: 20 μs and 40 μs. The trajectory is measured at a wall normal location of $\frac{y}{\delta} = 0.5$. The discharge current of the pulsed plasma jet was set at 4.5 A and a 45° pitched and 90° skewed jet was used for both cases.

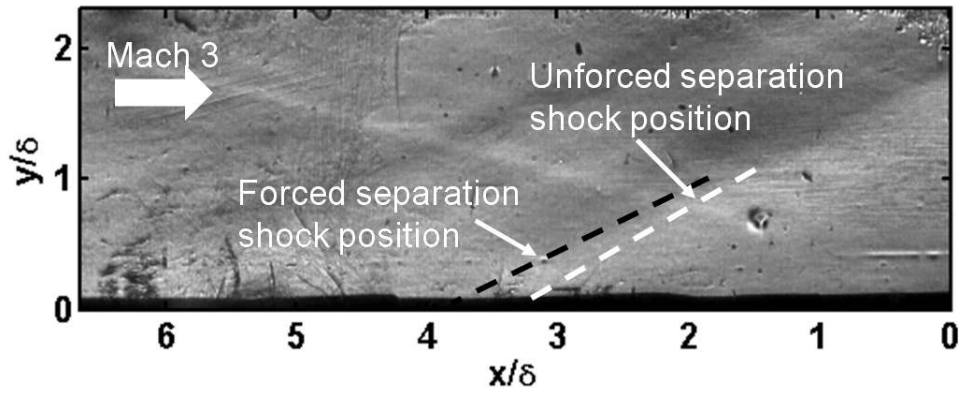

(a)

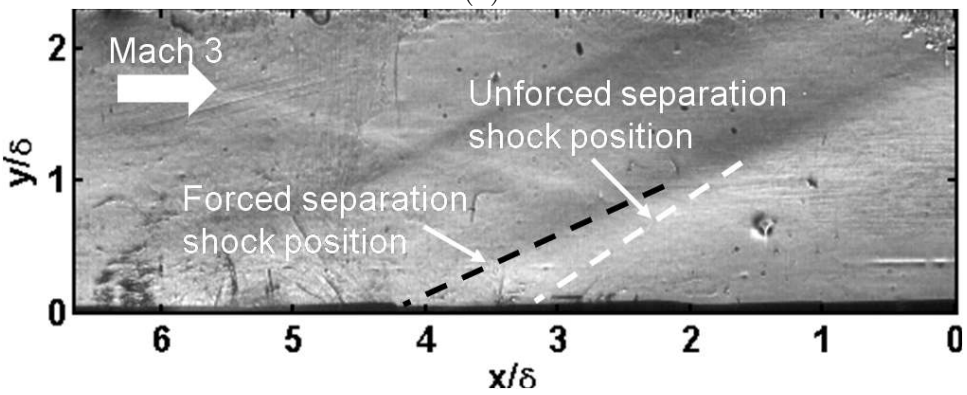

(b)

Figure 5.13: Schlieren images to illustrate the upstream displacement of the separation shock with increasing pulse duration of the pulsed-plasma jet. (a) corresponds to a $20\mu s$ pulse duration and (b) corresponds to $50\mu s$ pulse duration. The discharge current for both cases was set at 2 A, and a 45° pitched and 90° skewed jet was used for both the cases.

Chapter 6

Interaction between the pulsed-plasma jet and the separation shock: Unsteady flow structure

Schlieren imaging was performed at 10 kHz to study the response of the separation shock to pulsed-plasma jet arrays in a time-resolved manner. The discharge current through each pulsed-plasma jet was 2 A and the pulse duration was 50 μs unless stated otherwise. A majority of the study was made with the pulsed-plasma jet located 6δ upstream of the compression corner. This injection location was also upstream of the separation shock. The pulsed-plasma jet was pitched at 45° and skewed at 90° for this injection location. A study was also made of the effect of the location of the pulsed-plasma jet on its performance.

6.1 Actuator placed in the upstream boundary layer

The time resolved characterization of the response of the separation shock to the pulsed-plasma jet array injected into the upstream boundary layer was accomplished using 10 kHz schlieren imaging. The actuator was located 6 δ upstream of the compression corner. The intermittent region was located about 3 δ upstream of the compression corner. A representative time sequence that shows the unsteady motion of the separation shock during 400 μs of a 2 kHz discharge cycle is shown in fig. 6.1. The pulsing frequency of 2 kHz ($St_L \approx 0.04$) was chosen so that it lies close to the peak of the low frequency unsteadiness of the separation bubble, which

will be discussed later. Fig. 6.1 (a) shows the location of the separation shock 75 μs after the start of the discharge trigger. It was earlier observed from phase-locked CO_2 PLS imaging (described in the previous chapter) that the jet reaches the separation shock about 45 μs after the start of the discharge trigger and the entire pulsed-plasma jet convected through the separation shock after about 100 μs. From fig. 6.1 (a) it can be seen that the separation shock moves upstream by about 0.7 δ (3 mm) as the pulsed-plasma jet convects through the shock. This corresponds to a shock velocity of about $0.05U_\infty$. Figure 6.1(b) corresponds to the time, t = 175 μs, when the entire pulsed-plasma jet has convected through the separation shock (where t is the time delay from the discharge trigger). It can be seen that the separation shock in fig. 6.1 (b) is at a downstream position compared to fig. 6.1 (a); however, it has not reached its mean unforced position. In fact, it continues to recover to its mean position in fig. 6.1 (c) and 6.1 (d) corresponding to 275 μs and 375 μs after the start of the discharge trigger. In Fig. 6.1 (d), i.e. after about 375 μs, it has reached its mean unforced position. Thus, the separation shock spends about 70% of the time upstream of the unforced mean shock location.

A shock tracking program was developed in house to capture the motion of the separation shock from the schlieren images. The program identifies the presence of the shock from the relative pixel intensity across the row at different wall-normal locations. The closest location above the wall at which the program can unambiguously identify the shock is 0.5 δ. The shock location used for analysis was computed as the average location over a height of 0.2δ (i.e., average shock location between 0.5 δ to 0.7 δ). Note that this analysis is used only to illustrate the periodic motion of the separation shock and no quantitative inference was made about the separation shock foot location. To start with, figure 6.2(a) shows the separation shock motion of the

unforced case with respect to its mean. The Δt between successive points is 100 μs (0.1 ms). It can be seen from the time trace of separation shock motion that there is a broadband jitter without any clear periodic motion. The maximum amplitude upstream and downstream motion of the separation shock is about $0.4\,\delta$ and the separation shock tends to stay within +/- $0.2\,\delta$ from the mean location for the majority of the time. Figure 6.2(b) shows the separation shock motion with respect to the mean unforced shock location when forced using pulsed-plasma jet array over 20 injection cycles (100 images). The pulsing frequency of the discharge was 2 kHz and the discharge current through each jet was 2 A. The mean unforced location is denoted by $\frac{x}{\delta} = 0$. The first image was taken 25 μs (0.025ms) after the start of the discharge trigger. It can be clearly seen that the separation shock moves over $0.7\,\delta$ between 25 μs (0.025 ms) and 125 μs (0.125 ms) and it repeats over all injection cycles. This quick upstream motion is followed by a rather gradual recovery motion. It can be seen that in a majority of the injection cycles shown, the separation shock reaches farther downstream (to about $-0.3\,\delta$) as compared to the unforced case (where the typical downstream motion extends to about -0.2δ). Finally, it is also clear that the broad aperiodic motion of the shock seen in the unforced case does not occur when forced. This shows that the separation shock motion has been locked to the pulsing of the jet.

Figure 6.3 (a,b) shows PDFs of the separation shock velocity for different portions of the forcing cycle. Approximately 1500 images (300 cycles) were used to compute the statistics. Positive velocities correspond to downstream shock motion and negative velocities correspond to upstream shock motion. Figure 6.3(a) is the P.D.F of maximum upstream (negative) velocity of the separation shock over the first half of the cycle. Note that this velocity can be positive if no negative velocity occurs

during this time window. Figure 6.3(b) shows the maximum downstream (positive) velocity over the second half of the forcing cycle, i.e., during the recovery of the separation shock after forcing. The upstream shock motion corresponds to the response of the shock due to the passage of the pulsed-plasma jet, and the downstream shock motion corresponds to the recovery of the separation shock to its equilibrium position, which in turn corresponds to the relaxation of the separation bubble perturbed by the pulsed-plasma jet (discussed later). The upstream shock velocities seem to encompass velocities between 0 to 35 m/s, which correspond to 0 to 6% U_∞ with the most probable value of about 3% U_∞. However, the downstream shock velocities seem to be limited to 0 to 21 m/s, which corresponds to 0 to 3.5% U_∞, with the most probable value of about 12 m/s, or 2% U_∞. Interestingly, Gonsalez and Dolling (1993) measured shock velocities for a wide-range of shock/boundary layer interactions and found that the typical shock foot velocity was between 2 - 3% of U_∞. The present case seems to correspond to one where the separation shock is perturbed upstream of its mean position and then allowed to recover naturally. PIV results presented later in this chapter show that the downstream recovery motion of the separation shock corresponds to the relaxation of the separation bubble excited by the pulsed-plasma jet. It should also be noted in fig 6.3(b) that there is a small fraction of velocities ($\approx$ 12 %) which correspond to upstream motion ($U_{shock}/U_\infty < 0$). This is because in those cases, the separation shock has fully recovered from the effect of forcing before the next pulse and it executes its natural unforced (upstream) motion before the next pulse arrives. Thus, it is clear, qualitatively, from the above discussion that the pulsed-plasma jet injection has a profound effect on the separation bubble unsteadiness. The broadband aperiodic nature of the separation bubble unsteadiness seems to be converted to a periodic motion with the help of pulsed-plasma jets. In order to make a quantitative study of the effect of plasma-jet pulsing on the separation bubble

unsteadiness, wall pressure fluctuation measurements were performed.

6.2 Wall pressure fluctuation measurement of SWBLI forcing

To quantify the effect of upstream pulsed injection on the separated flow unsteadiness, the power spectra of the wall-pressure signals measured at different locations under the shock / boundary layer interaction region were computed. For this part of the study, only a single 45° pitched and 90° skewed pulsed-plasma jet was used, since employing multiple jets resulted in severe electromagnetic (EM) noise and eventual transducer damage (see appendix B). The pulse duration of the plasma jet was set at $20\,\mu s$ throughout the study. Different jet pulsing frequencies and injection locations were tested. The spanwise location of the transducer was roughly in line with the path of the pulsed-plasma jet, which was determined by using phase-locked plan-view PLS imaging. Figure 6.4 shows sample power spectra where the pulsed-plasma jet was issued from the fixed location of $6\,\delta$ upstream of the compression corner, and pressure measurements were made at different downstream locations under the separated flow. In the present study, the pressure-measurement locations are given relative to the interaction length L, which is defined as the distance between the mean separation shock-foot location (inferred from schlieren imaging) and the compression ramp corner. A change in normalizing length scale is made because the pressure fluctuation studies in canonical SWBLI found in the literature uses the interaction length as the normalizing length scale. For the present case $L \approx 3\delta$, which, in physical units, is about $12\,mm$.

6.2.1 Interaction of plasma jet with different regions of SWBLI

The interaction of pulsed plasma jet with SWBLI unsteadiness was studied by measuring the wall pressure fluctuations at different locations inside SWBLI region. Pressure fluctuations with and without upstream forcing were measured at $x/L = 0.95$, 0.86, 0.66 and 0. These measurement locations span the range of the intermittent region to the compression ramp corner. The pulsed-plasma jet was located $6\,\delta$ upstream of the compression corner for these measurements. The pulsing frequency of the plasma jet was fixed at 2 kHz which translates to a Strouhal number based on interaction length, defined as $St_L = fL/U_\infty$, of 0.04. Wall pressure fluctuation measurements made in the intermittent region for the unforced case, shown in figure 6.4(a), shows that the low frequency unsteadiness of SWBLI occurs for Strouhal number in the range of $St_L \approx 0.02 - 0.05$. This unsteadiness frequency coincides with those of a canonical SWBLI reported previously (Gonsalez and Dolling (1993); Dupont et al. (2005)). The impact of the pulsing is studied by comparing the power spectral density of the unforced and forced cases.

Figure 6.4 (a) shows the plots of power spectral density (PSD) of wall-pressure fluctuations measured under the intermittent region ($x/L = 0.95$), normalized by the square of the mean pressure, with and without upstream forcing. It should be noted that the data are presented without normalizing by the RMS fluctuations in order to study the quantitative changes in the power spectra. The spectra of both the forced and unforced cases contain noticeable spikes at discrete frequencies. The spikes in the unforced case are due to structural vibration of the splitter plate that holds the transducer. The spikes in the forced case occur because of structural vibration as in the unforced case, and also because of the electromagnetic noise associated with the plasma discharge. The spikes due to EM noise occur at the pulsing frequency and its

higher harmonics. The spikes due to structural vibration and EM noise are marked in the figure. It should be noted that the argument for using the power spectra, despite the presence of interference-spikes, is because the objective of this study is to observe the changes induced by the pulsing over broad frequency bands, and no quantitative conclusions are drawn at the specific frequencies that coincide with the spikes.

In Fig. 6.4(a), each plot corresponds to an average of three experimental runs that were highly repeatable. Without forcing, the power spectrum is dominated by energy at low frequency as is typical of a canonical SWBLI (Gonsalez and Dolling (1993); Dupont et al. (2005)). The Strouhal number based on separation length at the location where the peak of the power spectrum occurs is about 0.023, which is in the range reported in several previous SWBLI studies (0.02-0.05) [Gonsalez and Dolling (1993); Dupont et al. (2005)]. The frequency of plasma jet forcing was chosen such that it coincided with the low frequency range of the separation shock motion. The maximum amplitude of the frequency-multiplied power spectrum normalized by the square of mean wall pressure is about 0.65×10^{-3}. It can be clearly seen that with forcing there are noticeable changes in the power spectrum of the pressure fluctuations. The magnitude of the peak pressure fluctuations at separation shock frequencies ($St_L = 0.02 - 0.05$) has decreased by about 40% and the maximum amplitude of the pre-multiplied power spectrum normalized on the square of mean pressure is about 0.4×10^{-3}. Above Strouhal number of 0.1, the spectra of forced and unforced cases overlap, indicating that the higher frequencies are not affected by the forcing.

Figure 6.4(b) shows the power spectra at $x/L = 0.66$, where the unforced case shows the pressure fluctuations are shifted toward higher frequencies than those under the intermittent region (fig. 6.4 (a)). The unforced power spectrum shows the

presence of two high-amplitude bands separated by a relatively low-amplitude valley. These broad peaks occur at $St_L = 0.03 - 0.08$ and $0.2 - 1$, separated by a valley between $0.08 - 0.2$. The maximum amplitude of the power spectrum in the low-frequency region occurs at $St_L = 0.04$ and its value normalized by the wall pressure is about 0.35×10^{-3}. Upon forcing, the amplitude of pressure fluctuations in the range of frequencies between $St_L = 0.04 - 0.8$ clearly decreases. The maximum decrease in amplitude in the low frequency region occurs at about $St_L = 0.06$. The average amplitude of pressure fluctuations between $St_L = 0.04 - 0.08$ has decreased from 0.3×10^{-3} to 0.22×10^{-3}. Figure 6.4(b) also shows that with forcing, there is an increase in amplitude of fluctuations in the Strouhal number range of $St_L = 0.01 - 0.03$, with maximum increase at $St_L = 0.02$ from 0.22×10^{-3} without forcing to 0.3×10^{-3}. This increase in amplitude of pressure fluctuations at such low frequencies due to forcing is counter to the desired effect of forcing. However it should be noted that the absolute magnitude of fractional increase in pressure fluctuations around $St_L = 0.02$ is 0.08×10^{-3}, which is 3 times smaller than the decrease in the amplitude of pressure fluctuations achieved in the intermittent region with forcing. Overall, at the location of $x/L = 0.66$, forcing shifts the frequency of peak pressure fluctuations to a lower value - the peak amplitude occurs at $St_L = 0.02$ with forcing, whereas the peak amplitude in the low frequency band without forcing occurs at $St_L = 0.04$.

Figure 6.4(c) shows the case where pressure measurements were made at the compression corner ($x/L = 0$). In this case, the unforced-case pressure fluctuations are shifted to still higher frequencies. The unforced spectrum continuously increases till $St_L = 0.1$ and stays constant till $St_L = 0.5$. Beyond $St_L = 1$ the frequency response of the pressure transducer limits the accuracy of the measurements. The maximum amplitude of the pressure fluctuations normalized by the square of the

mean wall pressure is about 0.35×10^{-3} and it occurs at $St_L \approx 1$. With forcing the power spectrum looks very similar to the unforced case. There are no noticeable changes in the amplitude of the spectrum at low frequencies. Considering the spectral features induced by EM noise, the effect of forcing at high frequencies could not be ascertained within the experimental uncertainty at the high frequency region ($St_L > 1$). Nevertheless, these results seem to show that the effect of upstream forcing is not felt close to the compression corner.

An interesting case emerges when the pressure fluctuations were measured at $x/L = 0.86$, which is in between the intermittent region and $x/L = 0.66$. This measurement location is notable for the effect of forcing that is not observed. The power spectrum at $x/L = 0.86$, with and without forcing, is shown in fig 6.4(d). The pressure fluctuations without forcing exhibit a continuously increasing amplitude till $St_L = 0.1$. The low frequency peak that was dominant at $x/L = 0.95$ does not make a dominant contribution to the total fluctuations at this location. Instead, the pressure fluctuations are dominated by high frequency fluctuations. The maximum power spectral density normalized by the square of the wall pressure is 3×10^{-4}. Interestingly, the power spectrum does not change with forcing. The magnitude of the fluctuations, and the trend with increasing frequency, remain the same with forcing. Thus, it is seen that forcing does not seem to affect the fluctuations at $x/L = 0.86$ even though significant modifications were observed at surrounding locations. The influence of forcing on the separation bubble pressure fluctuations brings up two interesting questions:

1. What is the physical mechanism that leads to the suppression of pressure fluctuations in the intermittent region and the shift of the dominant frequency to lower value at $x/L = 0.66$?

2. Why is the effect of forcing observed at $x/L = 1$ and 0.66, but not at $x/L = 0.86$ and 0?

These two questions will be addressed in the following paragraphs. Figure 6.2 (b) clearly shows that the forced separation shock motion executes periodic oscillations at the pulsing frequency. In other words, the energy content in the broadband frequencies of the unforced shock is transferred to the pulsing frequency when the shock is forced. This would account for the decrease in the amplitude of the broadband low frequency seen in the intermittent region (fig. 6.6 (a)).

To investigate reason for the shift of power spectral peak to lower frequencies observed at $x/L = 0.66$, wall pressure fluctuation measurements were obtained at several downstream locations under the SWBLI of an unforced 24° compression corner placed in the Mach 3 flow. The spatial evolution of the power spectra along the SWBLI region is shown in figure 6.6(a) - (e). The dominant Strouhal number at each location was identified as the peak in the dominant broadband feature, and the spatial variation of this dominant Strouhal number is shown in figure 6.6 (f). The plot shows that the dominant Strouhal number peaks at $x/L = 0.8$, which is just downstream of the intermittent region. Downstream of this location, the dominant Strouhal number decreases significantly. This is especially the case between $0.2 < x/L < 0.8$. It was pointed out earlier that the separation shock spends about 70% of its time upstream of its unforced mean location with pulsed-plasma jet injection. It is possible that the modified pressure spectrum with forcing is because of the increased average distance of the separation shock from the transducer due to the average upstream shift of the separation shock. This is illustrated in the schematic shown in figure 6.5. It is therefore quite possible that forcing causes a shift to a lower dominant frequency at $x/L = 0.66$ because the mean location of the separation shock is farther upstream

and so the transducer is in a region of lower dominant frequency.

To understand why forcing does not seem to affect the pressure fluctuations at $x/L = 0.86$, it is instructive to study the organization of the separation bubble, i.e., how the pressure fluctuations inside the separation bubble are correlated with those in the intermittent region. Figure 6.7 shows the coherence of the wall pressure fluctuations between $x/L = 0.8$ and $x/L = 1$, and $x/L = 0.6$ and $x/L = 1$. The location where $x/L = 1$ is under the intermittent region. Coherence spectra show the linearity of two fluctuating signals as a function of frequency. A coherence of unity signifies a linearly coupled system and values less than unity signifies the degree of non-linearity, with a value of 0 signifying an uncoupled system. For the present case, the frequencies of interest are those of the low frequency unsteadiness of the separation shock motion ($St_L \approx 0.01 - 0.03$). The coherence between pressures under the intermittent region ($x/L = 1$) and $x/L = 0.8$ (in the relevant Strouhal number range) is about 0.05, which shows significant non-linearity between $x/L = 1$ and $x/L = 0.8$. Hence a perturbation in pressure in the intermittent region does not create a corresponding fluctuation in pressure at $x/L = 0.8$. This could be a reason why the power spectrum is not affected by forcing. The corresponding value of coherence between $x/L = 1$ and $x/L = 0.6$ is about 0.3, which signifies considerably higher linearity between the signals. Hence, with forcing the separation shock motion causes modifications to the pressure fluctuations in the intermittent region. This in turn causes the corresponding modifications in the fluctuations at $x/L = 0.66$, as seen in fig 6.4(b).

6.2.2 Effect of pulsing frequency on the SWBLI unsteadiness

From the previous section, it is clear that the effect of the pulsed-plasma jet injection can be detected in the intermittent region as well as inside the SWBLI region. A study was made to assess the effect of changing the pulsing frequency on the SWBLI unsteadiness. Three pulsing frequencies, 2 kHz, 3 kHz and4 kHz, which corresponds to $St_L = 0.04$, 0.06 and 0.08, respectively, were tested. The lowest frequency lies close to the peak of the low frequency unsteadiness of the SWBLI mentioned earlier ($St_L = 0.02-0.05$). The higher frequencies lie away from the peak of the low frequency unsteadiness of the SWBLI. It should be mentioned that the corresponding amplitude of the unsteadiness at these higher frequencies is about a third of the peak amplitude. Due to the limitations in the cavity recharging time, frequencies of pulsing higher than 5 kHz could not be achieved. Similar to the previous sections, a qualitative study of the interaction was made using 10 kHz schlieren imaging and a quantitative study was made using wall-pressure fluctuation measurements. It should be noted that there is a small difference in the experimental settings between the schlieren imaging and wall-pressure fluctuation measurements. While schlieren imaging was performed with an array of three plasma jets operated at a fixed duty cycle of 10% for all pulsing frequencies, the wall pressure fluctuations were performed with a single plasma jet operated for a fixed pulse duration of $20\,\mu s$ per pulse. Figure 6.8 shows a schlieren image sequence of the interaction between the pulsed-plasma jet and the SWBLI during one pulse cycle. The plasma jet was pulsed at 3.3 kHz and operated for a duration of $30\,\mu s$ per cycle. Each sub-figure is separated by $100\,\mu s$. The location of the mean unforced shock is marked as a white line. It can be seen that the separation shock responds to the plasma jet pulses by moving upstream. This response of the shock is qualitatively identical to that with 2 kHz pulsing seen in fig. 6.1. However,

the amplitude of upstream motion of the separation shock in the present case is reduced when compared to that with 2 kHz pulsing, shown in fig. 6.8. A similar tracking of the separation shock, as performed in fig. 6.2 and 6.3, was also made in order to study the motion of the separation shock in detail (figure not shown). The periodic motion of the separation shock with pulsed-plasma jet forcing was evident. An interesting feature of the separation shock recovery motion was that the average velocity of the shock recovery motion was close to 2% U_∞, which is the velocity that was observed even for the plasma jet pulsed at 2 kHz.

Wall pressure measurements were made to study the response of the SWBLI to the plasma jet pulsed at different frequencies. Attempts were made to make the wall pressure fluctuation measurements in the intermittent region in order to capture the impact of different pulsing frequencies on the low frequency unsteadiness of the SWBLI directly. However, with increased pulsing frequency, significantly higher instances of direct discharge between the anode of the actuator and the pulsed ground were observed. Hence, the efforts to make this measurement were abandoned. Instead, wall pressure fluctuation measurements were made inside the SWBLI region at the location $x/L = 0.66$ for different plasma jet pulsing frequencies. It was shown in the previous section that the effect of the pulsed-plasma jet on the intermittent region was also seen at $x/L = 0.66$ because of considerable coherence in the pressure fluctuations between the intermittent region and at $x/L = 0.66$. Hence, for this experiment, the impact of the plasma jet on the low frequency unsteadiness of the SWBLI were inferred from the wall pressure fluctuation measurements made at $x/L = 0.66$. Figure 6.9 shows the power spectrum of the wall pressure fluctuations with plasma jet pulsing frequencies of 3 and 4 kHz. The power spectra of the unforced case and forced case (plasma-jet pulsed at 2 kHz), are also shown for comparison. It can be

seen that the power spectra of the wall pressure fluctuations are modified from the unforced case even with pulsing frequencies of 3 and 4 kHz. In fact, the modifications of the power spectra with 3 and 4 kHz forcing are very similar to those caused by 2 kHz forcing. The amplitudes of the fluctuations at $St_L > 0.03$ was significantly reduced, whereas the fluctuations in the range $St_L = 0.01 - 0.03$ were increased. The extent of reduction at $St_L > 0.03$ and the amplification between $St_L = 0.01 - 0.03$ was identical at all frequencies between 2 kHz and 4 kHz. Hence, it can be concluded from the wall pressure fluctuation measurements that the SWBLI was modified in a similar manner quantitatively and qualitatively at different pulsing frequencies. This is in contrast to the schlieren movies at different pulsing frequencies (figs. 6.1 and 6.8) where a reduction in response of the separation shock was observed with increasing frequencies. It should be noted that the duration of the operation of the plasma jet was fixed at 20 μs for all frequencies while making the wall pressure fluctuation measurements. This is in contrast with the settings of the schlieren imaging, where the duty cycle was fixed by changing plasma pulse duration. Hence, it can be concluded that the duration of the jet pulse has a bigger impact on the SWBLI unsteadiness than the pulsing frequency itself, for the range of frequencies tested in this study.

It appears paradoxical that the increase in pulsing frequency, keeping the pulse-duration fixed, does not impact the power spectrum. The reason behind the paradox is that, assuming the same recovery shock velocity, the separation shock recovers to smaller distances with increasing pulsing frequency. Hence, the mean separation shock location becomes increasingly upstream with increasing frequency. In other words, the transducer is at an increasingly downstream location with respect to the separation shock with increasing frequency. It was seen from fig. 6.6(f) that the dominant frequency of the power spectra decreases with increasing downstream

distances from the separation shock. However, in the present case, the dominant frequency is approximately the same for all the pulsing frequencies. This implies that the effectiveness of the pulsed-plasma jet decreases with increasing pulsing frequency. The exact reason behind this is not completely understood. However, some of the possible reasons are discussed here. With increasing pulsing frequency, the density of the pulsed-plasma jet decreases because of increased mean cavity temperature. Since the jet exit velocity remains unaltered with increasing frequency, the momentum (and hence the strength) of the plasma jet decreases with increasing pulsing frequency. This might cause less of separation shock actuation with increasing frequency. Another possibility is that the higher pulsing frequency is away from the "natural frequency" of the low frequency unsteadiness of the separation bubble. For example, if we model the separation bubble dynamics as a mass-spring-damper system whose resonance is in the low frequency unsteadiness range, the higher pulsing frequency corresponds to the range that is away from resonance. Hence, substantially higher amplitude is required when forcing at this frequency to cause the same actuation as would be required at resonance.

6.3 Effect of forcing location

A detailed study was made to assess the effect of location of forcing on the separation shock unsteadiness. Three different locations: $x = 6\,\delta$, $1.7\,\delta$ and $0\,\delta$ upstream of the compression corner were tested. While the $x = 6\,\delta$ injection case corresponds to the location upstream of the separation shock, $x = 1.7\,\delta$ and $0\,\delta$ correspond to locations inside the SWBLI interaction region. The $x = 6\delta$ injection case has been presented in detail in the previous sections and will not be repeated here. For the $x = 1.7\delta$ and 0δ injection cases, arrays of three pulsed-plasma jets pitched at varying

angles between -30° and 30° were employed. For these downstream injection experiments, the jets were not skewed.

First, the response of the separation shock to the pulsed-plasma jet injected at different locations is compared using $10\,kHz$ schlieren imaging. Figure 6.10 shows instantaneous images of the interaction between the separation shock with the pulsed-plasma jet injected at different locations. The pitch angle of the downstream injection case is -30° (i.e., 30° counter to the upstream flow direction). The images correspond to the maximum upstream shock displacement that was observed. The corresponding mean shock location for the unforced case is also indicated by a dotted line. In all the cases, the pulsed-plasma jet can be clearly seen in the schlieren images and the phase-averaged boundary of the plasma-jet seen from the schlieren images is also marked in the images. The phase-averaged boundary of the plasma jet was obtained by subtracting the phase-averaged schlieren image of the forced case from an average schlieren image of the unforced case. For the case of upstream injection, most of the jet seems to extend along the outer boundary of the separation bubble without penetrating into the bulk of the bubble. This observation is supported by the plasma luminosity image shown in fig. 5.5 of chapter 5, where the luminous region corresponds to the pulsed-plasma jet. For the case of injection from inside the separation bubble, the phase-averaged boundary of the pulsed-plasma jet at the instant of maximum upstream separation shock motion is shown in fig. 6.10 (b) and (c). It can be seen that the pulsed-plasma jet penetrates upstream through the bulk of the separation bubble before it is convected by the upstream flow. Thus, with injection from inside the separation bubble, the pulsed-plasma jet should cause considerable changes to the thermodynamic conditions within the separation bubble, e.g., a change in the speed of sound owing to the introduction of hot gases. In order to appreciate the

magnitude of the disturbance caused by the pulsed-plasma jet, the peak momentum ratio of the pulsed-plasma jet to the freestream was estimated to be about 0.6 as shown in chapter 5 and the exit velocity of the jet is about $0.5U_\infty$.

Figure 6.10 shows that upstream injection causes significant upstream displacement of the separation shock, whereas injection from inside the separation bubble causes much less separation shock movement. The same result was also observed when the pitch angle was changed from -30° to 0° (normal injection) and 30° (i.e., 30° along the upstream flow direction).

The specific case of injection located $1.7\,\delta$ from the compression corner ($x/L \approx 0.5$) was also studied by using wall pressure measurements. The pitch angle was varied between -30° to +30°. The wall pressure measurement was made inside the intermittent region at $x/L = 1$ for all cases. Note that the normalizing length scale has been changed to interaction length ($L \approx 3.5\delta$) for the pressure measurements has changed in order to be consistent with the previous literature on the pressure fluctuations in SWBLI region. Figure 6.11 shows the power spectra, normalized by the square of mean pressure, of the wall pressure fluctuations with and without pulsed-plasma jet injection. The pitch angle of the plasma jet was $-30°$. The spectra of both the forced and unforced cases contain a few spikes at discrete frequencies due to structural vibration and EM noise as marked in the figure. As argued for the upstream injection cases, no quantitative inferences are drawn at any frequency coinciding with a spike and the objective is to understand the overall effect of the pulsed-plasma jet injection. It can be seen that the spectra with and without injection are identical to one another but for the spikes due to EM noise. This indicates that the pulsed-plasma jet injected inside the separation bubble does not cause any noticeable change to the separation shock motion. Similar results were also obtained for the case with injection

at the compression ramp corner ($x/L = 0$). Similar results were also obtained by varying the pitch angle of injection from -30° to 30° at both downstream injection locations ($x/L = 0.5$ and 0). These results clearly indicate that the injection from inside the separation bubble has negligible impact on the low frequency motion of the separation bubble. Thus, it is inferred that disturbances of a given amplitude, when injected from upstream of the separation shock, cause significantly larger changes in the separation shock motion than injection from within the separation bubble.

6.4 Analysis of separation shock actuation mechanism

From the above sections, it is clear that pulsed-plasma jet injection from upstream of the separation shock causes the maximum perturbation to the separation shock. A detailed analysis of the separation shock actuation mechanism by the pulsed-plasma jet injected from upstream was made using phase-locked schlieren imaging at different time delays and particle image velocimetry. In this study, the response of the separation shock to the pulsed-plasma jet is investigated qualitatively. The initial phase of interaction is the time during which there is a direct interaction between the pulsed-plasma jet with the separation shock. This phase happens between 40 to 100 μs from the start of discharge trigger. The recovery phase corresponds to the bulk downstream motion of the separation shock as observed in the 10 kHz schlieren movies discussed earlier (e.g. fig. 6.1). This happens roughly between 100 to 500 μs from the start of discharge trigger.

6.4.1 Initial phase of interaction

The initial phase of interaction is characterized by those times when there is a direct interaction between the pulsed-plasma jet and the separation shock. This

happens during the time delays between 40 to 100μs after the start of discharge trigger. The initial interaction between the pulsed-plasma jet with the separation shock was studied using phase-averaged schlieren imaging done at 60 Hz. An array of three pulsed-plasma jets, pitched at 45° and skewed at 90°, was employed. The discharge current of each pulsed-plasma jet was set at 4.5 A and its pulse duration was set at 20 μs. The plasma jet was injected from about 4δ upstream of the compression corner (about 2δ upstream of the separation shock). The discharge was pulsed at 60 Hz. The separation shock was generated using an one inch wide 30° compression corner and the separation shock was located 2δ upstream of the compression corner. The time resolution of this phase-average schlieren imaging was 5μs, which was short enough to make a detailed study of the separation shock motion during the initial phase of the interaction.

Figure 6.12 shows the average schlieren image of the flowfield without the pulsed-plasma jet and phase-locked schlieren images with the pulsed-plasma jet after 45 and 60μs from the start of the discharge trigger. From the figures, it can be discerned that the separation shock exhibits two characteristic features during the initial phase of the interaction. At the start of the interaction, when the plasma-jet is just incident on the separation shock, the portion of the separation shock close to the floor bulges upstream. This can be seen in fig. 6.12 (b), which was taken when the pulsed-plasma jet just entered the separation shock. At later times, as the pulsed-plasma jet propagates through the SWBLI region, the separation shock gets progressively 'bulged out'. This feature is seen in fig. 6.12 (c), where a higher location along the shock length is bulged out when compared to fig. 6.12 (b).

The upstream bulging of the separation shock close to the foot, similar to the one seen in fig 6.12 (b), was also observed with a low density perturbation by Shin

et al. (2008). They used a surface mounted DC glow discharge source upstream of the separation shock to cause local heat addition to the incoming flow, which creates a low density perturbation. Figure 6.13 shows the comparison of the response of the separation shock to the incoming low density perturbation with the undisturbed case obtained by Shin et al. (2008) (fig. 6.13 (a) and 6.13 (b)) and the present case (fig. 6.13 (c) and 6.13 (d)). The location of the anode and cathode are marked by 'A' and 'C' respectively in fig. 6.13 (a) and (b). The red lines shown in fig. 6.13 (a) and (b) mark the heights of the separation shock at the given locations, and this detail is irrelevant for the present discussion. It can be seen that the structure of the separation shock as observed from schlieren imaging gets modified in the same manner in both cases. Hence, it is proposed that the initial upstream bulge of the separation shock, close to its foot, is because of the low density of the pulsed-plasma jet, which causes a sudden decrease in incoming Mach number. The separation shock responds to the smaller Mach number by shifting upstream. This is not surprising, as it is well known that the standoff distance of the shock increases with decreasing freestream Mach number.

To understand how the propagation of the pulsed-plasma jet could cause a "bulge" at different portions of the separation shock, a simple quasi-steady model is proposed. Let us consider a case without separation bubble, which makes the analysis simpler. The absence of the separation bubble results in an attached shock for turning angles less than the inviscid limit. An illustration of this model is shown in figure 6.14, where fig. 6.14 (a) shows the flowfield without plasma-jet and fig. 6.14 (b) shows the flowfield with plasma-jet injection.

Consider a region, as shown in fig. 6.14 (a) and (b), which covers a portion of the upstream boundary layer and a portion of the region downstream of the separation

shock. Let the boundary marked '1' be located upstream of the plasma-jet orifice so that the mass flux across the boundary '1' is same for both fig. 6.14 (a) and (b). The mass flux across the boundary '1' is denoted by $\dot{m}_1$. Let the boundary marked '2' and '3' be located sufficiently above the floor for both the cases. Also, let the boundary '2' and '3' be parallel to the streamline of the no plasma-jet case and plasma-jet injection case (fig. 6.14 (a) and (b)), so that there is no mass flux across boundary '2' and '3'. Let 'h_B' denote the height of the boundary '3' for both cases, as shown in the figure. Let the mass flux through the boundary marked '4' be denoted as $\dot{m}_{4A}$ for no plasma-jet case (fig. 6.14 (a)) and as $\dot{m}_{4B}$ for plasma-jet injection case. Let the boundary marked 'A' coincide with the floor. Let the density of the flow downstream of the shock be denoted by ρ_{2A} for the no plasma-jet case and ρ_{2B} for plasma-jet injection case respectively.

Applying the conservation of mass for the no plasma-jet case, the mass flux entering boundary '1' is equal to the mass flux exiting through boundary '4', i.e.,

$$\dot{m}_{4A} = \dot{m}_1 = \int_0^{h_B} \rho_{2A} u_{2A} dy \tag{6.1}$$

Now let us consider the application of the mass conservation for the situation where plasma-jet is injected. For this analysis, a steady plasma-jet is considered, as shown in fig. 6.14(b). The plasma-jet, by definition, is a low density and a low momentum perturbation. Let $\dot{m}_{pl}$ and ρ_{pl} denote the mass flux of the plasma jet and the density of the plasma-jet downstream of the shock due to compression corner. Let h_{pl} denote the vertical extent of the plasma-jet while it crosses the boundary '4'. Now applying conservation of mass to the plasma-jet injection case,

$$\dot{m}_{4B} = \dot{m}_{pl} + \dot{m}_1 = \int_0^{h_{pl}} \rho_{pl} u_{2B} dy \; + \int_{h_{pl}}^{h_B} \rho_{2B} u_{2B} dy \tag{6.2}$$

From the right-hand side of the equations 6.1 and 6.2, it can be seen that the mass flux $\dot{m}_1$ is confined within the height 'h_B' for no plasma-jet case, whereas $\dot{m}_1$ is confined within '$h_B - h_{pl}$' for the plasma-jet injection case. This shows that there is an increased compression with the plasma-jet injection case. This increased compresion means an increased shock angle in the region above the plasma-jet region.

6.4.2 Recovery phase of interaction

The recovery phase of the interaction was studied using phase-averaged schlieren imaging at $10\,kHz$ and particle image velocimetry at 10 Hz. An array of three pulsed-plasma jet pitched at 45° and skewed at 90° was employed. The discharge current of each pulsed-plasma jet was set at $2\,A$. The pulse width of the pulsed-plasma jet was set at $50\,\mu s$ and the discharge was pulsed at $2\,kHz$. The plasma jet was injected 6δ upstream of the compression corner (about 3δ upstream of the separation shock). The SWBLI was generated using a 24° compression corner, 1.5 inches wide and the separation shock was located 3δ in front of the compression corner. The time resolution of this phase-average schlieren imaging was $100\,\mu s$. This was short enough to make a detailed study of the separation shock motion during the recovery phase of the interaction.

It should be mentioned that the pulsed-plasma jet current and its pulse width are different for the studies on the initial phase and the recovery phase of the interaction. However, this part of the study focuses on the upstream motion and the recovery of the separation shock only. It was noted in the previous chapter 5 that there were

no qualitative changes in the interaction with changing discharge current and pulse duration. The separation shock was pushed upstream and was allowed to recover to its unforced position in all the pulsed-plasma jet configurations. However, the extent to which the separation shock is pushed upstream and the time scale of recovery does change with discharge current and pulse duration. Since the general theme of this section is to explain the mechanism of the interaction between the pulsed-plasma jet and the separation shock, only the qualitative details, which are independent of the discharge properties are considered, and the quantitative details of the interaction are ignored.

Figure 6.15 shows the phase-averaged schlieren images taken at 125, 225, 325 and 425 μs. About 180 pulse cycles were included to compute the phase-average image at each time delay. During this time period, the pulsed-plasma jet should have propagated through the SWBLI region, and thus there is no direct interaction between the pulsed-plasma jet and the separation shock. This time period simply corresponds to the recovery phase of the separation shock (i.e., the bulk downstream shock motion). In each figure, a linear extrapolation of the separation shock was made to the floor of the test section (shown as black dashed line) to mark the approximate shock foot location. In figures 6.15(b), (c) and (d) the separation shock locations in the previous frame are marked as white dashed line. It can be seen in figure 6.15 (d) that the separation shock is roughly at the same location as it was in figure 6.15(c); hence the time scale of recovery of the separation estimated from these images is about 400 μs. It should be noted that this gradual recovery of the separation shock was discussed in detail in previous sections using instantaneous images. Figure 6.15 shows the downstream shock motion is present even in the phase-average images.

To understand the mechanism that drives this bulk downstream shock mo-

tion, particle image velocimetry was performed in the streamwise plane to obtain the flowfield at different time delays between 100 and 200 μs from the start of the discharge trigger. The imaging plane was approximately at the spanwise centerline of the pulsed-plasma jet. The information about the trajectory of the pulsed-plasma jet was obtained from plan-view PLS imaging. A single pulsed-plasma jet was employed for this experiment. The discharge current was set at 2 A and the pulse duration was set at $50\mu s$. About 50 vector fields were averaged to obtain the phase-average velocity field at each time delay. Figure 6.16 shows the mean streamwise (U) velocity contours of the flowfield of the unforced case and forced case at different time delays. The colormap was adjusted to emphasize the extent of the separation bubble. Figure 6.16 (a) corresponds to the unforced case. It can be seen that there is no observable reverse velocity in the flowfield, which is most likely because the closest location to the floor where the velocity could be measured was about $\delta/4$. This limitation is because reflections of the laser sheet off the floor interfered with the particle images and made it impossible to compute accurate vectors in this region. Hence, the absence of reverse velocity in this measurement does not necessarily imply the absence of mean separation. Figures 6.16(b), (c) and (d) correspond to the time delays of 100, 125 and 150 μs after the start of discharge trigger, respectively. The region of reverse velocity can be clearly seen in all the figures. This unambiguously shows a mean separation (reversed flow) at these time delays. Hence, the separation bubble has expanded significantly with the passage of the pulsed-plasma jet. It can also be seen that the extent of the separation bubble is larger at 125 μs when compared to 100 and 150 μs, which indicates that the separation bubble grows with the passage of the pulsed-plasma jet and subsequently shrinks in size. It is known from previous shock boundary layer interaction studies that the separation shock responds to the large scale pulsations of the separation bubble whose time scales are much longer than

the incoming boundary layer fluctuations. It is proposed here that the pulsed-plasma jet induces such large scale pulsations in the separation bubble as inferred from the separation bubble size at different time instants. The slow downstream motion of the separation shock to its unforced position is a direct result of the long recovery time scale of the separation bubble.

The interaction between the plasma-jet and SWBLI can be summarized as follows:

- the separation shock undergoes an initial downstream shift due to the vortex generator action of the plasma jet
- the initial downstream shift is followed by an upstream shift, in response to the passage of the high temperature (low density) disturbance of the pulsed-plasma jet.
- the separation bubble increase in size as the pulsed-plasma jet propagates through the interaction.
- the separation bubble then recovers to its unperturbed state. The time scale of this pulsation is much longer than the time scale of the incoming boundary layer fluctuations. The separation shock is driven by the pulsations of the separation bubble as it is found in all SWBLI studies. The slow recovery of the separation bubble is likely the reason for the slow downstream motion of the separation shock after it is displaced upstream.

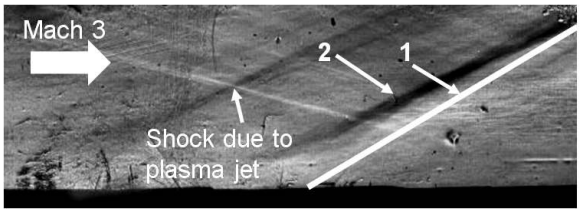

(a) 75 μs

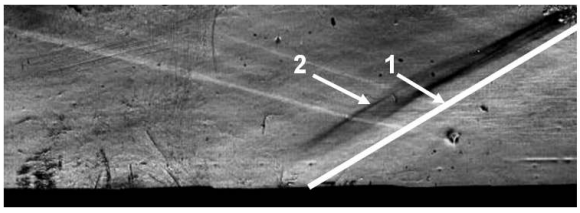

(b) 175μs

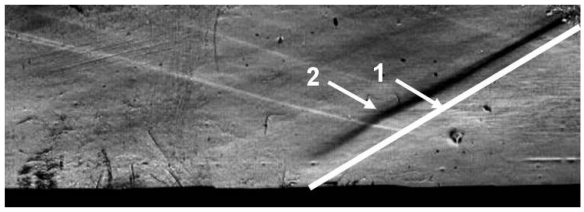

(c) 275 μs

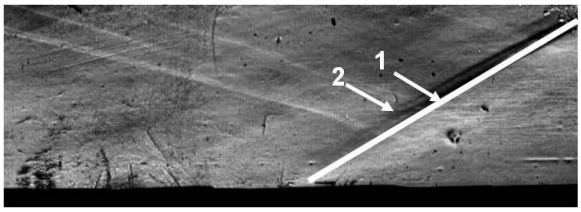

(d) 375 μs

Figure 6.1: 10 kHz framing rate schlieren movie sequence of the separation shock motion with pulsed-plasma jet actuation. Each frame is separated by 100 μs, starting from 75 μs after the start of the discharge trigger (frame (a)). Arrow (1) points to a line that indicates the mean shock position for the unforced case, and arrow (2) shows the location of the perturbed shock location. The plasma jet was pulsed at 2 kHz ($St_L = 0.04$).

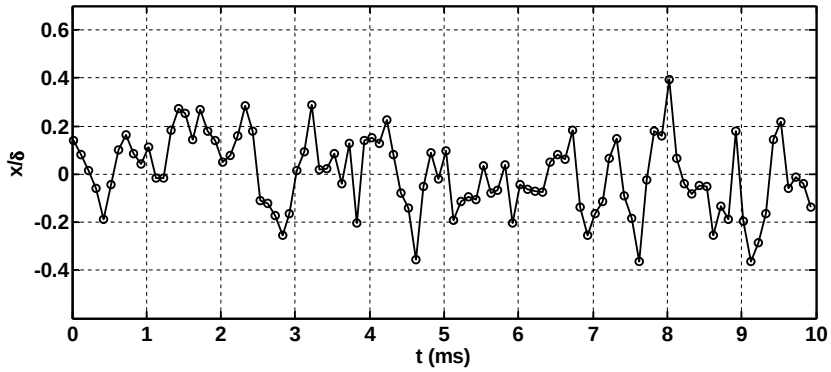

(a)

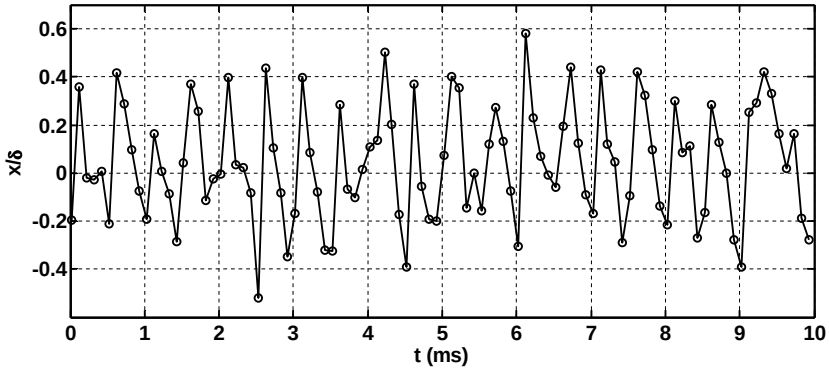

(b)

Figure 6.2: Sample time series separation shock motion obtained from schlieren images. The shock location corresponds to the average location between y = 0.5 – 0.7 δ. Fig. (a) represents the shock motion of the unforced case while (b) represents the shock motion with 2 kHz forcing. The mean unforced shock location is denoted by x/δ=0.

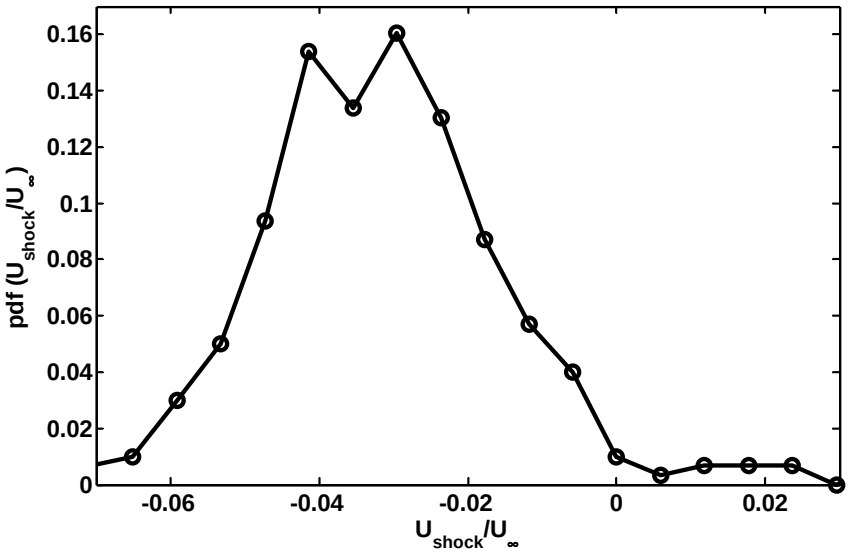

(a)

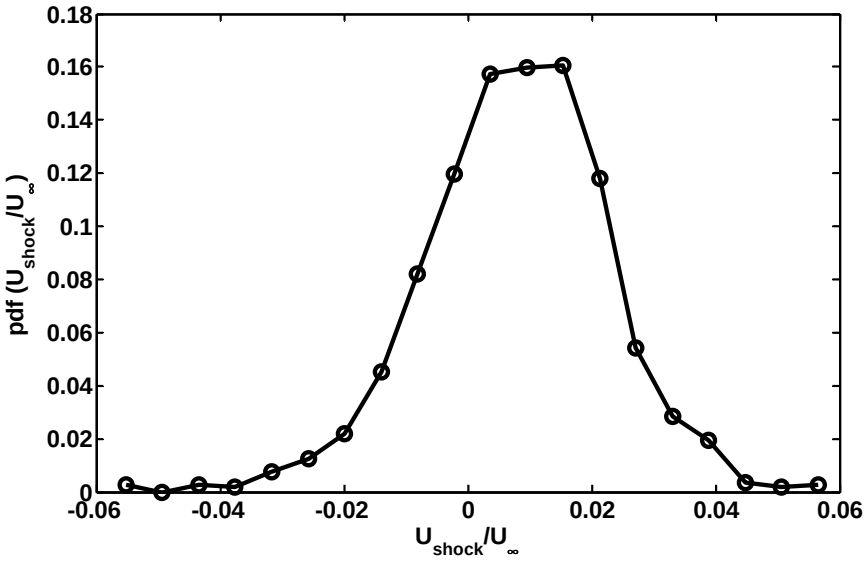

(b)

Figure 6.3: Probability density function of the separation shock velocity while it is being forced using a 2 kHz pulsed-plasma jet placed 6δ upstream of the compression corner. The separation shock locations are calculated from the schlieren movies. Figure (a) shows the pdf of the shock velocity immediately after the pulse and (b) shows the pdf of the shock velocity during its relaxation phase.

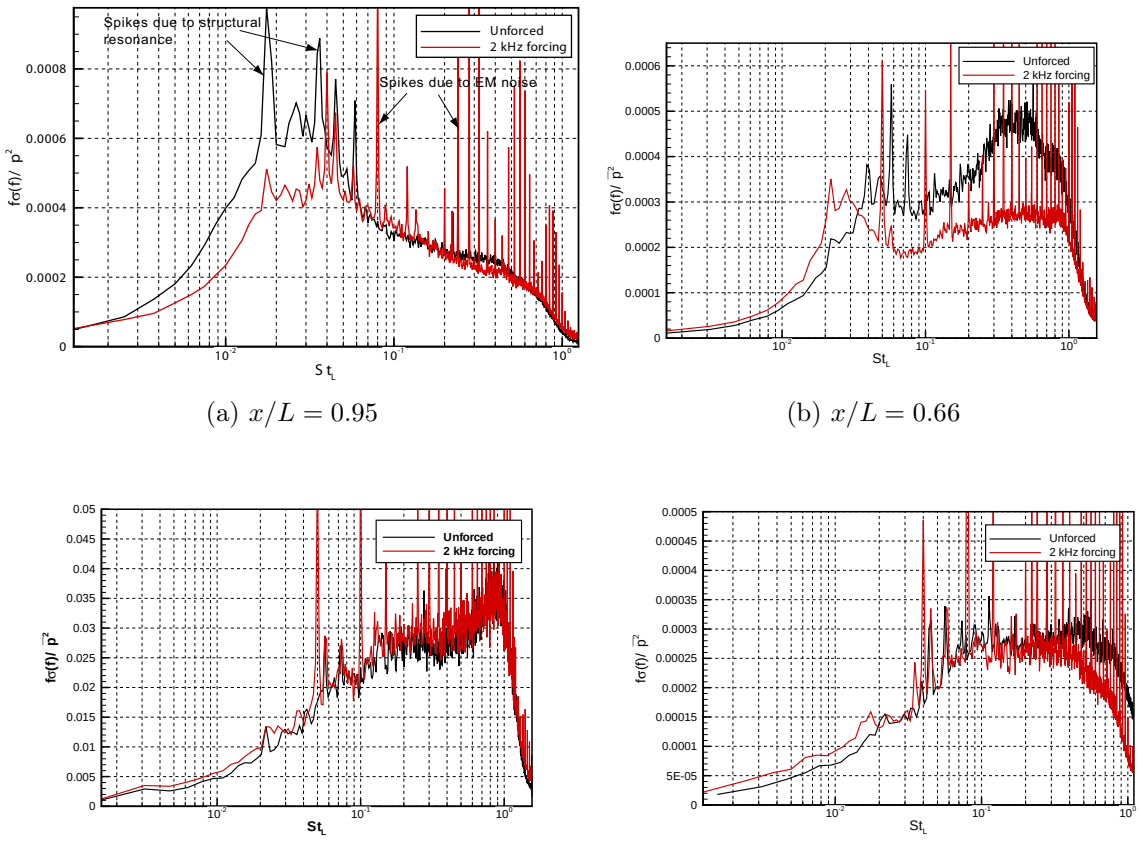

(a) $x/L = 0.95$

(b) $x/L = 0.66$

(c) $x/L = 0$

(d) $x/L = 0.86$

Figure 6.4: Comparison of the power spectra of the wall pressure underneath SWBLI region with and without forcing. (a) x/L $\approx$ 0.95 (intermittent region), (b) x/L = 0.66, (c) x/L = 0 and (d) x/L = 0.86. The pulsed-plasma jet is located at 6δ upstream of the compression corner in all the cases. The pulsing frequency was fixed at 2 kHz ($St_L = 0.04$) for all cases.

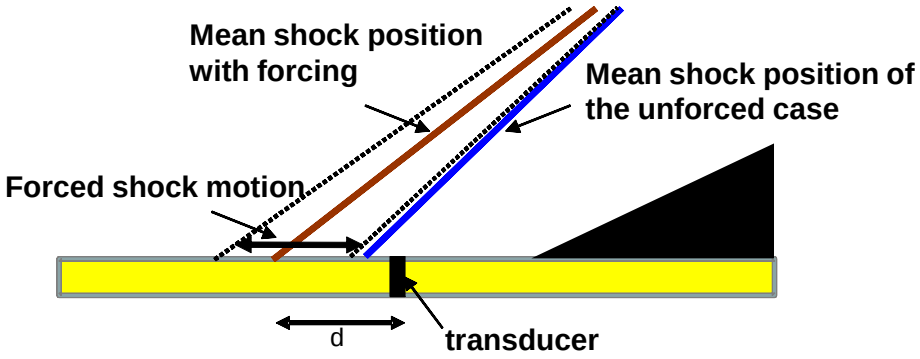

Figure 6.5: Schematic illustrating average downstream shift of the transducer relative to the separation shock when the shock is forcing used pulsed-plasma jets.

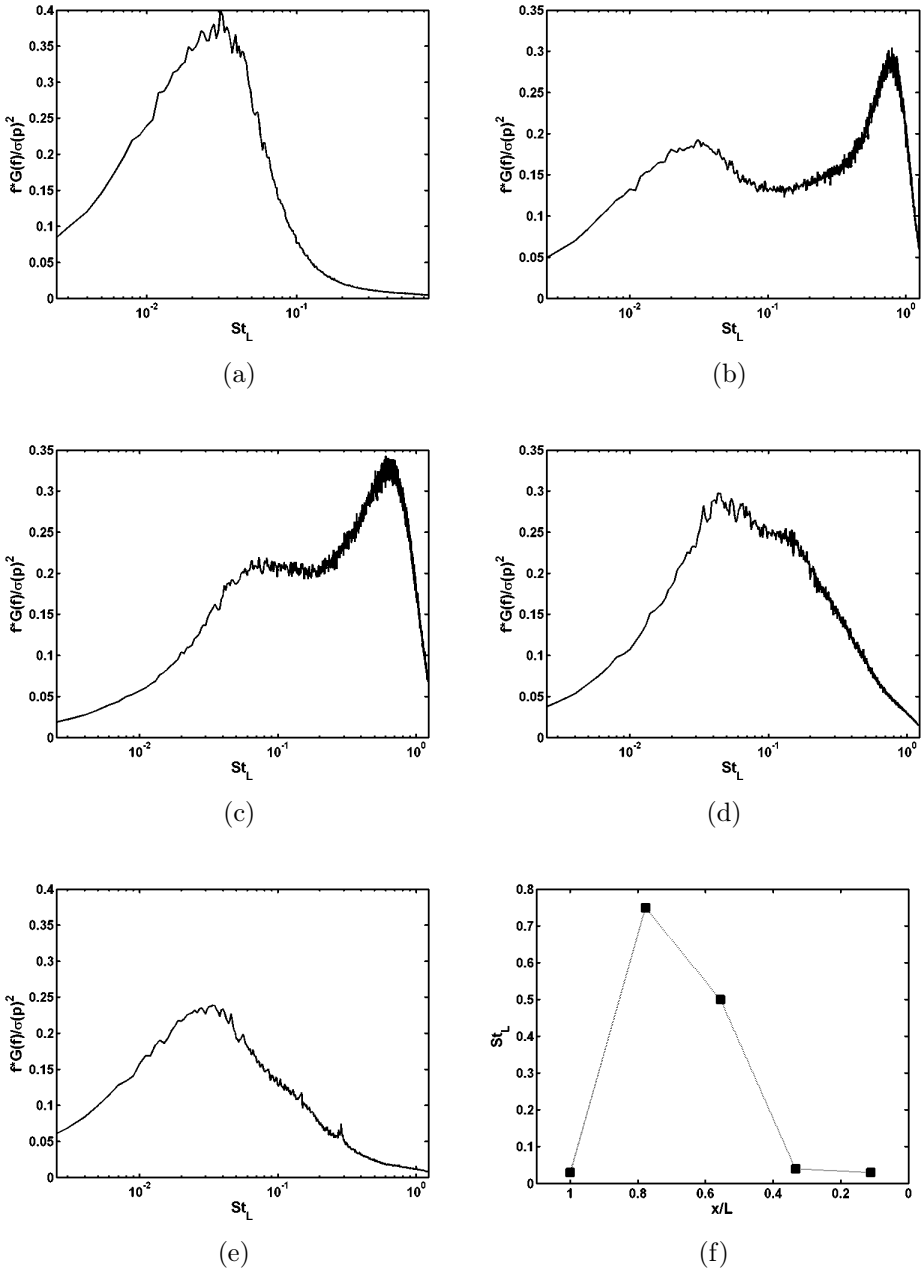

Figure 6.6: Evolution of power spectra of pressure fluctuations under an unforced SWBLI region. Figure (a) corresponds to $x/L = 1$, (b) $x/L = 0.77$, (c) $x/L = 0.55$, (d) $x/L = 0.33$, (e) $x/L = 0.11$, (f) evolution of St_L with the highest amplitude obtained from fig. (a) - (e).

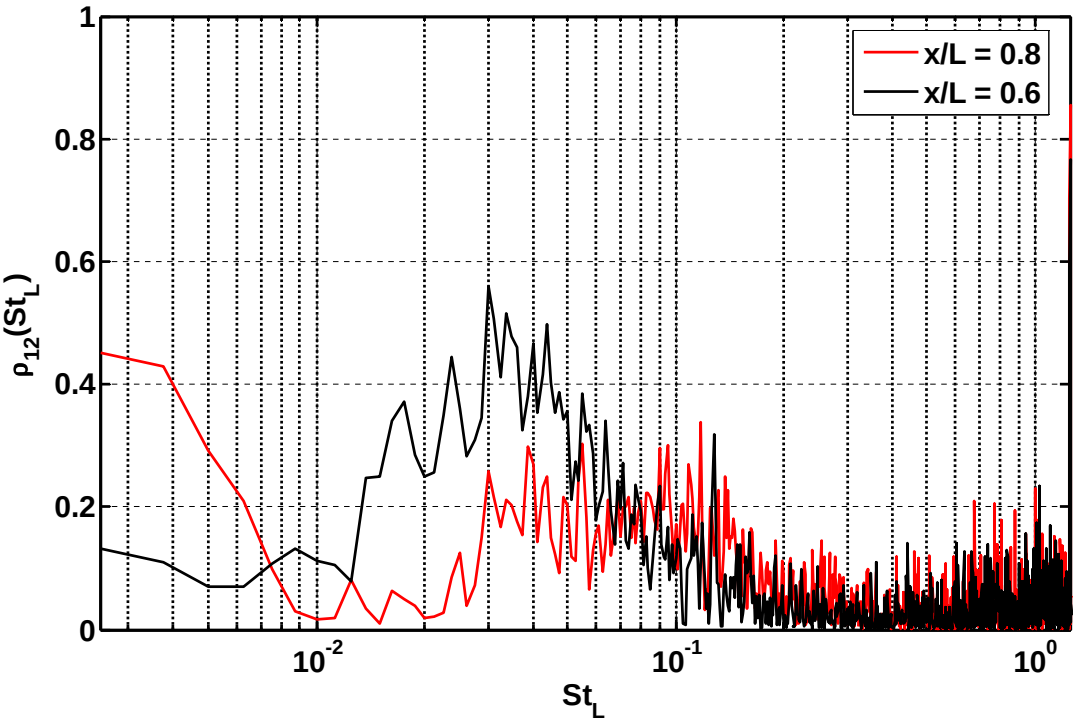

Figure 6.7: Coherence spectra of the wall pressure fluctuations between intermittent region and inside SWBLI region (x/L = 0.8 and 0.6).

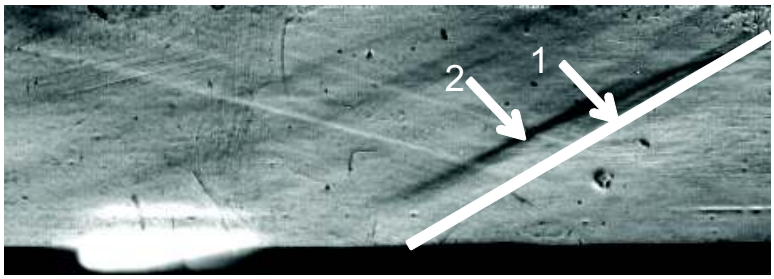

(a) 75 μs

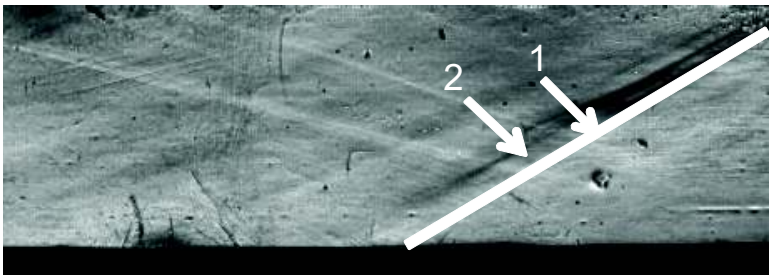

(b) 175 μs

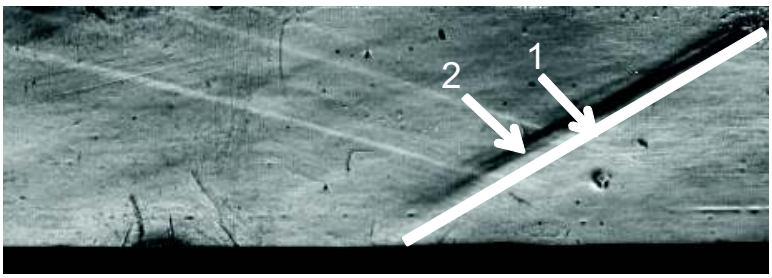

(c) 275 μs

Figure 6.8: 10 kHz framing rate schlieren movie sequence of the separation shock motion with pulsed-plasma jet actuation. Each frame is separated by 100 μs, starting from 75μs after the start of the discharge trigger (frame (a)). Arrow (1) points to a line that indicates the mean shock position for the unforced case, and arrow (2) shows the location of the perturbed shock location. The plasma jet was pulsed at 3.3 kHz ($St_L = 0.066$).

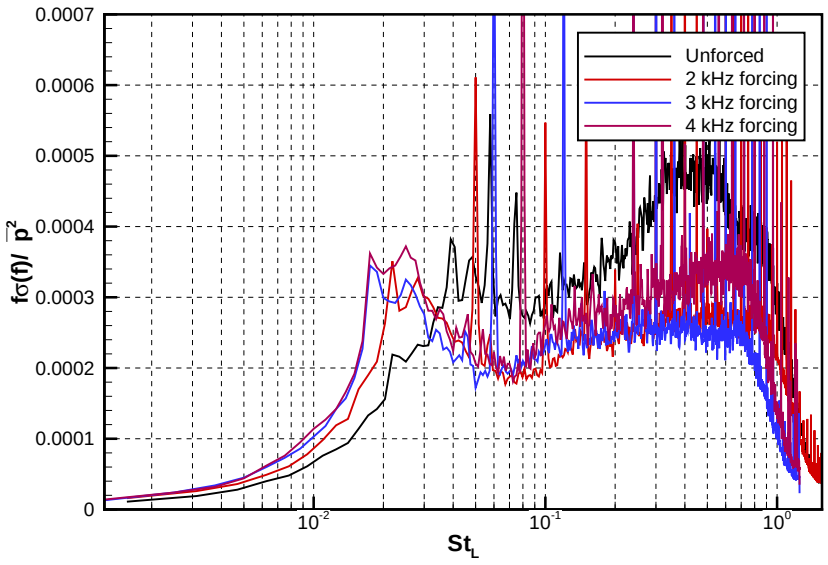

Figure 6.9: Comparison of the power spectra of the SWBLI unsteadiness at $x/L = 0.66$ forced at different frequencies. The discharge current was fixed at 3.9 A per jet and the pulse duration was fixed at 20 μs at all the forcing frequencies.

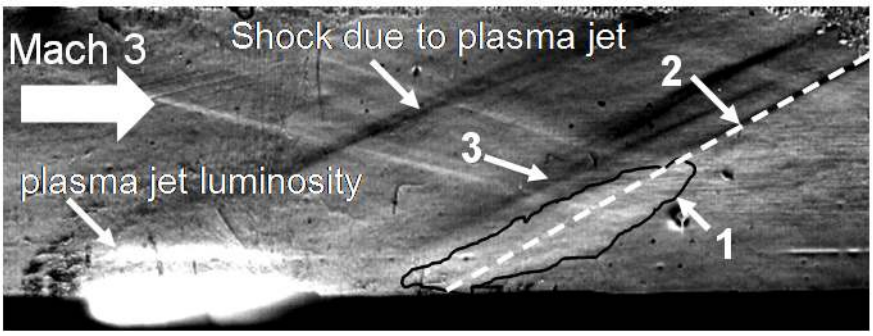

(a) 6δ

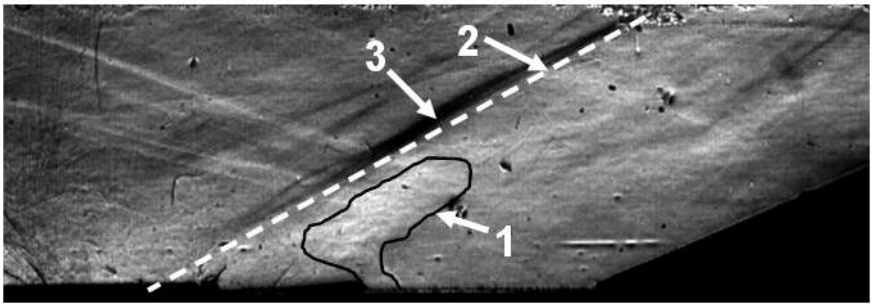

(b) 1.7δ

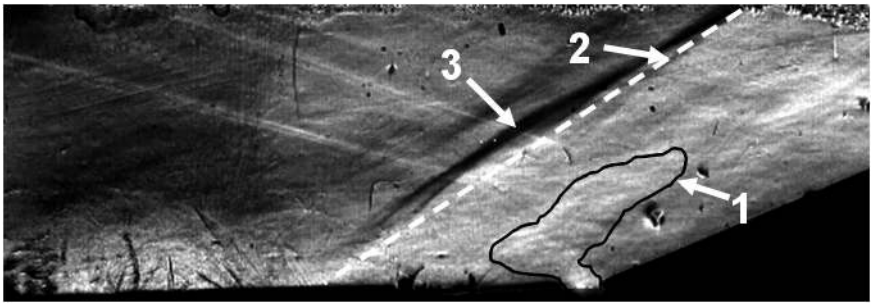

(c) 0δ

Figure 6.10: The effect of location of pulsed-plasma jet injection on the separation shock motion. Arrow "1" marks the approximate boundary of the pulsed-plasma jet injected. Arrow "2" shows the approximate mean location of the unforced separation shock and arrow "3" shows the separation shock forced by the pulsed-plasma jet. In figure (a) the jet is injected from 6δ, (b) the jet is injected from 0δ and (c) the jet is injected from 2δ upstream of the compression corner.

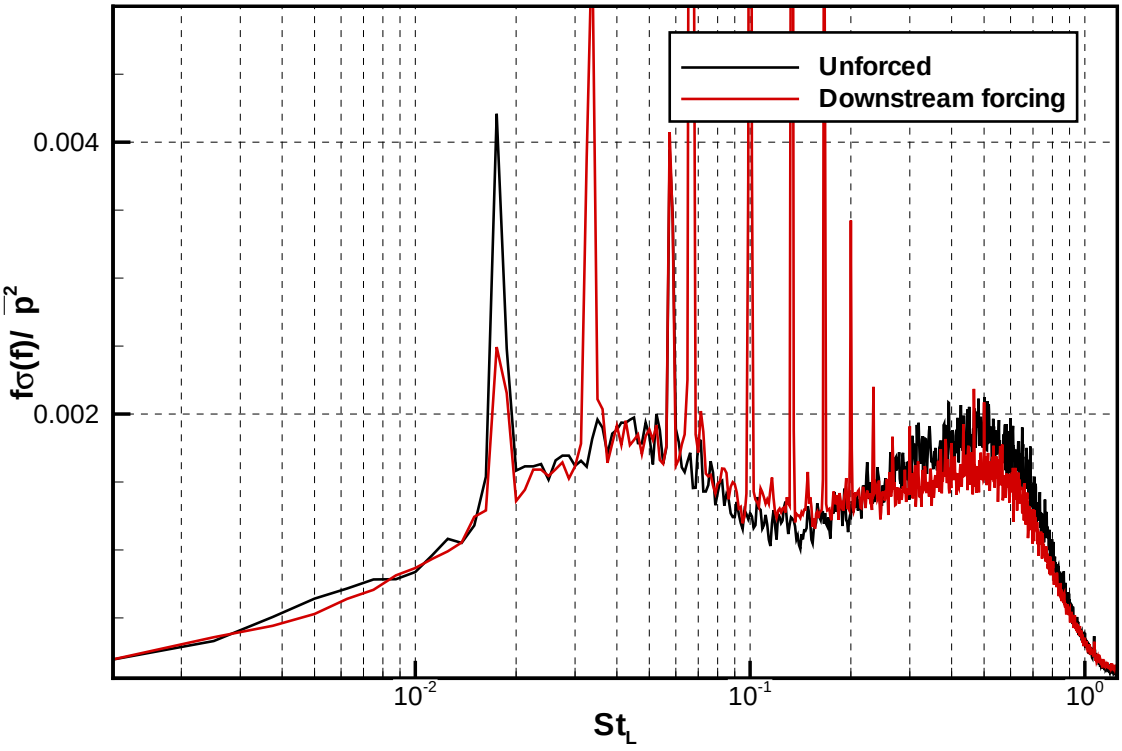

Figure 6.11: Power spectra at x/L = 1 of the wall pressure fluctuations with and without forcing using pulsed-plasma jets. The jet array is placed at 1.7δ from the compression corner (inside the separation bubble) and is pitched at - 30° (i.e. counter to the incoming flow).

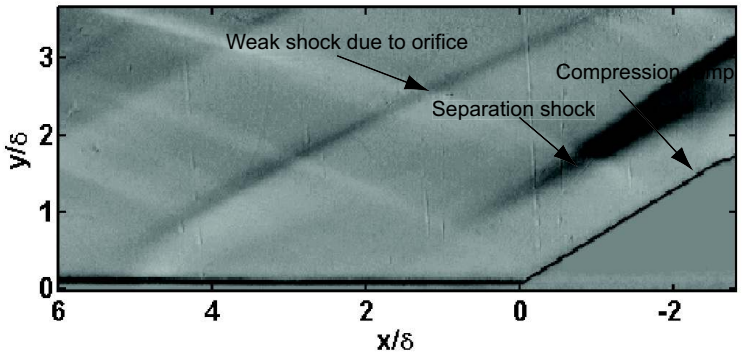

(a)

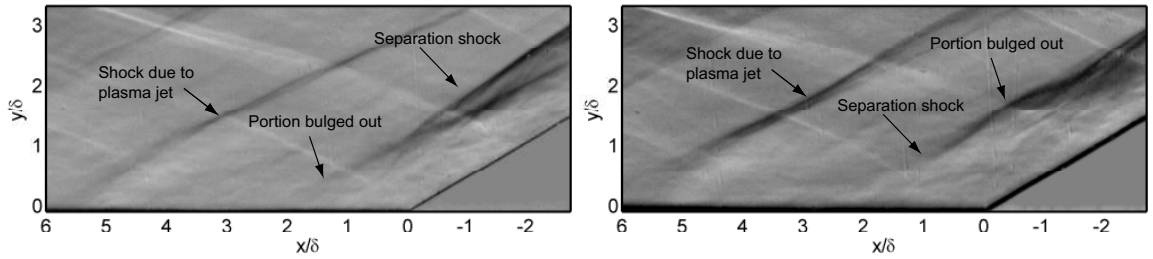

(b) (c)

Figure 6.12: Phase locked schlieren imaging showing the initial response of the separation shock to the pulsed-plasma jet. Figure (a) corresponds to the instant before the interaction while (b) and (c) was taken during the interaction. The time delays in figure (b) and (c) corresponds to 45 and 60 μs after the start of the discharge trigger respectively.

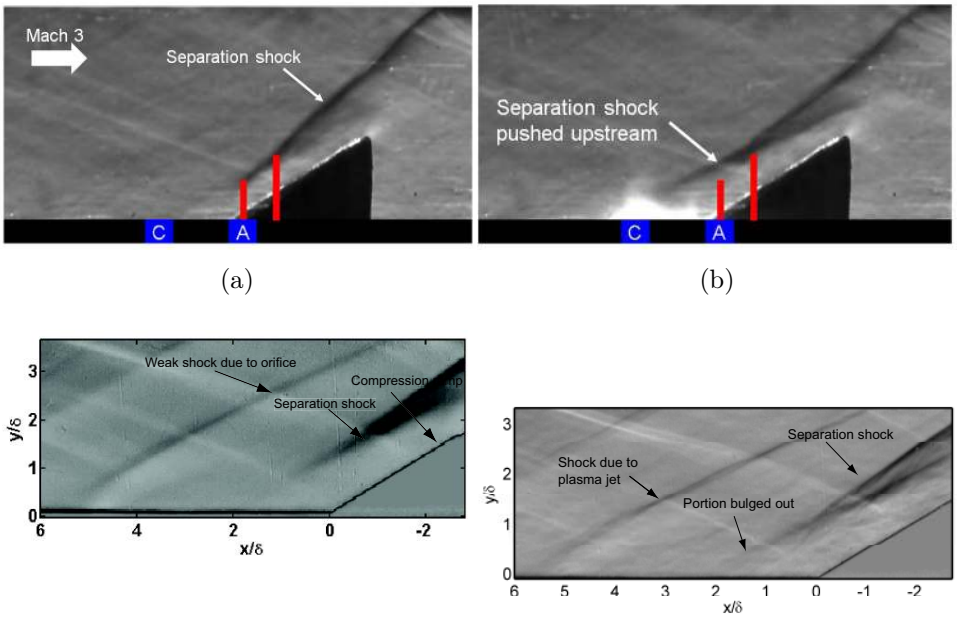

Figure 6.13: Comparison of the response of the separation shock to a low density perturbation by a DC glow discharge reproduced from Shin et al. (2008) with the response separation shock to the pulsed plasma during the initial phase of interaction. Figure 6.13 (a) and (b) corresponds to the schlieren image without and with low density perturbation respectively, reproduced from Shin et al. (2008) . 'A' and 'C' marks the location of the anode and the cathode of the discharge. The red lines marks the height of the separation shock at the given location, which is not relevant to the present study. Figure 6.13 (c) and (d) corresponds to the schlieren image without and with pulsed-plasma jet interaction respectively.

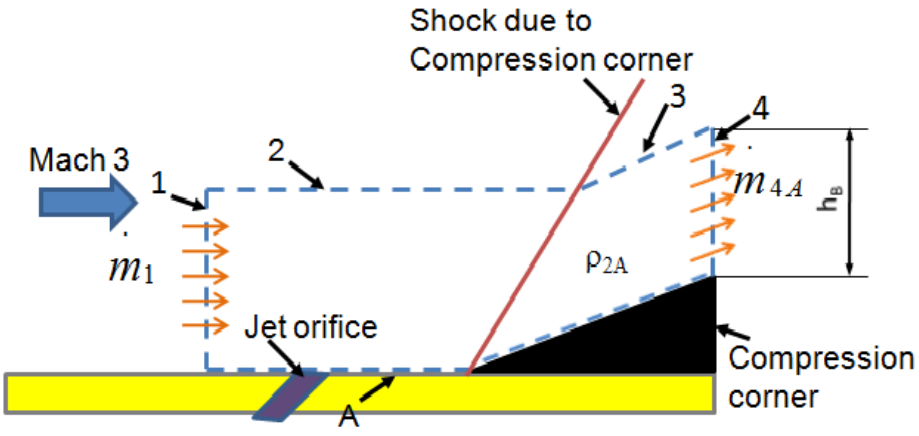

(a)

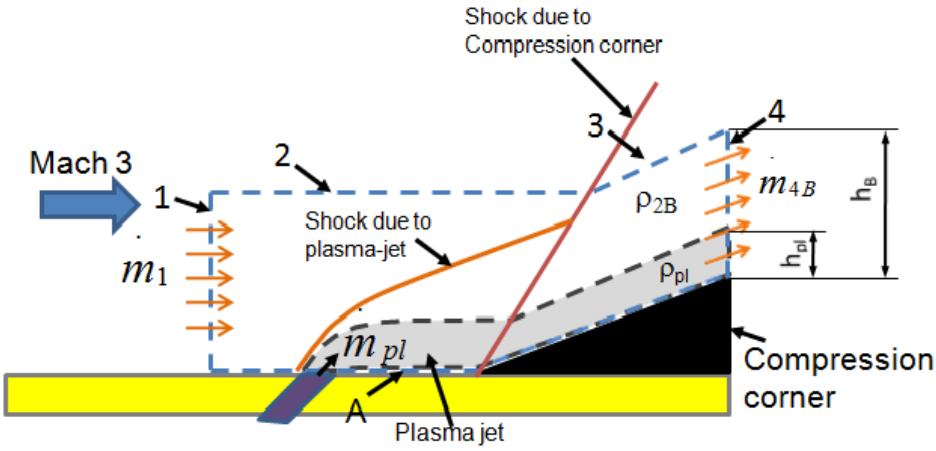

(b)

Figure 6.14: Schematic illustrating the cause of the bulge in the separation shock as the plasma jet passes through the interaction. (a) shows the separation shock structure without pulsed-plasma jet. (b) shows the modified separation shock structure due to the passage of the pulsed-plasma jet.

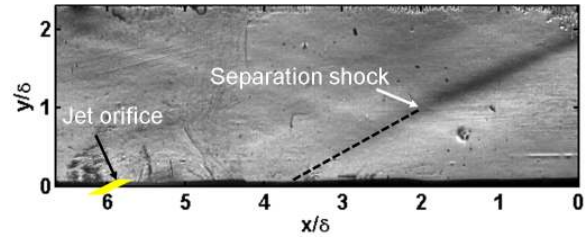

(a) 125μs

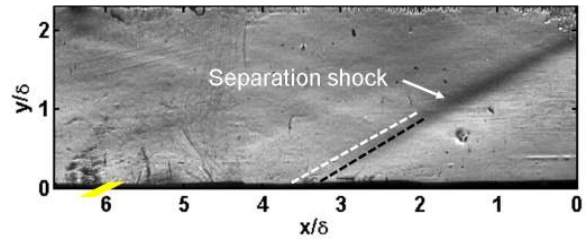

(b) 225μs

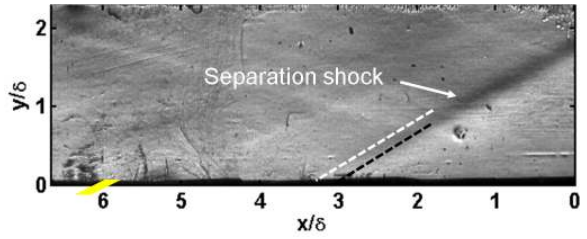

(c) 325μs

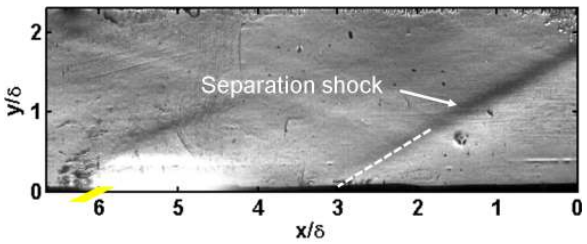

(d) 425μs

Figure 6.15: Phase average images of the separation shock motion with pulsed-plasma jet actuation. Each frame is separated by 100 μs, starting from 125μs after the start of the discharge trigger (frame (a)). Dashed line in black that indicates the mean shock position for the current frame, and the dashed line in white shows the location of the shock location in the previous frame.

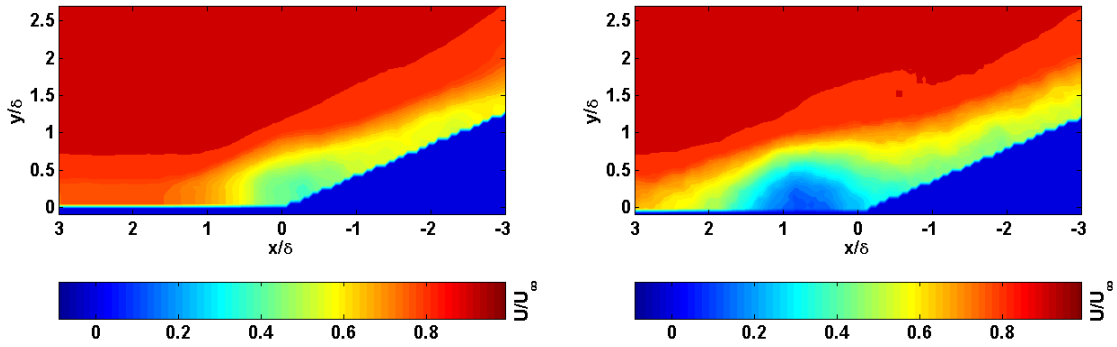

(a) unforced

(b) 100μs

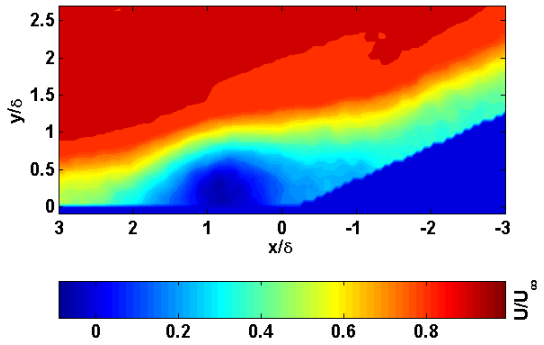

(c) 125μs

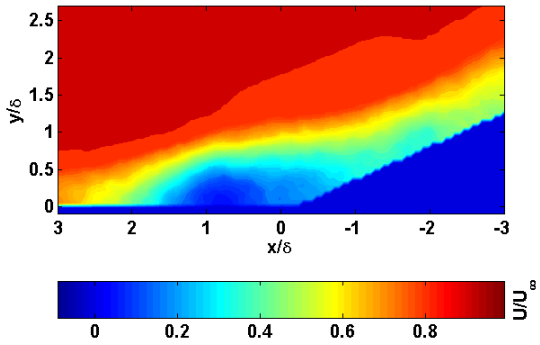

(d) 150μs

Figure 6.16: Phase averaged streamwise velocity contours captured without pulsed-plasma jet (fig (a)) and with pulsed-plasma jet at different time delays. Fig (b) corresponds to 100 μs (c) corresponds to 125 μs and (d) corresponds to 150 μs from the start of the discharge trigger.

Chapter 7

Summary and conclusions

A pulsed plasma actuator was studied that holds promise for use in supersonic flow control, owing to its high-bandwidth ($\sim kHz$) and high-injection velocity ($\sim 300\, m/s$). This actuator has the further advantage that the momentum that issues from the jet can be injected into the flow at directed angles. A thorough characterization of a pulsed-plasma jet issuing into a static vacuum chamber was conducted. The jet velocity was shown to be a function of the discharge current and the cavity material and independent of other relevant factors studied. The jet velocity was of order 300 m/s and increased only by 30% (from 250 m/s to 330 m/s) for a 10-fold increase in discharge current (from 1.2 A to 11 A). Reliable and repeatable pulses were obtained for frequencies up to about 5 kHz. Above 5 kHz the discharge would begin to miss pulses, which is believed to be due to the finite gas recharge time of the cavity. Spectroscopic measurements suggested that the discharge was characterized by a high degree of thermal non-equilibrium. The fraction of power that goes to gas heating was estimated to be about 10% of the input power, which is consistent with the values available in the literature. This inefficient gas heating is believed to be the main reason for the low jet velocity compared to the theoretical estimate of about 1000 m/s made by Grossman et al. (2003) and Cybyk et al. (2005). The finite time for energy deposition was also indirectly determined by measuring the evolution of the local-average gas temperature for different duration pulses. These measurements

were used to explain the effect of gradual gas heating on the jet exit velocity of the pulsed plasma jet.

Initial tests to assess the strength of the pulsed-plasma jet showed that the jet injected normal to the flow penetrated about 1.5δ. The estimated jet-to-crossflow momentum flux ratio was 0.6, which indicates the jet momentum flux is comparable to that of the supersonic freestream. A series of tests was conducted to explore the effectiveness of the pulsed-plasma jet array in controlling the unsteadiness of the separation shock in a SWBLI generated by a 30 compression ramp in a Mach 3 flow. The pulsed-plasma jet was tested in different configurations including normal injection, streamwise pitched and pitched and skewed. The latter was used in an attempt to induce a strong pulsed vortex generator. The results show that the pulsed-plasma jet in all configurations caused significant modification to the separation shock. Essentially, all of the configurations caused the separation shock to move upstream followed by a gradual recovery to its mean position. The pitched and skewed jets however, caused downstream motion of the separation shock for a brief time ($\approx 5 - 10\mu s$) demonstrating its potential to act as a vortex generator.

Time-resolved schlieren imaging of the interaction of the pulsed-plasma actuator with the SWBLI generated by a 24° compression corner placed in a Mach 3 flow was also made. The effect of actuator location was explored by placing the actuator in the upstream boundary layer and at two locations within the downstream separated flow. The first case studied was with the actuator placed in the upstream boundary layer. Time-resolved schlieren imaging showed that separation shock motion could be characterized by an initial quick upstream motion when the pulsed plasma jet passes through the separation shock followed by a slower recovery to its unforced mean position. By following the separation shock close to the floor, it was found that the shock

motion was locked to the pulsing frequency. The fluctuating wall-pressure fluctuation measurements showed about 30% decrease in the intermittent region at the frequencies that correspond to the low-frequency unsteadiness of the SWBLI. With upstream forcing, the effect of the forcing depended strongly on where the pressures were being measured within the interaction. Some pressure measurement locations showed considerable changes in the power spectrum with forcing, whereas some locations showed no effect of forcing. This observation is believed to be related to the organization of the separation bubble, i.e., how strongly the dynamics of different regions of the flow are coupled. A study was also made to study the effect of injection location. It was found that the pulsed-plasma jet, when injected from upstream of the separation shock, caused a significant modification to the separated flow dynamics. However, the same jet did not cause a noticeable change in the dynamics when injected from inside the separation bubble or near reattachment. The lack of effect with downstream injection location was observed for jets that were skewed by 30 degrees in the upstream and downstream directions.

It is useful to consider how the pulsed-plasma jet based SWBLI unsteadiness control might make an important contribution. Since the separation shock pulsations are locked to the pulsing frequency of the plasma jet, the frequency of the pulsations can be detuned off the resonance frequency of the aerodynamic structures. Thus the amplitude of mechanical and thermal loading is tremendously mitigated at the resonance frequencies. The important difference in the mitigation of the unsteadiness using pulsed-plasma jet is that the decrease in amplitude occurs at all times; the amplitude of the fluctuations in the resonance frequency range for the forced case never reaches the values of the unforced case at any point in time. Moreover, since the frequency of the loading is known, "detuners" can be placed at different locations

in the aircraft structures so that the effect of the periodic loading can be largely mitigated.

A closer look at the schlieren movies and the time trace reveals that the amplitude of the separation shock motion is considerably higher in the forced case, compared to the unforced case. This essentially implies that it may be possible the magnitude of mechanical and thermal loading by the separation shock has increased upon forcing and that a larger region is subjected to the fluctuating mechanical and thermal loading. This is indeed true for the pulsing frequencies used for this study. However it was noted that the recovery velocity of the separation shock for all the pulsing frequencies tested was constant (about 2% U_∞). This result implies that it may be possible to reduce the amplitude of the motion of the separation shock by increasing the pulsing frequency of the plasma jet. The significance of this result is that the separation shock would essentially be anchored to a location. However, this hypothesis could not be tested in the current study because of the limitation in the maximum power that the power supply could deliver. Hence, the future experiments with higher pulsing frequencies may shed more light on the control of the separation bubble unsteadiness at these frequencies and the associated amplitude of the forced separation shock motion.

At this point, it is also instructive to have an outlook about the practicality of using the pulsed-plasma jet for real-world SWBLI unsteadiness control in hypersonic aircraft. The idea would be to cover those surfaces on the airplane where the SWBLIs occur, with a linear array of pulsed-plasma jets. Assuming the inter-jet spacing of about 4 jets per inch (roughly 200 per meter), let us compute how many such plasma-jets would be required to control the SWBLI unsteadiness of the wing, control surface and inlet. Assuming a wing span of 60 ft (20 m), tail (horizontal and vertical) length

of 60 ft (20 m) and an total engine inlet perimeter of 20 m, the total number of plasma-jets required would be about 10000. Assuming that the plasma-jets have to be placed at both sides of the wings and tail, the total number of plasma-jets would be roughly 40000. The mean input power per jet for the present experiments is about $400\,W$. It should be noted that the gas heating efficiency of the present experiments was about 10%, which should be about the same for the pressure and density conditions that prevail at the cruising altitude of hypersonic aircrafts ($\approx 40\,km$). Hence, in the practical scenario, the mean input power per jet that would be required to generate plasma-jet with similar momentum as this study would be approximately 400 W, as in the present experiments. Thus, the power required to control the SWBLI unsteadiness of the entire airplane would be roughly of the order of few tens of MW. This target of power requirement is achievable with the available technology. Hence, the pulsed-plasma jets do hold a significant promise to be employed for hypersonic airplanes. However a significant amount of work is required to optimize different parameters and design effort is required before the pulsed-plasma jets could find a commercial application.

Appendices

Appendix A

Wall pressure fluctuation measurements in reacting flows

Pressure fluctuations are commonly measured to study the unsteadiness associated with any supersonic flowfield such as jets, separation bubble, base flow, etc. With the rapidly growing application of plasma discharges towards supersonic flow control, pressure fluctuations have to be performed in a reacting environment to study such situations. The pressure fluctuations are relatively simple to measure in a non-reacting flow; however, in a reacting environment the presence of charge species pose a huge impediment for the measurement. The different problems that are present in the reacting environment are as follows:

- Charged particles strike the sensing membrane of the transducer, and causes permanent changes in its frequency response and calibration
- Charged species that strike the sensing element creates permanent material damage
- Very high electromagnetic interference due to the sudden appearance of the charged species.

It should be mentioned that whereas the EM noise could be minimized to a great extent with appropriate shielding, the material damage to the transducer sensing element is a more severe and unpredictable problem to handle. This is particularly the

case with high frequency response transducers whose sensing membranes are made of semiconductor material, since the damage threshold current of these sensing membranes is very small. In addition, they can also be damaged because of charge build up with time owing to their inherent capacitance. Thus new strategies are required in order to protect the transducers and to make meaningful pressure fluctuation measurement. In this appendix, one such strategy is explained and successfully applied to study the SWBLI unsteadiness control using pulsed-plasma jet actuators. The location of the pressure fluctuation measurement is at the floor of the test section.

In order to understand the flow situations where the presence of ions should be considered while designing the experiments, it is necessary to find out if the charged species are actually going to be present in the measurement location. The methodology that is to be adopted to ascertain the presence of charged species is to compare the recombination time scale of the charged species to the time scale required by the charged species to convect to the measurement station. If the recombination time scale is greater than or equal to the convection time scale, then the charged species are going to be present in the measurement location and additional strategies such as the one discussed in this appendix is required for making successful measurement.

For the air plasma, such as the one in the present work, at pressures from few tens of torr to about 1 atmosphere, the dominant charged species are the N_2^+ ions and the electrons. Hence, the time scale of the recombination time scale of the N_2^+ ions alone is considered. The most dominant pathway of the recombination of the N_2^+ ions is the dissociative recombination with the collision with electrons as mentioned by Yu et al. (2001). The chemical equation of the reaction is as follows:

$$N_2^+ + e^- \rightarrow 2N$$

Table A.1 shows the Arrhenius rate parameters required to compute the reaction rate coefficient, reproduced from Deconinck et al. (2007). The reaction rate coefficient k_f is computed using the following expression:

$$k_f = AT_e^b e^{-\frac{E}{T_e}}$$

where T_e denotes the electron temperature. For this study, the value of T_e is estimated to be about 1.2 eV, as shown in chapter 4. Using the aforementioned value of T_e and Arrhenius rate parameters, the reaction rate coefficient is estimated to be $k_f = 1.6 \times 10^{-14} \#/m^3$. The reaction rate of recombination of N_2^+, which is the same as the rate of depletion of the charged species (ions), is estimated to be:

$$R = \frac{dn_{N_2^+}}{dt} = k_f n_{N_2^+} n_{e^-}$$

The time scale of depletion of the charged species (ions) is found using the expression

$$\tau_{N_2^+} = \frac{n_{N_2^+}}{\frac{dn_{N_2^+}}{dt}} = \frac{1}{k_f n_{e^-}}$$

The electron number density is estimated to be $n_{e^-} \sim \mathcal{O}(10^{19} \frac{\#}{m^3})$ in chapter 4. Thus the time scale of depletion of charged species is found to be $\tau_{N_2^+} \sim \mathcal{O}(10\mu s)$. This time scale gives the lower limit of the actual recombination time scale, since a large fraction of the electrons is unaffected by the bulk gas dilitation and is never issued with the plasma jet. The convection time scale is determined as

$$\tau_f = \frac{L}{U_\infty}$$

Reaction	A(#, m)	b	E(K)
$N_2^+ + e^- \rightarrow 2N$	2.54×10^{-12}	-0.5	0

Table A.1: Arrhenius rate parameters for the dissociative recombination of N_2^+

The length scale L is the separation between the pulsed-plasma jet orifice and the measurement location, which is of the order of 1 cm. Thus the flow time scale is estimated to be $\mathcal{O}(10\mu s)$. Thus the convective time scale of the ions is of the same order of magnitude as the ion depletion time scale. Hence there is a very high probability that the charged species prevails close to the measurement location, which necessitates the strategies to protect the measurement devices.

There have been a few successful measurements of pressure fluctuations in reacting environments by previous researchers. Samimy et al. (2007) used an array of microphones to measure pressure fluctuations in the farfield of a mixing layer manipulated by pulsed arc discharges (LAFPA) at atmospheric pressure. More recently, near-field pressure fluctuations were also measured using Kulite pressure transducers for the same experimental configurations by Sinha et al. (2008). High-frequency pressure measurements were also attempted to study plasma-based SWBLI control at low pressure by Caraballo et al. (2009). However, they reported that the charged species caused significant damage to the pressure transducers making it impossible to make any meaningful measurements. Thus, with the advent of the electric discharges for supersonic flow control, development of innovative means to measure pressure fluctuations is necessary in order to make simple and meaningful study of the flow field characteristics in the presence of charged species. The measurements should also be in reasonable proximity to the actuators in order to get a more accurate estimate of the strength of actuation. This appendix describes one such technique to make measurements of pressure fluctuations in close proximity to the actuators with

acceptable noise and without damaging the transducers. The technique has been successfully employed to study shock wave/ boundary layer interaction control using a pulsed-plasma jet.

A.1 Principle of the technique and design considerations

The principle of this technique is to trap the charged species present in the pulsed-plasma jet by a ground electrode before the ions can reach the transducer. Thus, only the hot jet, without the charged species, convects over the transducer. In order to accomplish this, a ground electrode was placed upstream (to the direction of convection of ions) of the pressure transducer to drain the incoming ions. However, the ground electrode could not be permanently grounded since the anode of the pulsed-plasma jet circuit typically reached high enough electric potential to create a direct discharge to this ground electrode, and thus bypassing the cathode of the pulsed-plasma jet. This led to undesirable interruption in the generation of the pulsed-plasma jet and a very high EM noise in the transducer. Hence, the ground-electrode was connected to ground only during the time when the charged species were expected to convect over it. The ground electrode also required a ballast resistance in order to prevent a current surge through the ground electrode while the ions were being trapped by it. In addition, the ballast resistance was low enough to trap all the ions without the ground electrode reaching any appreciable potential that would prevent further draining of ions. A circuit was designed that meets all the above requirements and is described in the next section.

A.2 Experimental setup

A schematic of the experimental set up and an illustration of the operation of this technique is shown in figureA.1. The set up consists of a pulsed ground (PG) placed about 1δ upstream of the transducer. The pulsed ground electrode was made of copper and its diameter was 2.5 mm. Figure A.1 (b) shows the luminosity image of the pulsed-plasma jet. It can be observed that there is a visible glow on the surface of the pulsed ground electrode, which is due to the collection of ions by the electrode. Thus, it can be seen that the pulsed ground electrode indeed drains the ions that convects past it.

The schematic of the circuitry employed for operating the pulsed ground is shown in figure A.2. The switching circuit is controlled by a master clock (marked as function generator), which triggers the circuit at a preset time delay. The master clock also controlled the generation of the pulsed-plasma jet. A variable resistor (VR) was connected to the pulsed ground electrode (PG) and the resistance of VR was set according to the procedure described in the next paragraph. The transducer was located at distances between 1.4 and 0.9 inches from the plasma jet orifice. These locations correspond to the corner of the compression ramp through the intermittent region of the SWBLI.

Before the pressure transducer was mounted for measurements, a surrogate transducer was placed in the location of the transducer to determine the resistance of the variable resistor (VR). The surrogate transducer was made of a copper wire whose diameter was same as the pressure transducer. A resistor was connected to the surrogate transducer that would match the impedance of the pressure transducer. The resistance of VR was adjusted such that it would prevent the direct discharge from anode to pulsed ground electrode (PG), yet drain the ions in the plasma jet before

they could reach the transducer. The current through the surrogate transducer was monitored in an oscilloscope. It should be noted that while current flows through the surrogate transducer, a visible glow could be seen on its surface because of the ions striking its surface. The value of VR was adjusted till the current through the resistor vanished and no visible glow could be seen on the surface of the surrogate transducer.

The activation time and duration of the PG was determined from the trajectory and the duration of the pulsed-plasma jet measured using plan-view PLS measured at locations close to the floor of the test section. The trajectories of the pulsed-plasma jet with a discharge current of 3.9 A, measured at $\frac{y}{\delta} = 0.2\, and\, 0.5$, are shown in fig. 5.3. The streamwise extent of the pulsed-plasma jet at different pulse widths are also shown in fig. 5.11. It was mentioned earlier in chapter 4 that the pulsed-plasma jet was convected at the local undisturbed flow velocity without any noticeable change in its structure. It was also noted in chapter 4 that the duration of the pulsed jet scaled with the pulse width of the discharge for the range of pulse durations tested. Hence, by knowing the distance between the pulsed ground and the jet orifice, the start and end time of the pulse was set such that the electrode remained grounded while the plasma jet convected past the electrode. Once the resistance of VR was set to the appropriate value and the pulse duration of the pulsed ground electrode was determined, the surrogate transducer was replaced by the actual pressure transducer used for measurement (Kulite transducer model XCQ-062-50A). The cables of the transducers were shielded to minimize the effect of electromagnetic interference emanating from the pulsed-plasma jet.

A.3 Sample time series

Pressure time series data were taken for 2 s while the pulsed-plasma jet was in operation. The pulsing frequency of the pulsed-plasma jet was varied between 1 kHz and 4 kHz. The pulse width of the jet was fixed at $20\,\mu s$ and the peak discharge current was set at 2 A. The measurements were started after 2 seconds from the start of the pulsed-plasma jet in order to make sure a steady state had been established. A sample time series of the pressure fluctuations with a single pulsed-plasma jet, pulsed at 2 kHz, is shown in figure A.3. The corresponding discharge current waveform, measured simultaneously as the voltage drop across a 1.2Ω resistor placed in the circuit, is also shown (marked Discharge current). It can be seen that the pressure fluctuations look predominantly free of spikes due to electromagnetic (EM) noise. However, spikes do occur shortly after the start of the discharge and at the end of the discharge. The spikes are due to the maximum time rate of change in current (from OFF to ON and ON to OFF), which causes very high levels of EM noise. The maximum magnitude of these noise spikes is approximately two times larger than the rms pressure fluctuations present in the unforced flow. It is important to note that the width of the noise spikes is less than $30\,\mu s$. It was observed from the PLS imaging that the interaction of the pulsed-plasma jet with the separation shock began only after about $60\,\mu s$ from the start of the discharge trigger. By this time the pressure signal was free of EM noise, which makes it possible to study the effect of the pulsed-plasma jet on SWBLI unambiguously. On increasing the number of pulsed-plasma jets from one to three increases the noise considerably. Figure A.4 shows the time series with three jets**.** The plasma jet was pulsed at 2 kHz. The spikes due to EM noise are marked in the figure. It can be clearly seen that the scaling of noise is not linear with the number of pulsed-plasma jets. One of the possible reasons for such

a large increase in the magnitude of the noise is that only a single ground electrode was employed even with an array of three pulsed-plasma jets. Thus it is possible that when the charged species from the individual jets reached the ground electrode they started to interact with one another, and thus creating plasma instabilities and other effects that amplified the noise non-linearly. It should be noted that even for the case with the three pulsed-plasma jet array, the single ground electrode completely drained all the charged species and the ions did not strike the transducers.

A.4 Data processing

The effect of the pulsed-plasma jets on the SWBLI was studied by comparing the power spectra of pressure fluctuations at different streamwise locations of SWBLI. However, the short-duration spikes that occur occasionally when the pulsed-plasma jet was generated caused additional non-trivial contribution to the power spectra at all the frequencies. The reason for this can be understood by considering the spike as an approximate delta function whose width in the frequency domain is very broad. Hence, it is necessary to process the data to remove the spurious spikes before their power spectrum is computed. The procedure followed in processing the data includes identifying the spikes by computing the slope at individual points using a forward difference scheme. The spikes due to EM noise were identified as the data points whose gradient is beyond ± 4 standard deviations of the mean gradient. The value of the threshold was chosen such that none of the data points that correspond to the actual signal were removed. Typically the number of data points that correspond to EM noise was about 1-2% of the data samples. Once the spurious data points were identified, they were replaced by interpolating the data values before and after the spike that were within the global maximum and minimum values of the unforced

case. The number of interpolated data points per identified spike was about 3 to 5. Hence, the total number of modified data points was between 5 – 10% of the total data points.

A.4.1 Demonstration of processing with benchmark cases

In order to demonstrate the processing scheme, pressure fluctuations slightly downstream of the intermittent region of the SWBLI ($x/L \approx 0.8$, where L is the interaction length scale) generated by a 24 compression ramp were measured. An array of three pulsed-plasma jets was used in order to illustrate the ability of the procedure to filter out the effect of even large noise spikes. In this experiment the orifice of the pulsed-plasma jets were covered with a high temperature insulating tape so that the pulsed-plasma jets were never issued when the discharge was generated. Hence, the pressure data consists of the unforced pressure fluctuations with contributions from the EM noise, with no effect of forcing due to the pulsed-plasma jet. Thus, after data processing, the spectra with and without the pulsed-plasma jets should overlap. The pulsing frequency tested was 2 kHz, which corresponds to the typical forcing frequency employed during separation shock control experiments. Figure A.5 (a) shows the comparison of the pressure spectra with and without the discharge, but without performing any data processing. The spectra with the discharge was scaled down by 10 times in order for the pressure spectra to match on the same scales. This 10 fold increase in the broad-band frequency is because of the large EM spikes that contributes to the energy at all frequencies. The contributions from the EM spikes can also be clearly seen in the scaled-down power spectra. The spectra does not seem to agree with the case without pulsed-plasma jet at any frequencies. Figure A.5 (b) shows the comparison between the pressure spectra without discharge and with

discharge after data-processing. It should be noted that the spectra with pulsing was not scaled down as it was done in figure A.5 (a). It can be observed from figure A.5 (b) that there is a very high degree of overlap between the pressure spectra. The spikes at the pulsing frequency and its harmonics can be observed. Thus, it is clear that the interpolation scheme removes the contribution of the EM noise in the broad-band frequencies. However, the interpolation scheme cannot completely remove the contribution of the EM noise at its resonant frequencies. Thus, the scheme localizes the effect of the EM noise at the pulsing frequency and its higher harmonics, while keeping the remaining spectra clear of its influence.

A study of the impact of the interpolation scheme on the power spectrum at different frequencies was also studied. In this procedure a pressure fluctuation data set of an unforced case was selected. About 3 to 6 data points were chosen at equal intervals from this data set. Different intervals were chosen to simulate different pulsing frequencies. The chosen data points were removed and replaced with interpolated values between the preceding and succeeding data points. The power spectral density of the modified data at a frequency of 2 kHz was compared with that of the original data in figure A.6. The spectra without interpolation plotted in black. Case 1 corresponds to the interpolation between 3 data points. In this case 4.8% of the original data were modified. Case 2 corresponds to the interpolation between 6 data points. In this case 9.6 % of the original data were modified. It can be seen that in all the cases there are no significant modifications to the spectra. The power spectra of the interpolated signals are within 5% of the power spectra of the original signal. This shows that the interpolation procedure does not introduce major spurious features to the power spectra.

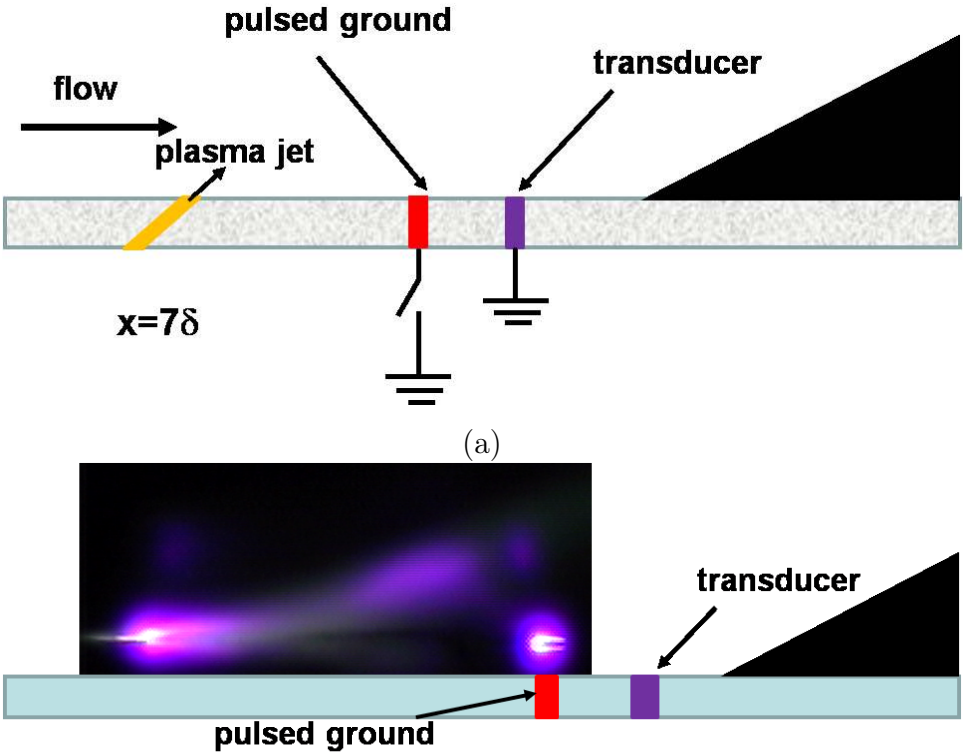

Figure A.1: Schematic of the experimental set up of the pressure measurement (fig. (a)) and the plasma luminosity image showing the working of the experimental procedure (fig. (b))

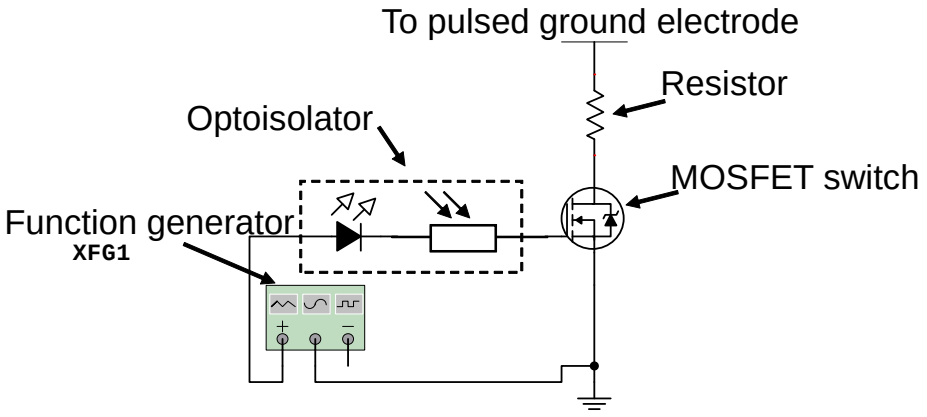

Figure A.2: Schematic of the circuitry of the pulsed ground electrode employed for pressure fluctuation measurements

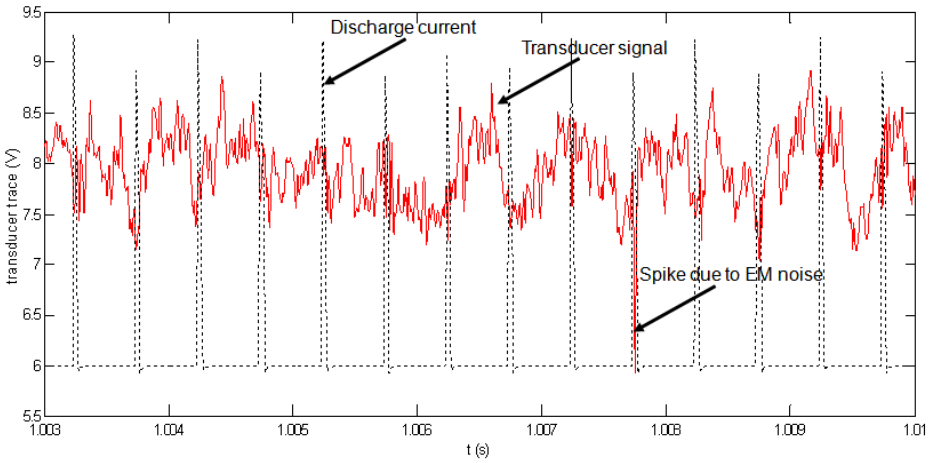

Figure A.3: Sample time trace of the pressure transducer signal with a single pulsed-plasma jet. The discharge current of the pulsed-plasma jet was 2 A. The discharge current waveform measured simultaneously with the pressure signals is also shown as dotted lines. The spikes due to EM noise are also marked.

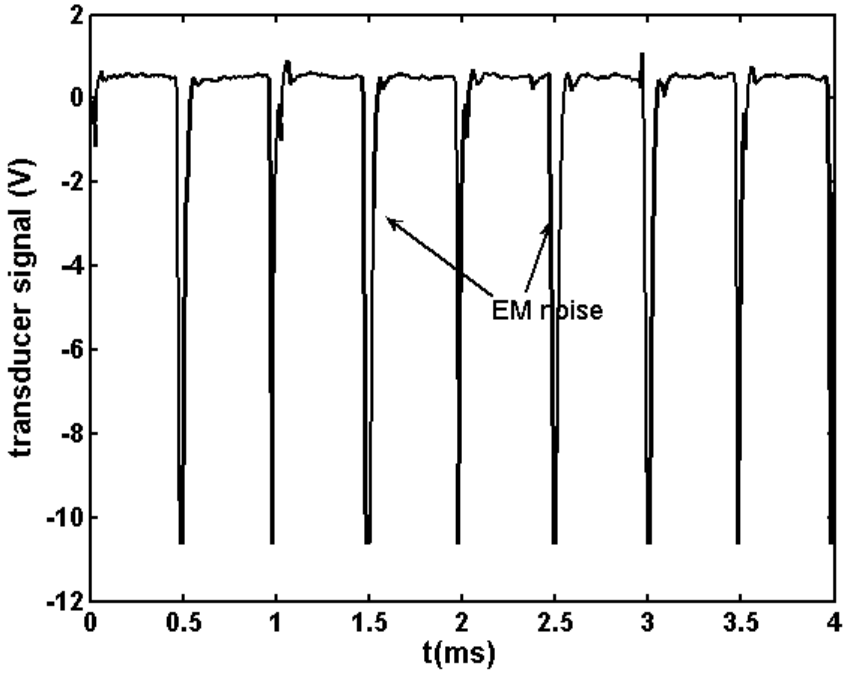

Figure A.4: Sample time trace of the pressure transducer signal with an array of three pulsed-plasma jets.

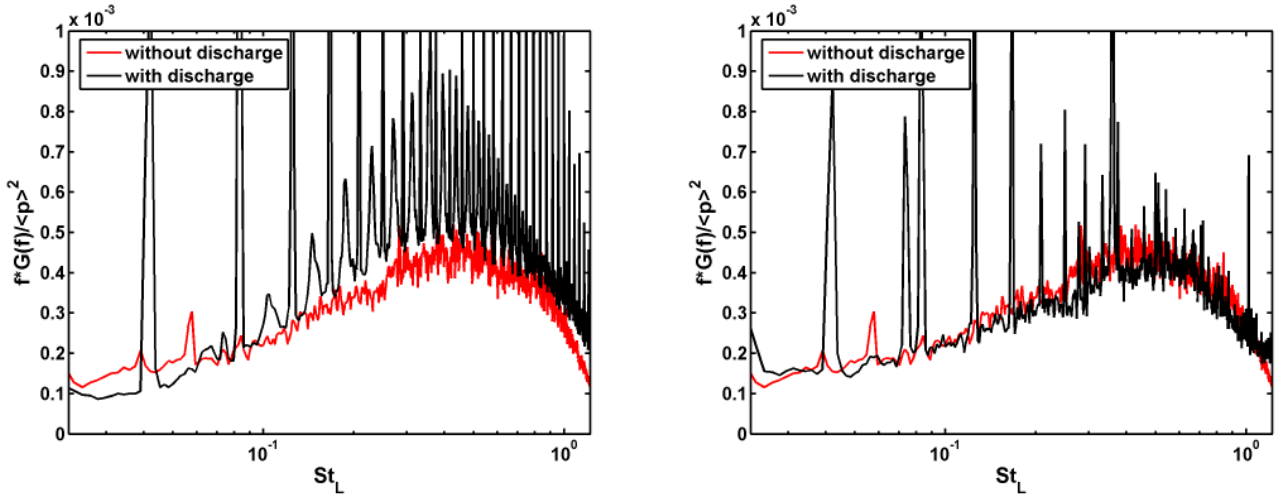

Figure A.5: Demonstration of the interpolation scheme used for data processing. Fig. (a) pressure power spectra for cases with and without discharge, but with no plasma jet. No processing was used for the case with discharge. Fig. (b) pressure power spectra with and without discharge (and no plasma jet), but where the case with discharge has been processed with the technique described in this appendix.

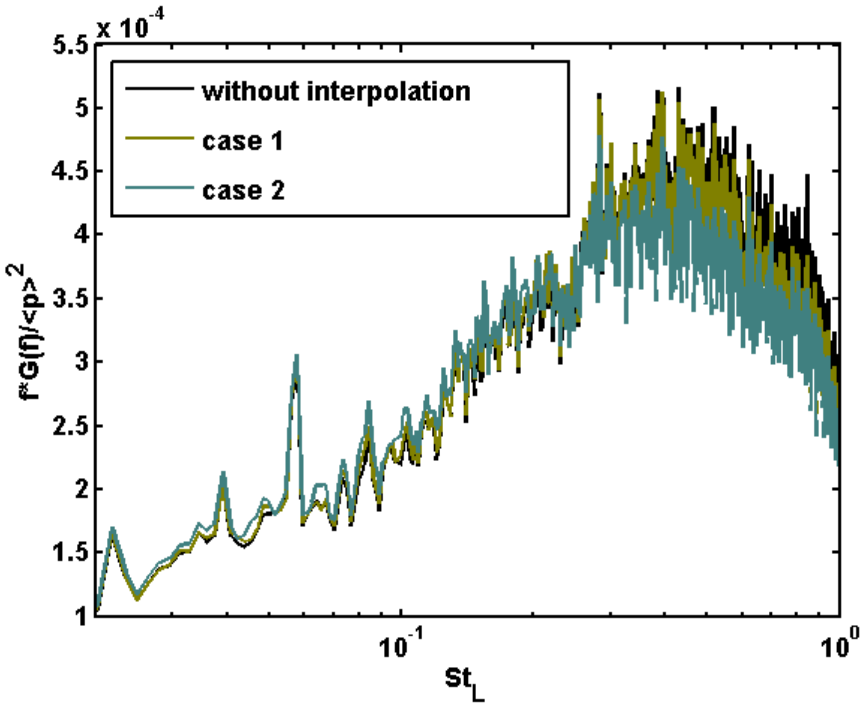

Figure A.6: Effect of interpolation of the data on the power spectrum. Case 1 corresponds to interpolation between 3 data points which modifies 4.8 % of the original data and case 2 corresponds to interpolation between 6 data points which modifies 9.6% of the original data.

Appendix B

Temperature measurement using Optical emission spectroscopy

Optical emission spectroscopy was performed to obtain spectra of the $C^3\Pi_u \rightarrow B^3\Pi_g$ transition of the N_2 molecule. The rotational and vibrational temperatures were estimated by fitting synthetic spectra, computed for different temperatures, to the measured spectra. A detailed description of the estimation procedure can be found in Shin (2007).

Briefly, the intensity of a radiative transition between two rotational levels can be described as

$$I \sim N'_{n',v'} \frac{\nu'^4 g_{J'} \Phi_{P'}}{Q_r} e^{-\frac{E'_r}{kT_r}} \tag{B.1}$$

where:

Q_r is the rotional partition function given by

$$Q_r = \sum_J g_{J'} \Phi_{P'} e^{\frac{-E'_r}{kT_r}} \tag{B.2}$$

$g_{J'}$ is the degeneracy of the J'^{th} rotational level given by

$$g_{J'} = 2J' + 1 \tag{B.3}$$

$\Phi_{P'}$ refers to the contribution of the nuclear spin at the different levels. It takes a value of 2 for even J' levels and 1 for odd J' levels.

E'_r corresponds to the energy level of the upper rotational level from which the transition occurs

$N'_{n'v'}$ corresponds to the total number density of the electronic (n') and vibrational (v') state in which the rotational transition occurs.

A similar expression for intensity can also be written to describe a rovibronic transition as follows:

$$I \sim N_{n'} \frac{\nu'^4 S_{v'v"} g_{J'} \Phi_{P'}}{Q_r Q_v} e^{-(\frac{E'_r}{kT_r} + \frac{E'_v}{kT_v})} \tag{B.4}$$

where:

Q_v is the partition function of the vibrational energy levels given by

$$Q_v = \sum_J \Phi e^{\frac{-E'_v}{kT_v}} \tag{B.5}$$

E'_v corresponds to the energy level of the upper vibrational level from which the transition occurs

$S_{v'v"}$ is the band strength of the vibrational transition between the v' and $v"$. The value of the band strength, $S_{v'v"}$ can be found in the literature for various gases.

$N'_{n'}$ corresponds to the total number density of the electronic (n') state in which the rovibronic transition occurs.

Although the rotational and rovibronic transitions occur at discrete frequencies, the homogeneous and inhomogeneous broadening that are inherently present in the system causes non-zero intensities at all frequencies. The dominant form of broadening for the present experiments was the instrument broadening. The magnitude of instrument broadening was measured from the emission spectrum of low-pressure krypton calibration lamp. The emission spectrum of the krypton corresponding to each electronic transition was measured and a Gaussian was fitted to each of the measured lines. The instrument broadening was measured as the mean FWHM of the fitted Gaussians. The value of instrument broadening for the present experiment was 0.094 nm (FWHM). MATLAB codes were developed to compute the synthetic spectra, which incorporate the effect of instrument broadening. It should be noted that in order to percieve the intensity alteration due to nuclear spin, the spectra should resolve the lambda doubling of the transition (see Shin (2007)). However, for the present experiment the instrument broadening overwhelms the spectra making it impossible to resolve the lambda doubling.

B.1 Estimation of the rotational temperature

The rotational temperature was estimated by fitting synthetic spectra at different temperatures individually to the $C^3\Pi_u \rightarrow B^3\Pi_g$ (0-2) transition and $C^3\Pi_u \rightarrow B^3\Pi_g$ (1-3) transition of N_2 SPS. A comparison of the measured spectra with the synthetic spectra at different temperatures for the $C^3\Pi_u \rightarrow B^3\Pi_g$ (0-2) transition is shown in fig B.1 (a) - B.1 (c). An error estimate is also shown for different temperatures in figure B.1 (d). The error is defined as the fractional deviation of the synthetic

fit from the measured spectra. The normalization is done using 10 - point running averaged experimental spectra. The rotational temperature that corresponds to the minimum error was taken as the actual rotational temperature. For the spectra shown in the figure which corresponds to a pulsed plasma jet of 1.2 A discharge current this temperature corresponds to 700 K and the relative error was observed to be about 12 %.

B.2 Estimation of the vibrational temperature

Once the rotational temperature was estimated it is fairly straight forward to obtain the vibrational temperature. In order to obtain the vibrational temperature at least two vibrational transitions are needed. For the present case, the transition between levels $C^3\Pi_u \rightarrow B^3\Pi_g$ (0-2) and $C^3\Pi_u \rightarrow B^3\Pi_g$ (1-3) were used to compute the vibrational temperature. Once the rotational temperatures were obtained using the procedure described in the previous section, the vibrational temperature was determined by matching the relative intensities of the bandhead of the different vibrational transitions. An example spectra in which the rotational and vibrational temperatures were estimated using the above procedure is shown in figure B.2. This figure shows the spectrum of the pulsed-plasma jet with 6.5 A discharge current per jet. It can been seen that the vibrational temperature of 3100 K matches the relative intensities of the band head of the two vibrational transitions shown. The corresponding rotational temperature was estimated to be 800 K.

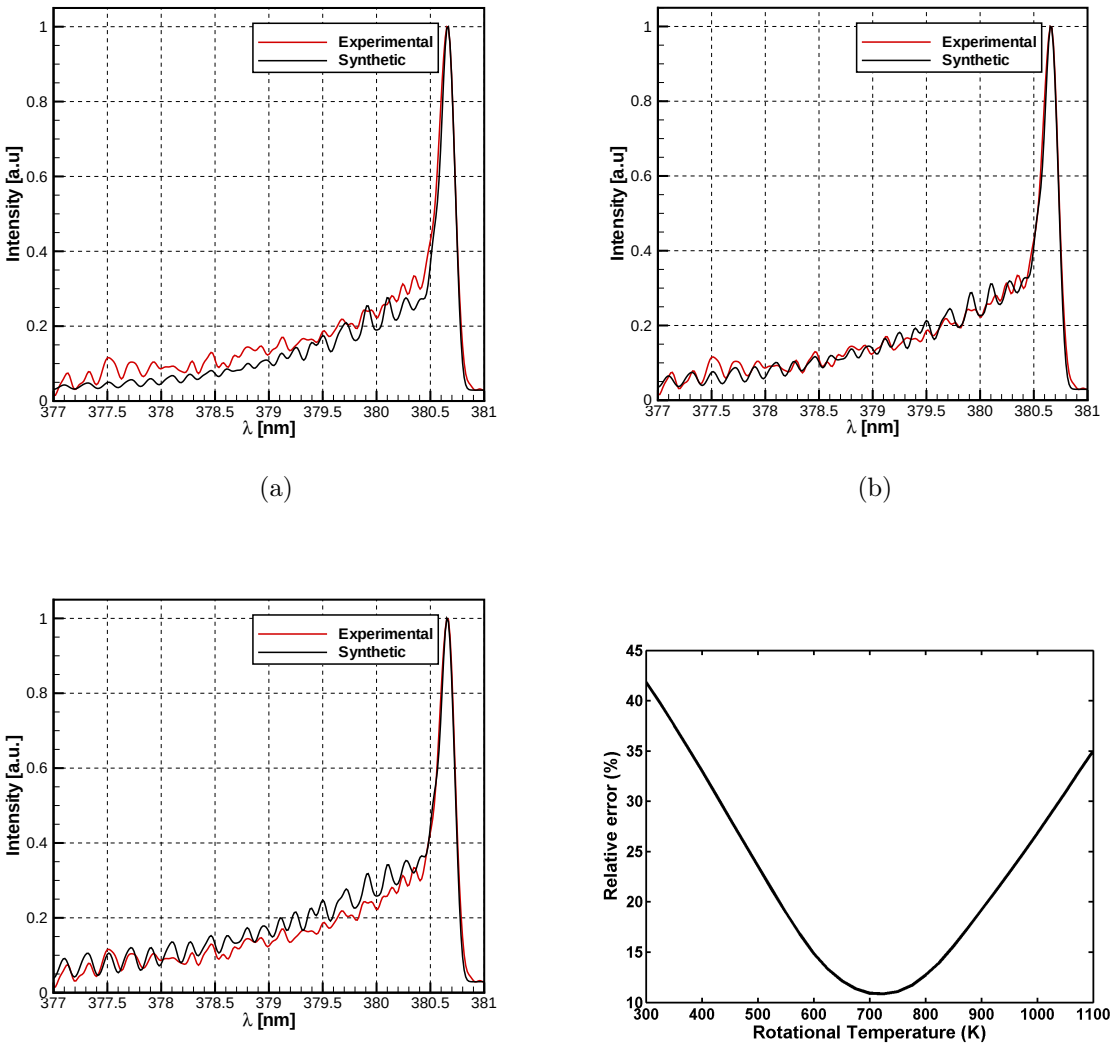

Figure B.1: Comparison of the synthetic rotational spectrum fit at different rotational temperatures to the measured spectrum. The synthetic spectrum is shown in red and measured spectrum is shown in black. Figure (a) corresponds to the spectrum at 500 K, (b) 700 K and (c) 900 K. Figure (d) shows the relative percentage error between the synthetic fit and the measured spectrum.

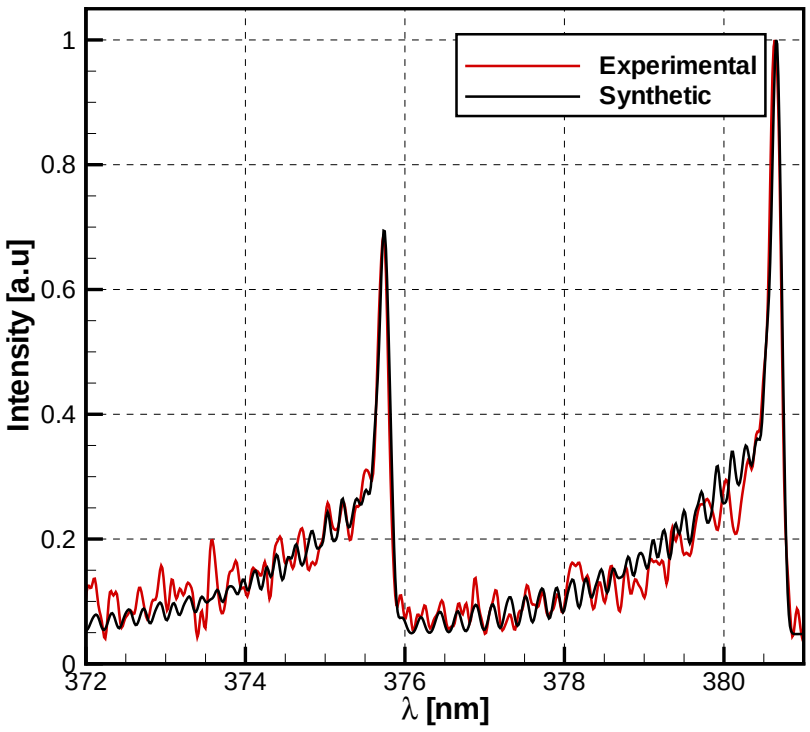

Figure B.2: Comparison of the synthetic rovibronic spectrum with the measured spectrum. The rotational temperature was estimated to be 800 K and vibrational temperature was estimated to be 3100 K.

Bibliography

D. S. Dolling, Fluctuating loads in shock-wave / boundary layer interaction: tutorial and update, AIAA 93-0284 .

D. S. Dolling, 50 years of shock wave/boundary layer interaction - what next?, AIAA Journal 39 (8) (2001) 1517–1531.

P. R. Viswanath, Shock wave turbulent boundary layer interaction and its control: a survey of recent developments, Sadhana 12 (1988) 45–104.

E. M. Braun, F. K. Lu, D. R. Wilson, A critical review of electric and electromagnetic flow control research applied to aerodynamics, AIAA 2008-3788. .

R. L. Resler, W. R. Sears, The prospects for Magneto-aerodynamics, Journal of the Aeronautical Sciences 25 (4) (1958) 235–245.

T. C. Corke, M. L. Post, D. M. Orlov, Single dielectric barrier discharge plasma enhance aerodynamics: physics, modeling and applications, Experiments in Fluids 46 (2009) 1– 26.

D. Knight, A selected survey of Magnetogasdynamic local flow control at high speeds, AIAA 2004-1191 .

T. C. Corke, M. L. Post, Overview of plasma flow control: concepts, optimization, and applications, AIAA 2005-563 .

C. L. Enloe, M. G. McHarg, G. I. Font, T. E. McLaughlin, Plasma-induced force and self-induced drag in the dielectric barrier discharge aerodynamic plasma actuator, AIAA 2009-1622 .

M. Post, T. Corke, Separation control using plasma actuators - stationary and oscillating airfoils, AIAA 2004-0841 .

M. L. Post, T. C. Corke, Separation control on high angle of attack airfoil using plasma actuators, AIAA 2003-1024 .

A. Kozlov, F. O. Thomas, T. C. Corke, Plasma actuators for bluff body flow control, AIAA 2006-2845 .

S. Grundmann, C. Tropea, Experimental transition delay using glow-discharge plasma actuators, Experiments in Fluids 42 (2007) 653–657.

A. Kosinov, A. Maslov, S. Shevelkov, Experments on the stability of supersonic laminar boundary layer, Journal of Fluid Mechanics 219.

J. R. Roth, D. M. Sherman, Boundary layer flow control with a one atmosphere uniform glow discharge surface plasma, AIAA 98-0328 .

J. R. Roth, Aerodynamic flow acceleratoin using paraelectric and peristaltic electrohydrodynamic effects of a one atmosphere uniform glow discharge plasma, Physics of plasmas 10 (5) (2003) 2117 – 2126.

F. Cheng, X. Zhong, S. Gogineni, R. L. Kimmel, Effect of applied magnetic field on the instability of Mach 4.5 boundary layer over a flat plate, AIAA 2002-0351 .

M. Nishihara, N. Jiang, W. Rich, W. R. Lempert, I. Adamovich, Low-temperature supersonic boundary layer control using repetitively pulsed MHD forcing, AIAA 2005-5178 .

M. Nishihara, W. Rich, W. R. Lempert, I. V. Adamovich, Low-temperature M = 3 flow deceleration by Lorentz force, Physics of Fluids 18 (2006) 086101–1 – 11.

V. Bityurin, K. Savelkin, S. Leonov, D. Yarantsev, Effect of electrical discharge on separation processes and shocks position in supersonic airflow, AIAA-2002-0355 .

V. Bityurin, K. Savelkin, S. Leonov, D. Yarantsev, The features of electro-discharge plasma control of high-speed gas flows, AIAA 2002-2180 .

V. Bityurin, K. Savelkin, S. Leonov, D. Yarantsev, Effect of electrical discharge on separation process and shocks position in supersonic airflow, AIAA 2002-3055 .

S. B. Leonov, a. Y. D. A. Gromov, V. G, A. P. Kuriachy, Mechanisms of flow control by near-surface electrical discharge generation, AIAA 2005-780 .

S. Leonov, V. Bityurin, D. Yarantsev, The effect of plasma induced separation, AIAA 2003-3853 .

S. B. Leonov, Y. I. Isaenkov, A. Firsov, Mixing intensification in high-speed flow by unstable pulse discharge, AIAA 2009-4074 .

J. Menart, M. McFarland, K. Campbell, Use of a plasma arc to produce large surface pressure changes on a flat plate in a Mach 5 flow, AIAA 2007-631 .

H. Yan, D. Gaitonde, J. S. Shang, Numerical investigation of pulsed thermal perturbation in supersonic boundary layer, AIAA 2007-3887 .

P. Bletzinger, B. Ganguly, A. Garscadden, Strong Double-Layer formation by shock waves in non-equilibrium plasmas, Physical Review E 67 (2003) 047401–047401–4.

P. Bletzinger, B. Ganguly, V. W. D., A. Garscadden, Plasmas in hgh speed aerodynamics, Journal of Physics D: Applied Physics 38 (2005) R33–R57.

P. Q. Elias, B. Chanetz, S. Larigaldie, D. Packan, Study of the effect of glow discharges near M = 3 bow shock, AIAA Journal 45 (9) (2007) 2237–2245.

S. P. Kuo, I. M. Kaikhoran, D. Bivolaru, L. Orlick, Observation of shock wave elimination by a plasma in Mach-2.5 flow, Physics of Plasmas 7 (5) (2000) 1345–1348.

M. Samimy, I. Adamovich, B. Webb, J. Kastner, J. Hileman, S. Keshav, P. Palm., Development and characterization of plasma actuators for high-speed jet control, Experiments in Fluids (2004) 577–588.

S. Keshav, J.-H. Kim, J. Kastner, I. V. Adamovich, . Utkin, Y. G, M. Samimy, Development and use of localized arc filament plasma actuators for high speed flow control, Journal of Physics D: Applied Physics 40 (2007) 685 – 694.

M. Samimy, K. J. Kim, J-H., I. Adamovich, Y. Utkin, Active Control of a Mach 0.9 Jet for Noise Mitigation Using Plasma Actuators, AIAA Journal 45 (4) (2007) 890–900.

J.-H. Kim, Kastner-J., A. I., M. Samimy, Y. Utkin, Active control of high speed and high reynolds number jets using plasma actuators, Journal of Fluid Mechanics 578.

M. K. Fischer, J.-H. Kim, M. Samimy, Noise control of a high Reynolds number Mach 0.9 heated jet using plasma actuators, AIAA 2009 3188 .

E. Caraballo, N. Webb, J. Little, J.-H. Kim, M. Samimy, Supersonic inlet flow control using plasma actuators, AIAA 2009-724 .

J. Wang, Y. Li, B. Cheng, C. Su, H. Song, Y. Wu, Effects of plasma aerodynamic actuation on oblique shock wave in a cold supersonic flow, Journal of Physics D: Applied Physics 42 (2009) 165503–11.

J.-H. Kim, M. Nishihara, S. Keshav, I. Adamovich, M. Samimy, On the development of localized arc filament plasma actuators for high-speed flow control, AIAA 2009-4071 .

J. M. Kendall, Wind tunnel experiments relating to supersonic and hypersonic boundary layer transition, AIAA Journal 13 (1975) 290 – 299.

D. W. Ladoon, S. P. Schneider, Measurements of controlled wave packets at Mach 4 on a cone at angle of attack, AIAA 98-0436 .

A. A. Maslov, A. N. Shiplyuk, A. A. Sidorenko, D. Arnal, Leading edge receptivity of a hypersonic boundary layer on a flat plate, Journal of Fluid Mechanics 426 (2001) 73 – 94.

R. L. Kimmel, J. R. Hayes, J. A. Menart, J. S. Shang, Effect of magnetic fields on surface plasma discharges at Mach 5, AIAA 2004-2661 .

R. L. Kimmel, J. R. Hayes, J. A. Menart, J. S. Shang., Application of plasma discharge arrays to high-speed flow control, 2005-0946 .

J. Shin, N. V., L. L. Raja, N. T. Clemens, Generation of plasma induced flow actuation by dc glow-like discharge in a supersonic flow, AIAA-2006-169 .

J. Menart, S. Stanfield, J. S. Shang, R. Kimmel, J. Hayes, Study of plasma electrode arrangements of optimum lift in a Mach 5 flow, AIAA 2006-1172 .

S. Zaidi, B. Alderman, R. Miles, C. Kalra, Y. Murtp, Magnetically driven surface discharges for shock-wave induced boundary-layer separation control, AIAA 2007-222 .

S. O. Macherert, Physics of magnetically accelerated non-equilibrium surface discharges in high-speed flow, AIAA 2006-1005 .

C. S. Kalra, Z. S. H., M. N. Shneider, R. B. Miles, Shockwave induced turbulent boundary layer separation control with plasma actuators, AIAA 2009-1002 .

K. R. Grossman, B. Z. Cybyk, D. M. Van Wie, Sparkjet actuators for flow control, AIAA 2003-57 .

K. R. Grossman, B. Z. Cybyk, M. C. Rigling, D. M. Van Wie, Characterization of sparkjet actuators for flow control, AIAA 2004-89 .

B. Z. Cybyk, J. T. Wilkerson, K. R. Grossman, Performance characteristics of the sparkjet flow control actuator, AIAA 2004-2131 .

B. Z. Cybyk, K. R. Grossman, J. T. Wilkerson, J. Chen, J. Katz, Single pulse performance of the sparkjet flow control actuator, AIAA 2005-401 .

B. Z. Cybyk, D. H. Simon, H. B. Land, J. Chen, J. Katz, Experimental characterization of a supersonic flow control actuator, AIAA 2006-478 .

S. J. Haack, H. B. Land, B. Z. Cybyk, H. S. Ko, J. Katz, Characterization of a high speed flow control actuator using digital speckle tomography and PIV, AIAA 2008-3759 .

A. L. Kistler, Fluctuating wall pressure under a separated supersonic flow, Journal of Acoustic Society of America 36 (3) (1964) 543 – 550.

A. J. Smits, J. P. Dussague, Turbulent shear layers in supersonic flow, AIP Press, Woodbury, NY, 1996.

J. Delery, J. Marvin, Shock-wave boundary layer interactions, AGARDograph 280.

A. Zheltovodov, Shock wave / turbulent boundary layer interactions: Fundamental studies and applications, AIAA 96-1977 .

Y. Andreopoulos, J. H. Agui, G. Briassulis, Shock wave-turbulence interactions, Annual Review of Fluid Mechanics 32 (2000) 309–345.

D. D. Knight, G. Degrez, Shock wave boundary layer interactions in high Mach number flows, A critical survey of current numerical prediction capabilities, Advisory Rept. 319, AGARD 2 (1998) 1.1–1.35.

J. P. Dussauge, Compressible turbulence and energetic scales: What is known from experiments in supersonic flow ?, Flow, Turbulence and Combustion 66 (2001) 373–391.

J. Andreopoulos, K. C. Muck, Some new aspects of the shock-wave boundary layer interaction, Journal of Fluid Mechanics 32 (1987) 309–345.

M. E. Erengil, D. S. Dolling, Correlation of separation shock motion with pressure fluctuations in the incoming boundary layer, AIAA Journal 29 (11) (1991) 1868–1877.

M. E. Erengil, D. S. Dolling, Physical causes of separation shock unsteadiness in shock wave turbulent boundary layer interactions, AIAA 1993-3134 .

D. Hunt, D. Nixon, Very large eddy simulation of an unsteady shock-wave turbulent boundary layer interaction, AIAA 95-2212 .

P. Wu, R. B. Miles, Megahertz visualization of compression-corner shock structures, AIAA Journal 39 (2001) 1542–1546.

S. J. Beresh, M. Comninos, N. T. Clemens, D. S. Dolling, The effects of the incoming turbulent boundary layer structure on a shock-induced separated flow, AIAA 97- .

L. Brusniak, D. S. Dolling, Physics of unsteady blunt-fin induced shock wave/-turbulent boundary layer interactions, Journal of Fluid Mechanics 273 (1994) 375–409.

W. B. McClure, An experimental study of the driving mechanism and control of the unsteady shock induced turbulent separation in a Mach 5 compression corner flow, Ph.D. thesis, The University of Texas at Austin, 1992.

O. H. Unalmis, D. S. Dolling, Decay of wall pressure field structure of a Mach 5 adiabatic turbulent boundary layer, AIAA 1994-2363 .

S. J. Beresh, N. T. Clemens, D. S. Dolling, Relationship between upstream boundary layer velocity fluctuations and separtion shock unsteadiness, AIAA Journal 40 (12) (2002) 2412–2422.

B. Ganapathisubramani, N. T. Clemens, D. Dolling, Large scale motions in a supersonic turbulent boundary layer, Journal of Fluid Mechanics 556 (2006) 271–282.

B. Ganapathisubramani, N. Clemens, D. Dolling, Effects of upstream boundary layer on the unsteadiness of shock-induced separation, Journal of Fluid Mechanics 585 (2007) 369–394.

B. Ganapathisubramani, N. Clemens, D. Dolling, Low-frequency dynamics of shock-induced separation in a compression ramp interaction, Journal of Fluid Mechanics 636 (2009) 397–425.

R. A. Humble, G. E. Elsinga, F. Scarano, B. W. van Oudheusden, Investigation of the instantaneous 3D flow organization of a shock wave/ turbulent boundary layer interaction using tomographic PIV, AIAA 2007-4112 .

P. Dupont, C. Haddad, J. F. Debieve, Space and time organization in a shock-induced separated boundary layer, Journal of Fluid Mechanics 559 (2006) 255–277.

P. Dupont, C. Haddad, J. P. Ardissone, J. F. Debieve, Space and time organization of a shock wave/turbulent boundary layer interaction, Aerospace Science and Technology 9 (2005) 561–572.

J. Dussauge, P. Dupont, J. Debieve, Unsteadiness in shock wave boundary layer

interactions with separation, Aerospace Science and Technology 10 (2006) 85–91.

P. Dupont, S. Piponniau, A. Sidorenko, J. F. Debieve, Investigation by Particle Image Velocimetry Measurements of Oblique Shock Reflection with Separation, AIAA Journal 46 (6).

S. Piponniau, J. P. Dussague, J. F. Debieve, P. Dupont, A simple model for low-frequency unsteadiness in shock induced separation, Journal of Fluid Mechanics 629.

M. J. Ringuette, M. Wu, M. P. Martin, Coherent structures in direct numerical simulation of turbulent boundary layers at Mach 3, Journal of Fluid Mechanics 594 (2008) 59–69.

M. Wu, M. P. Martin, Analysis of shock motion in shockwave and turbulent boundary layer interaction using direct numerical simulation data, Journal of Fluid Mechanics 594 (2008) 71–83.

S. Pirozolli, F. Grasso, Direct numerical simulation of impinging shock wave/ turbulent boundary layer interaction at M = 2.25, Physics of Fluids 18 (2006) 065113–1 – 17.

E. Touber, N. D. Sandham, Oblique shock impinging on a turbulent boundary layer: low-frequency mechanisms, AIAA 2008-4170 .

H. Holden, H. Babinsky, Separated shock-boundary layer interaction control using streamwise slots, Journal of Aircraft 42 (1) (2005) 166–171.

H. Babinsky, M. Patzold, H. Ogawa, T. Lutz, Shock-wave/ boundary-layer interaction control using three-dimensional bumps for transonic wings, AIAA Journal 46 (6).

D. C. McCormick, Shock-boundary layer interaction control with low-profile vortex generators and passive cavity, AIAA 1992-0064 .

J. W. Barter, D. S. Dolling, Reduction of fluctuating pressure loads in shock/boundary-layer interactions using vortex generators: Part 1, AIAA Journal 33 (10) (1995a) 1842–1849.

J. W. Barter, D. S. Dolling, Reduction of fluctuating pressure loads in shock/boundary-layer interactions using vortex generators: Part 2, AIAA Journal 34 (1) (1995b) 195–197.

a. W. J. Bueno, P. C., J. Searcy, B. Ganapathisubramani, N. T. Clemens, D. S. Dolling, Experiments in unsteady forcing of Mach 2 shock wave/boundary layer interactions, AIAA-2006-878 .

H. A. Holden, H. Babinsky, Vortex generators near shock/boundary layer interactions, AIAA 2004-1242 .

H. Holden, H. Babinsky, Effect of microvortex generators on separated normal shock/boundary-layer interactions, Journal of Aircraft 44 (1).

C. W. Pitt Ford, H. Babinsky, Micro-ramp control for oblique shock wave/boundary layer interactions, AIAA 2007-4115 .

Y. Lee, E. S. Hafenrichter, J. C. Dutton, E. Loth, Skin friction measurements for recirculating normal-shock/boundary layer interaction control, AIAA Journal 42 (4) (2004) 806–814.

D. Gefroh, E. Loth, C. Dutton, S. McIlwain, Control of an oblique shock/boundary-layer interaction with aeroelastic mesoflaps, AIAA Journal 40 (2002) 2456–2466.

E. Loth, R. Jaiman, C. Dutton, S. White, F. Roos, J. Mace, D. Davis, Mesoflap and bleed flow control for a Mach 2 inlet, AIAA 2004-0855 .

K. R. Sreenivasan, E. Loth, J. C. Dutton, Aerodynamics of recirculating flow control devices for normal shock/boundary layer interactions, AIAA 2004-426 .

D. J. Peake, The use of air injection to prevent separation of the turbulent boundary layer in supersonic flow, Aeronautical Research Council Current Papers (890).

P. R. Viswanath, L. Sankaran, P. M. Sagdeo, R. Narasimha, A. Prabhu, Injection slot location for boundary-layer control in shock induced separation, Journal of Aircraft 20 (8) (1983) 726–732.

M. S. Selig, A. J. Smits, Effect of periodic blowing on attached and separated supersonic turbulent boundary layers, AiAA Journal 29 (10) (1991) 1651–1658.

R. A. Wallis, A preliminary note on a modified type of air jet for boundary layer control, Aeronautical Research Council Current Papers (513).

J. P. Johnston, M. Nishi, Vortex generator jets - means for flow separation control, AIAA Journal 28 (6) (1990) 989–994.

D. A. Compton, J. P. Johnston, Streamwise vortex production by pitched and skewed jets in a turbulent boundary layer, AIAA Journal 30 (3) (1992) 640–647.

X. Zhang, M. W. Collins, Measurements of a longitudinal vortex generated by a rectangular jet in a turbulent boundary layer, Physics of Fluids 9 (6) (1997) 1665–1673.

E. R. Lachney, Two-dimensional temperature and pressure imaging of a supersonic flat plate wake, Master's thesis, The University of Texas at Austin, 1995.

T. G. Sanders, Sidewall and pitot pressure measurements of a Mach 3 turbulent wake, Master's thesis, The University of Texas at Austin, 1995.

M. F. Smith, Observations of supersonic flat plate wakes, Master's thesis, The University of Texas at Austin, 1995.

W. Merzkirch, Flow Visualization (Second Edition), Academic Press Inc., 1987.

M. Samimy, S. K. Lele, Motion of particles with inertia in a compressible free shear layer, Physics of fluids A 3 (1991) 1915 – 1923.

M. Raffel, C. Willert, J. Kompenhans, Particle Image Velocimetry - A practical guide, Springer, 2001.

R. A. Freeman, Variable-energy blast waves, Brit. J. Appl. Phys. (J. Phys. D.) 1 (2) (1968) 1697 – 1710.

M. N. Director, E. K. Dabora, Predictions of variable-energy blast waves, AIAA Journal 15 (9) (1977) 1315 – 1321.

F. Milinazzo, Y. Oved, R. M. Clements, P. R. Smy, Blast wave computations using the flux-corrected transport algorithm, J. Phys. D: Appl. Phys. 12 (1979) 1039 – 1049.

Y. Oved, F. Milinazzo, R. M. Clements, P. R. Smy, Blast waves produced by a time dependent energy source, AIAA Journal 17 (6) (1979) 601 – 605.

P. Kothnur, L. Raja, Two-dimensional simulation of a direct-current microhollow cathode discharge, Journal of Applied Physics 97 (4).

J. Shin, V. Narayanaswamy, L. L. Raja, N. T. Clemens, Characterization of a Direct-Current Glow Discharge Plasma Actuator in Low-pressure Supersonic Flow, AIAA Journal 45 (2007) 1596 – 1605.

Y. Utkin, S. Keshav, J. Kim, J. Kastner., I. Adamovich, M. Samimy, Characterization of Localized Arc Filament Plasma Actuators Used for High-speed Flow Control, AIAA-2007-787 .

Y. P. Raizer, Gas Discharge Physics, Springer, New York, 1991.

W. G. Vincenti, C. H. Kruger, Introduction to Physical Gas Dynamics, Krieger Publishing Company, 2002.

A. G. Engelhardt, A. V. Phelps, C. G. Risk, Determination of momentum transfer and inelastic collision cross sections for electrons in nitrogen using transport coefficients, Physical Review Letters 135 (6A) (1964) A1566–1574.

L. S. Frost, A. V. Phelps, Rotational excitation and momentum transfer cross section for electrons in H2 and N2 from transport coeffiecients, Physical Review 127 (5) (1962) 1621 – 1633.

L. C. Pitchford, S. V. Oneil, J. R. Rumble Jr, Extended Boltzmann analysis of elecgtron swarm experiments, Physical Review A 23 (1) (1981) 294 – 304.

L. C. Pitchford, A. V. Phelps, Comparative calculations of electron-swam properties in N2 at moderate E/N values, Physical Review A 25 (1) (1982) 540 – 554.

F. E. C. Culick, P. I. Shen, W. S. Griffin, Acoustic waves and heating due to molecular energy transfer in an electric discharge CO2 laser, IEEE Journal of Quantum electronics QE-12 (10) (1976) 566 – 574.

P. Smy, R. Clements, J. Dale, S. D., T. D.R., Efficiency and erosion characteristics of plasma jet igniters, J. Phys. D: Appl. Phys. 16 (1983) 783–791.

P. R. Smy, R. M. Clements, D. Simeoni, D. R. Topham, Plasma expulsion from the plasma jet igniter, J. Phys. D: Appl. Phys. 15 (1982) 2227–2239.

J. D. Anderson, Modern compressible flow with historic perspective, McGraw-Hill New York, 2002.

B. Z. Cybyk, K. R. Grossman, J. T. Wilerson, Single pulse performance of the sparkjet flow control actuator, AIAA 2003-57 .

S. Murugappan, E. Gutmark, C. Carter, Control of penetration and mixing of excited supersonic jet in supersonic crossflow, Physics of Fluids 17 (2005) 106101–1–13.

D. Knight, V. Kuchinskiy, A. Kuranov, E. Sheikin, Survey of aerodynamic flow control at high speed by energy deposition, AIAA 2003-0525 .

R. Adelgren, H. Yan, G. Elliott, D. Knight, Localized Flow Control by Laser Energy Deposition Applied to Edney IV and Intersecting Shocks, AIAA 2003-0031 .

J. C. Gonsalez, D. S. Dolling, Correlation of interaction sweepback effects on the dynamics of shock-induced turbulent separation, AIAA-93-0776 .

J. Shin, N. T. Clemens, L. L. Raja, Schlieren imaging of flow actuation produced by direct current surface glow discharge in supersonic flows, IEEE Transactions in Plasma Science 36 (4).

L. Yu, L. Pierrot, C. O. Laux, C. H. Kruger, Effects of vibrational non-equilibrium on the chemistry of two-temperature Nitrogen plasmas, Plasma Chemistry and Plasma Processing 21 (2001) 483 – 503.

T. Deconinck, S. Mahadevan, L. L. Raja, Simulation of Direct-current surface plasma phenomena in high-speed flow actuation, IEEE Transactions on Plasma Science 35 (5) (2007) 1301 – 1311.

A. Sinha, K. Kim, J.-H. Kim, A. Serrani, M. Samimy, Towards feedback control of high speed and high Reynolds number jets, AIAA 2008-3862 .

J. Shin, A study of direct-current surface discharge plasma for a Mach 3 supersonic flow control, Ph.D. thesis, The Unversity of Texas at Austin, 2007.

Vita

Venkat Narayanaswamy was born on the 6th of May, 1983 as the first child of R. Lakshmi and T. V. Narayanaswamy. He attended and graduated from the Indian institute of Technology, Madras in 2004 with Bachelor of Technology in Aerospace Engineering. He joined graduate school at the University of Texas at Austin in August of 2004. He pursued his graduate studies with a view to obtain his Ph.D.

Permanent address: No. 15/2 Vadivelu 3rd Cross Street, Perambur,
Chennai - 600011, India

This dissertation was typeset with LaTeX[†] by the author.

[†]LaTeX is a document preparation system developed by Leslie Lamport as a special version of Donald Knuth's TeX Program.